NOTE TO USERS

Page(s) missing in number only; text follows. The manuscript was microfilmed as received.

165-166

This reproduction is the best copy available.

Nonlinear Optical Spectroscopy and Imaging of Photonic Materials and Nanostructures

by

Michael Etienne

A dissertation submitted to the Graduate Faculty in Electrical Engineering in partial fulfillment of the requirements for the degree of Doctor of Philosophy

The City University of New York

2007

This manuscript has been read and accepted for the Graduate Faculty in Electrical Engineering in satisfaction of the dissertation requirement for the degree of Doctor of Philosophy.

	Roger Dorsinville, Ph.D.
Date	Chair of Examining Committee
	Mumtaz Kassir, Ph.D.
Date	Executive Officer

Ardie Walser, Ph.D. Associate Dean, The City College of New York

Fred Moshary, Ph.D. The City College of the City University of New York

Mark Arend, Ph.D. Research Associate, The City College of New York

Dr. Haim Grebel, Ph.D. Department of Electrical Engineering, New Jersey Institute of Technology.

Supervisory Committee

THE CITY UNIVERSITY OF NEW YORK

Abstract

Nonlinear Optical Spectroscopy and Imaging of Photonic Materials and Nanostructures

By

Michael Etienne

Advisor: Professor Roger Dorsinville

We investigated the nonlinear optical susceptibilities, the nonlinear absorption coefficients and the nonlinear transmission properties of various photonic glasses and crystals. The enhancement of the nonlinear absorption coefficient due to Two-Photon Absorption (TPA) in structural and optical defects in fused silica materials was explored. The correlation between the presence of defects and the increase in TPA was then used to propose a novel *in situ 2-D* mapping technique for defect detection when growing Potassium Dihydrogen Phosphate (KDP) crystals and their analogs. Open and close aperture Z-scans were also performed on various CdS quantum dots embedded in different generations, G4, G5 and G6, dendrimer films using picosecond and femtosecond pulses between 350 nm and 1 μm. The measured values of the third order nonlinear coefficient were among the highest off-resonance nonlinearities reported for organic and/or hybrid composites materials. We have shown that the nonlinear response in these materials is also a function of the dynamics of the excited states involved and that measurements of the nonlinear optical coefficient with pulses of different duration are directly correlated to the dynamics of the excited states. Finally, the nonlinear optical properties of hybrid systems based on single-wall carbon nanotubes were investigated at different laser pulse durations. These materials show interesting nonlinear transmission properties which makes them perfect candidates for optical limiting applications.

Acknowledgments

During the course of my doctoral studies, I lost both my grandmother and my mother, the two people dearest to me. Three weeks before my thesis defense, my mother, Lucille Hermione Jean-Francois, had a major stroke and died a week later. I am forever grateful to her, for her guidance, her teachings, her endless love for me. I am most grateful to God, for blessing me with so many things and good people in my life, among them a wonderful mother. Through Him I love her, and through her I love Him.

I am grateful to my advisor, Dr. Roger Dorsinville, for all his help and guidance throughout the years. I have dived into the vast sea of his knowledge only to realize after so many years that I was still very close to the surface.

My appreciation goes to the members of the committee, in particular, Dr. Ardie Walser, my co-advisor, for his constant effort to keep me focus on the goal, in particular for his correlation between entrepreneurship and doctoral studies. I think I finally got it.

I am thankful to Prof. Fred Moshary and Dr. Haim Grebel for their contribution and suggestions through discussions. Many thanks to Prof. Valeria Balogh-Nair for her generosity with many interesting quantum dots samples.

A special thank goes to my very supportive family, principally Harry Prophete, MD, for his unconditional support. My sister Nadia Etienne, my dear cousins Viathie and Gabrielle Julsaint for their help and trust.

A very special thank you goes to Mr. Pierre Belizaire, a second godfather to me who gave me the opportunity to make a dream come true.

In memoriam Mrs. Sosthenes Jean-Francois and Mrs. Lucille Hermione Jean-Francois

Table of Contents

List of Figures

List of Tables

Chapter I

Introduction and brief review of Nonlinear Optics and photonic materials

1.1. Introduction

This thesis summarizes the work done in assessing the nonlinear optical properties of a variety of photonic materials including some newly developed hybrid structures of semiconductor quantum dots embedded in polymeric matrices. The different spectroscopic methods used in this thesis are all transmission-based measurements, namely the open and close aperture Zscan technique and the nonlinear transmission spectroscopy. Nonlinear transmission refers to either an increase or a decrease in the transmission of a system with increasing intensity, fluence, incident angle or position along the z-axis. The Zscan technique, described later in this thesis, is based on the principle of spatial beam distortion and allows complete characterization of the real and imaginary parts of the third-order nonlinear susceptibility. Historically, there has been a growing interest in addressing the long-term degradation of various optical elements used in large aperture ultra-high intensity laser systems. Although the bulk of the available literature has been focused on laser damage threshold and identification of the defects present in the bulk materials, in this thesis however, we perform studies and analysis of the optical absorption in such optical components and determine whether or not multiphoton absorption processes occur in a damaged optical window and can be used as an imaging tool to identify their origin.

The first part of this thesis concerns with the transmission performance of fused silica-based optical elements. Owing to its optical properties in the UV region, fused silica is the material of choice for transmitting intense laser light at 355nm. However, obscuration of the material after prolonged hours operating under such high intensity UV laser irradiation, reduces its performance[1], therefore prompting for improved quality of the material. Obscuration losses, in general, are a result of damage initiation at an absorbing site, followed by subsequent growth of the damage area through further energy absorption. The mechanism of energy absorption at the damage site has been the subject of intense investigation[2-5] but is still partially unclear. By studying the transmission properties at pristine and damage sites of a fused silica substrate, we were able to correlate the presence of optical defects with two-photon absorption processes in the material.

Potassium dihydrogen phosphate (KH_2PO_4 or *KDP*) is another critical element found in ultra high intensity laser systems. Its transparency in the visible region coupled to a high second order nonlinear susceptibility makes it an excellent choice for light frequency converter and Pockels cell. However, the efficiency of energy conversion in KDP although among the highest available, can still be considered rather low[6]. This is a result of the fluence-dependent nature of frequency conversion in the material, which is limited by the presence of absorbing traps or defects in the crystal lattice. In large aperture optical elements, defects and impurities are a key limiting factor in material performance leading to optical losses and material failure[7]. It is therefore a very important task to locate and mitigate such defects, allowing higher incident power onto the crystal,

translating into higher available harmonic power if not better energy conversion efficiency. We will investigate the effects of impurities on the efficiency of KDPs, correlate those impurities with an increase in the two-photon absorption (*TPA*) coefficient and devise a new TPA-based imaging technique allowing to pin-point absorbing centers in the bulk material.

Another key issue overshadowing nonlinear materials is the lack of direct device implementation due to the rather low yield of nonlinear optical phenomena. An optical limiter, for example, requires either a large TPA coefficient or a combination of a large excited state cross section and a small ground state absorption cross section[8], an optical switch can be either based on reverse saturable absorption (*RSA*) or have a large nonlinear refraction coefficient and a small TPA coefficient[9]. Most available materials do not respond to such characteristics, and their development in many cases is not a straightforward process. The second part of our work is concerned with the optical characterization of highly performing nonlinear materials suitable for optical switching and optical limiting devices. Due to the antagonistic nature of waveguide-based optical switches and TPA-based optical limiters, two distinct nanostructure materials were developed. The first of these novel structures combines the excitonic properties of a semiconductor quantum dot with those of a dendritic nanoreactor to induce enhancement of the overall nonlinear response via dipole-dipole interaction[10]. This results in an unusually large nonlinear refraction coefficient along with a low TPA coefficient, essential qualities of a good optical switch. Using the single beam Zscan technique[11], the real part of the third-order nonlinear susceptibility was determined for a variety of such

hybrid systems at various wavelengths, quantum dots size and optical pulse durations. We conclude our investigation with the report of optical limiting behavior in single wall carbon nanotubes in a variety of configurations including SWCNT within various matrices of conductive polymer.

1.2. Nonlinear Optics and Photonics

The field of Photonics encompasses the different areas of optics involved in the control of photons. Photonics thus refers to the generation, transmission, modulation, amplification, frequency conversion and detection of coherent light. Because of the great promises of its potential applications, it has long been labeled the technology of the 21st century. The driving force behind photonics is the field of Nonlinear Optics. Nonlinear optics is to photonics what transistor is to electronics. The great interest generated over nonlinear optics in the past decades is not merely due to the quest for understanding the array of new phenomena occurring when an intense laser field interacts with a material, but mostly to the tremendous potential applications of NLO phenomena to the improvement of our quality of life. Many applications in Medicine, Telecommunications and Defense, just to name a few areas, are already benefiting from the nonlinear responses of materials. However, contrasting with their vast domain of applications, implementations based on nonlinear-optical effects utilize only two important manifestations[12]: frequency conversion related to the second-order nonlinear susceptibility and refractive index modulation associated with the third-order polarizability.

The second-order nonlinear susceptibility ($\chi^{(2)}$) is responsible for applications such as wavelength conversion and parametric processes, image analysis, high-density data storage and electrooptic spatial light modulators. Materials for wavelength conversion or lambda switching are of great interest in communication systems since they allow wavelength discrimination at the routing or multiplexing level (*maintaining the signal in the optical domain*), providing a drastic reduction in the processing time of optical information. They also are in great demand in lithographic systems where they allow access to wavelengths otherwise inaccessible through conventional eximer lasers. It is generally expected that devices based on the third-order nonlinear susceptibility provide faster switching rates than those based on the second-order effect. This is due to the fact that in the case of the second-order effect, the refractive index modulation is produced by an applied electric field, while for the third-order effects, the refractive index modulation is induced by a change of intensity of a controlling optical field. Therefore, light is controlled by light, resulting in much faster switching rates[13]. The third-order nonlinear susceptibility ($\chi^{(3)}$) leads to devices such as optical limiters, all-optical modulators and switches, wave mixers, saturable absorbers, and directional couplers[14]. All-optical switching is by far the most important representative of this group. It is perceived as an essential element for the future development of optical information processing and applications in broadband communications, eliminating the bottleneck due to optical to electrical signal conversion. Since optical switching in the nonresonant case can be in sub-picoseconds corresponding to bit rates of various terabits per second, all-optical processing will provide a substantial increase in speed. The advent of seamless and efficient wavelength conversion techniques along with highly performing optical

switches will provide a sure pathway to implementing a true all-optical communications system. Furthermore, concepts of optically adaptive neural network for signal processing have been proposed based on the three-dimensional holographic connectivity of channeled waveguides and the photorefractive effect[15]. This would constitute the first step towards a truly intelligent all-optical network allowing for fast dynamic connectivity and lower processing time at the nodes.

Compared to second-order-related devices, applications exploiting third-order nonlinearities are still in the stage of infancy. Since the origins of the nonlinear processes are now well understood, progress in nonlinear applications depends widely on the ability to develop new materials technology where the nonlinear optical responses can be optimized and the response time shortened.

1.3. Nonlinear Optics

A light wave consists of electric and magnetic fields varying sinusoidally at high frequencies. When light propagates through matter it induces motion of the charged particles that constitute the material. In a dielectric medium the charges are bound together and will start to oscillate in the applied electric field; they form oscillating electric dipoles. The contribution from the magnetic field part of the light and from electric quadrupoles is much weaker and is usually neglected. This is called the electric-dipole approximation. The oscillating dipoles add up to a macroscopic polarization P which is used to describe the response of the material. For low light intensities, i.e. small amplitudes of the electric field E, the charges can follow the field almost exactly and the relationship between E and P is essentially linear. For larger amplitudes the motion of the particles will be distorted and nonlinear terms will become important. The origin of nonlinear optics can be uncovered by recalling Maxwell's equations[16], which are a set of laws governing light-matter interaction.

Starting with

$$\nabla \times E = -\frac{1}{c}\frac{\partial B}{\partial t} \tag{1.1}$$

$$\nabla \times B = \frac{1}{c}\frac{\partial E}{\partial t} + \frac{4\pi}{c}J \tag{1.2}$$

$$\nabla \bullet E = 4\pi\rho \tag{1.3}$$

and $$\nabla \bullet B = 0 \qquad (1.4)$$

where *E(r, t)* and *B(r, t)* are the electric and magnetic fields respectively. The charge density ρ and the current density j are related through the law of charge conservation

$$\nabla \bullet j + \frac{\partial \rho}{\partial t} = 0 \qquad (1.5)$$

with $\rho = \rho_0 - \nabla \bullet P$ and $j = j_0 + \frac{\partial P}{\partial t}$ under electric dipole moment approximation. For a free medium, with $\rho_0 = 0$ and $j_0 = 0$, the third Maxwell equation becomes

$$\nabla \bullet E + 4\pi \nabla \bullet P = 0 \qquad (1.6)$$

while the combination of the first two Maxwell equations leads to

$$\nabla^2 E - \nabla(\nabla \bullet E) - \frac{\partial^2 E}{c^2 \partial t^2} - \frac{4\pi}{c^2}\frac{\partial^2 P}{\partial t^2} = 0 \qquad (1.7)$$

where $\frac{\partial^2 P}{\partial t^2}$ is the induced polarization term. In case of nonlinear manifestations, the polarization vector contains both a linear and a nonlinear contribution of the material. Provided that these new nonlinear terms are still small compared to the linear one, we can expand the polarization vector *P* in a power series in *E*:

$$P(t) = P^{(1)}(t) + P^{(2)}(t) + P^{(3)}(t) + P^{(4)}(t) + ...$$

$$\boldsymbol{P} = \varepsilon_0 (\chi^{(1)} \boldsymbol{E} + \chi^{(2)} \boldsymbol{E}^2 + \chi^{(3)} \boldsymbol{E}^3 + \chi^{(4)} \boldsymbol{E}^4 \ ...) \qquad (1.8)$$

Here $\chi^{(1)}$ is the linear susceptibility of the medium, often called the polarizibility and is related to the linear refractive index n by $n^2 = 1 + \chi^{(1)}$. The quantities $\chi^{(2)}$, $\chi^{(3)}$, ... are the nonlinear susceptibilities and they describe the nonlinear-optical properties of the medium.

It is worth mentioning here that even-order nonlinear suceptibilities can not exist in a material with inversion symmetry (centrosymmetric material). For example, in many isotropic media such as glasses, liquids and gasses, there can be no even powers of the field in the expansion of the polarization for symmetry reasons. The lowest-order nonlinearity is then the cubic term in Eq. (1.8).

The importance of the induced polarization can be understood from the fact that any oscillating dipole also emits radiation, at the frequency of oscillation, and thus modifies the optical field that induced the polarization. The following treatment can be found in any Nonlinear Optics reference book[17]. To demonstrate some of the many nonlinear phenomena that can occur, consider the following incoming field

$$E(t) = E_1 e^{-i\omega_1 t} + E_2 e^{-i\omega_2 t} + c.c. \qquad (1.9)$$

the second-order nonlinear response is given by

$$P^{(2)}(t) = \chi^{(2)}[E_1^2 e^{-2i\omega_1 t} + E_2^2 e^{-2i\omega_2 t} + 2E_1 E_2 e^{-i(\omega_1+\omega_2)t} + 2E_1 E_2^* e^{-i(\omega_1-\omega_2)t} + c.c.] + 2\chi^{(2)}[E_1 E_1^* + E_2 E_2^*] \quad (1.10)$$

Within this expression, it's easy to see various manifestations. The terms in $2\omega_i$ account for second harmonic generation; the terms in $\omega_1 \pm \omega_2$ are related to the sum and difference frequency generation; and the terms independent of ω (static E fields) are responsible for optical rectification. Connected to this latter effect, is the electrooptic effect where a static field modifies the optical properties of the medium. Most generally, the quadratic term involves the mixing of three different fields (it multiplies two fields to generate a third). This term is thus used for Optical Parametric Conversion by three-wave mixing. It is worth noting that only one of these competing processes can be amplified at one time. The selection will be determined by factors such as the polarization of the incoming beams and the phase-matching condition.

The same argument can be applied to study the third-order nonlinear responses of materials. For simplification purpose, let's consider a monochromatic field given by

$$E(t) = E \cos \omega t \quad (1.11)$$

Since, $\cos^3 \omega t = (1/4)\cos 3\omega t + (3/4)\cos \omega t$, the third order nonlinear polarization $P^{(3)}(t)$ can be written as

$$P^{(3)}(t) = (1/4)\chi^{(3)}E^{(3)} \cos 3\omega t + (3/4)\chi^{(3)}E^{(3)} \cos \omega t \quad (1.12)$$

The first term is the response of the applied electric field at frequency 3ω. This term corresponds to third harmonic generation process, which is illustrated in Fig. 1.2. Third harmonic generation is a process in which three photons of frequency ω are destroyed and one photon of frequency 3ω is simultaneously created.

The second term is very important for applications based on intensity-dependent refractive index, since it gives the relationship between the third-order susceptibility and the index of refraction at frequency ω. Using only the responses at the fundamental wavelength along with the permittivity of the material, one can obtain the expression,

$$n \approx n_0 + n_2 I \qquad (1.13)$$

which shows that the refractive index is directly proportional to the intensity of the incoming field. For a beam with a Gaussian profile, the index of refraction will follow a radial Gaussian distribution, which for the positive n_2 case means higher index of refraction at the center of the beam and lower index of refraction at the edge of the beam. This positive lens-like refractive index will give rise to what is known as the self-focusing phenomenon. Self-focusing at times is a very undesirable effect, since it readily leads to catastrophic dielectric optical breakdown in fibers and other devices due to the critical increase in intensity as light travels through the confined medium. For this reason, extensive research has been performed on materials with negative $\chi^{(3)}$ as self-defocusing associated with the negative n_2 can successfully solve the optical medium damage problem associated with self-focusing.

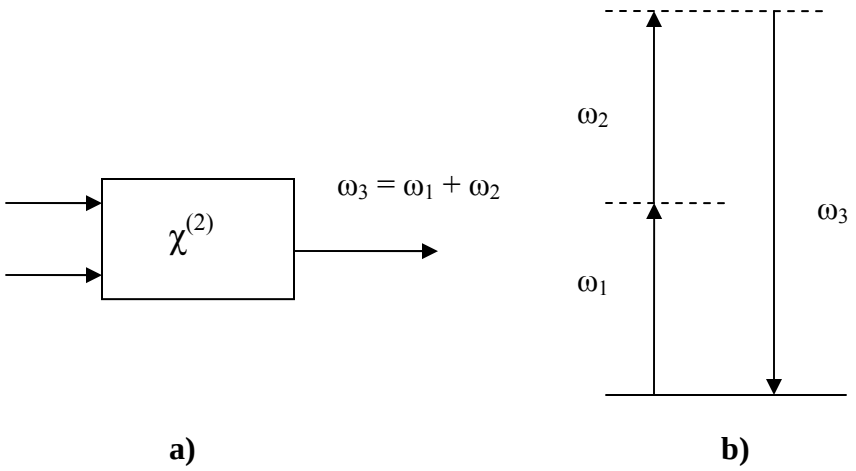

Fig 1.1 Sum frequency and second-harmonic generation a) Geometry of interaction b) Energy-level diagram

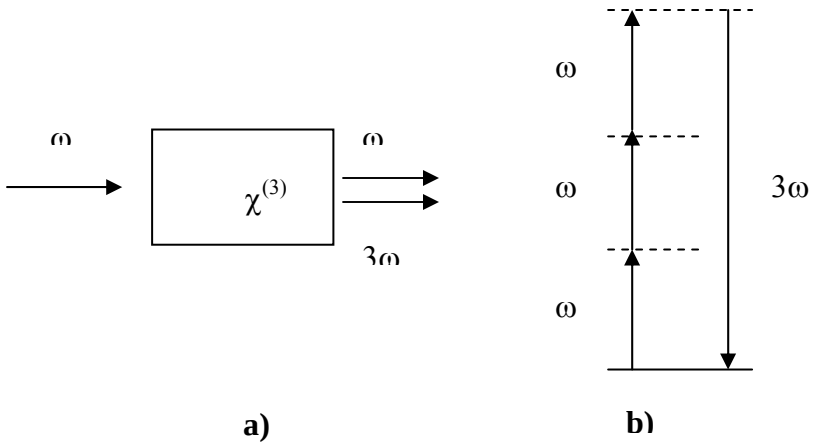

Fig 1.2 Third-harmonic generation a) Geometry of interaction b) Energy-level diagram

Another intensity-dependent phenomenon is two-photon absorption (*TPA*). TPA is a non-parametric process where an atom makes a transition from the ground state to a real excited state by simultaneously absorbing two laser photons. The intermediate transition typically involves a virtual state. While linear absorption probes the single-photon absorption properties of a material, two-photon absorption spectroscopy provides complementary information by probing the excited states of the system. It reveal important information regarding the nonlinear absorption coefficient of a given sample. The two-photon absorption scenario is illustrated in figure 1.3. This geometry shows the scenario where a transition is approximately resonant a 2ω. In this case, two photons from the same optical field oscillating at frequency ω are simultaneously absorbed in order to bring the excited atom to the higher lying state.

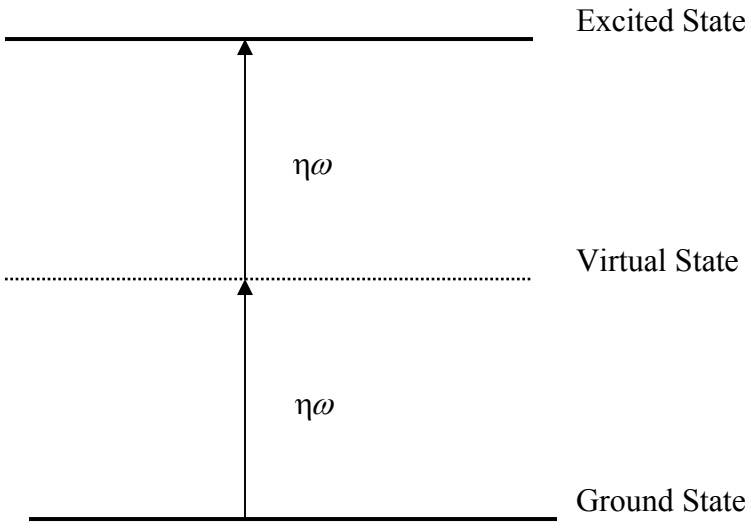

Fig 1.3 Schematic diagram of two-photon absorption. (TPA)

Other phenomena related to the intensity-dependent refractive index are Kerr effect and self-phase modulation. Self-phase modulation (SPM) refers to the self-induced phase shift experienced by an optical field during its propagation in a nonlinear medium. In fiber optics communications, for example, SPM is responsible for spectral broadening of ultrashort pulses and the existence of optical solitons in the anomalous-dispersion (negative dispersion) regime of fibers[18].

As has been shown so far, the cubic term is of major importance to this thesis since it is responsible for intensity dependent refractive index effects. TPA plays an crucial role in the first part of this thesis, since it allows investigation of optical limiting behavior in many inorganic materials.

1.4. Optical limiters

Optical limiting (OL) is a nonlinear optical process by which a material displays high transmission for low input intensity and low constant transmission at high input intensity or fluence. Optical limiters are one of the most important types of devices used to control the amplitude of high intensity optical pulses[19-21]. Since their direct use consists in providing protection for sensitive optical components from high-power laser radiation and optical transients, an optical limiter is required to have a wide dynamic range. The dynamic range is defined as the ratio between the input intensity to the threshold value for limiting action. Several characteristic outputs of optical limiters are illustrated in Fig. 1.4[22]. For low incident intensity or fluence, the devices show a linear transmittance. The slope of the linear region of an optical limiter can be very close to 45° corresponding to 100% transmission. This is mostly the case in two-photon absorbers. When the input fluence reaches a critical threshold limit, the transmittance of an optical limiter becomes nearly constant. Obtaining the response of Fig. 1.4 turns out to be possible by using a wide variety of materials[23]; however based on the nonlinear effects used, there are just two types of optical limiters: the energy-spreading type and the energy-absorbing type[24]. In the energy-spreading type of optical limiter, an aperture is placed in the far field in front of a recording detector. Various nonlinear optical mechanisms such as self-focusing, self-defocusing, induced scattering, induced-refraction and induced-aberration are then used in the nonlinear media to create the optical limiting effect. Nonlinear optical phenomena such as two-photon absorption (TPA), excited-state absorption (ESA) and reverse saturable absorption (RSA) make the bulk of energy-absorbing optical limiters.

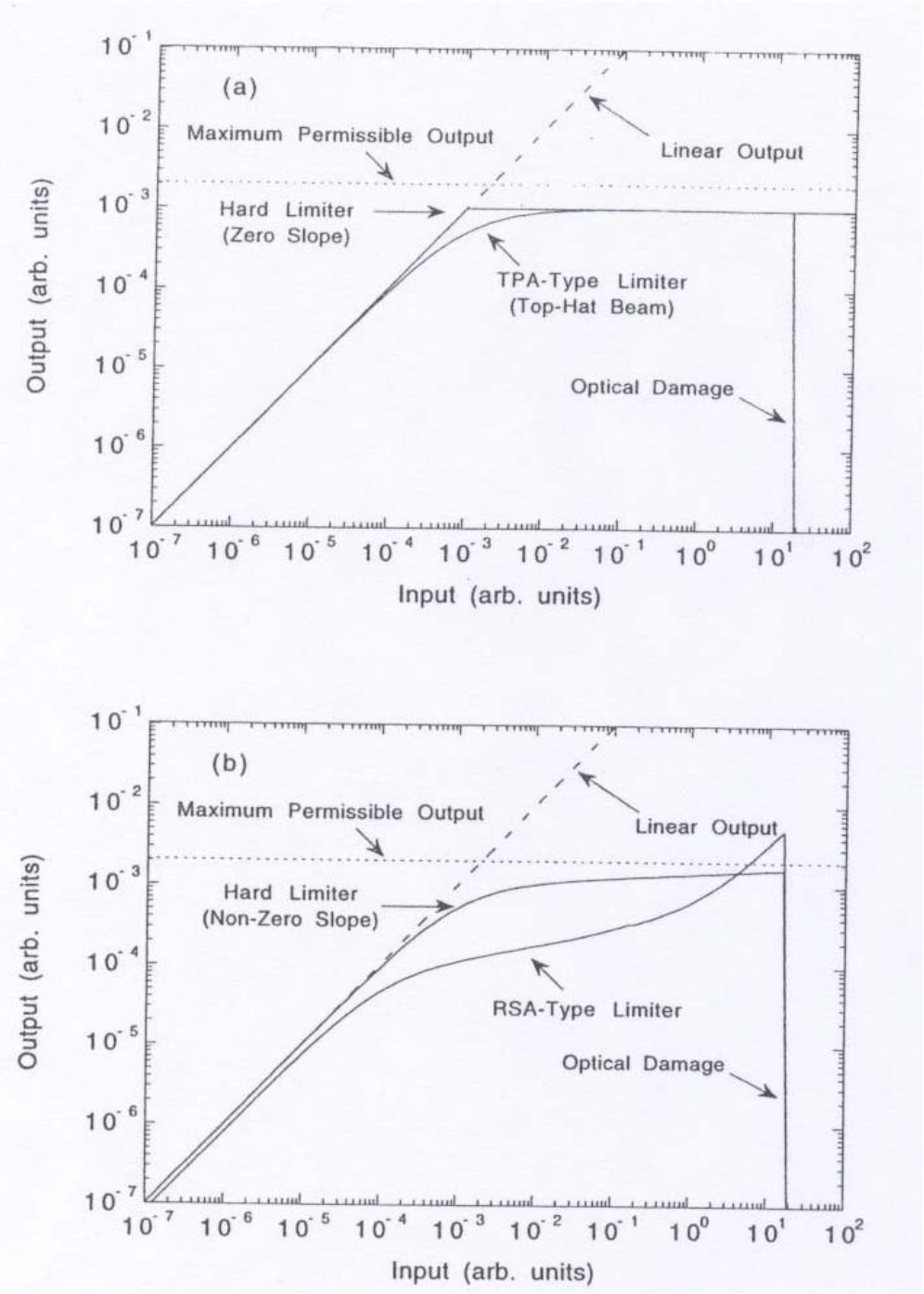

Figure 1.4.[22] Input-output characteristics of an optical limiter. (a) Ideal optical limiter. (b) Realistic optical

In the case of energy absorbing optical limiters, no aperture is needed in front of the detector. In general, TPA based OL devices offer three main advantages. First, the initial or linear transmissivity can be high because, for relatively weak input signals, TPA can be neglected and the nonlinear medium can be almost completely transparent. Second, the temporal response of the nonlinear medium can be fast because of the instantaneous nature of the TPA process. Based on the second advantage, the TPA mechanism is suitable not only for power limiting but also for reshaping optical pulses and stabilizing fast peak-power fluctuations[25]. Third, TPA retains high beam quality for the transmitted signal. These criteria lead us to investigate optical limiting properties of various materials based on their two-photon absorption and nonlinear refraction characteristics.

1.5. Optical switches

In general, an optical switch can be thought of as a device that allows the redirection of optical pulses using parameters such as intensity, polarization, wavelength and so on. Ultrafast optical switches are of significant interest for a range of applications including three-dimensional high-density optical computing, optical communications, optical electronics and optical sensing. Such variety of applications in turn imposes some restraint on the optical switch in terms of the switching time and the number of switch ports. Although there exist a wide range of optical switches, there has been increasing demand for all-optical devices since their switching rates can be in the pico to femtosecond range. The simplest all-optical switch corresponds to the Mach-Zehnder interferometer illustrated in Fig. 1.5 a). In this geometry, an optical waveguide is split into two branches. One arm is made of a linear material while the other arm is nonlinear. If we consider the simplistic case where only a signal field of amplitude E_s is applied to the device, we will show that this input pulse will be directed to one or the other output port depending on its intensity. Assuming symmetry of the beam splitters (same amplitude and reflection coefficients r and t), the coefficients are given by:

$$r = i\sqrt{R} \text{ and } t = \sqrt{T} \text{ with } R + T = 1 \tag{1.14}$$

The field at output port 1 is given by

$$E_1 = E_s(rt + rte^{i\phi_{NL}}) \tag{1.15}$$

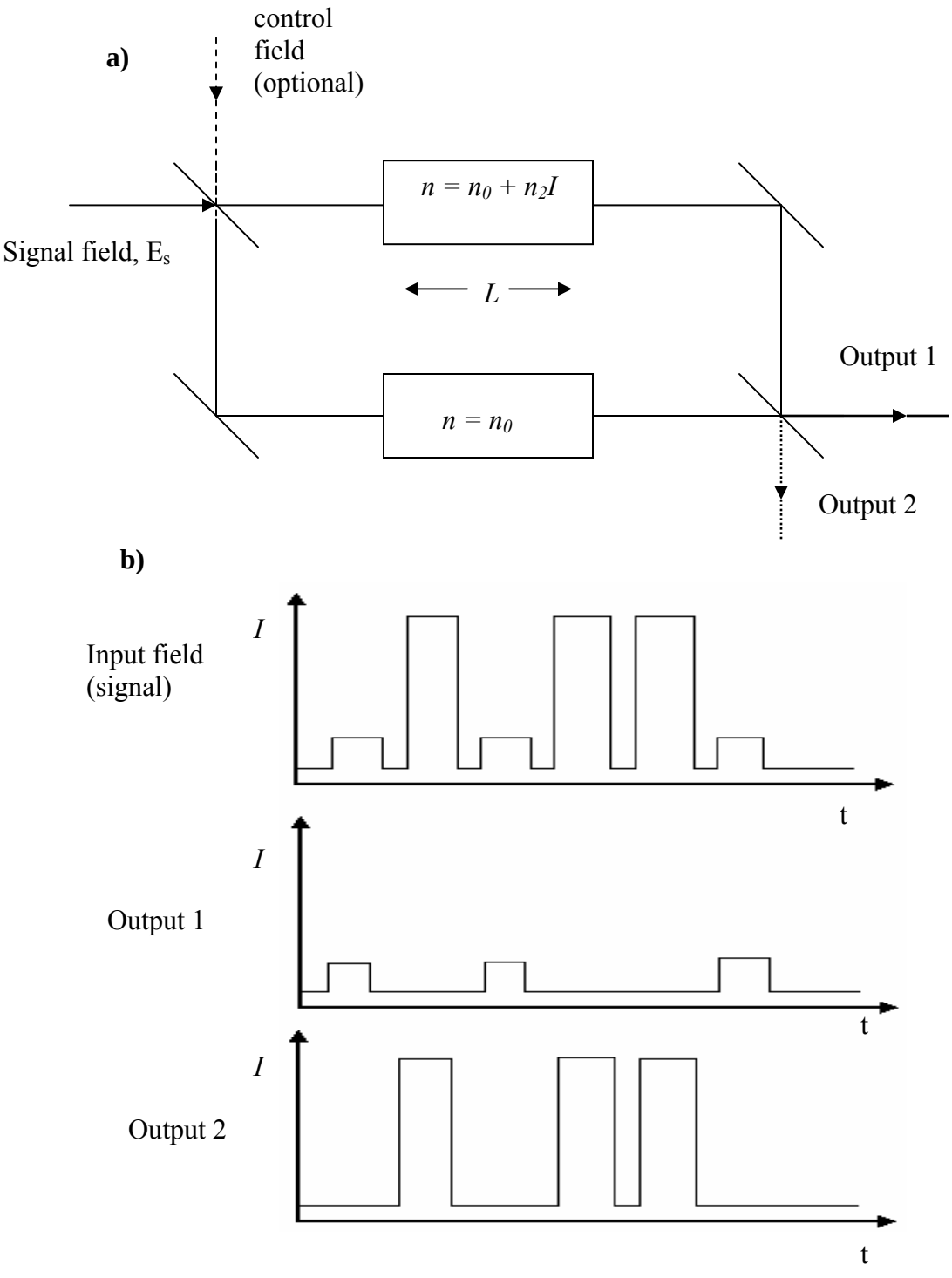

Fig 1.5 a) Configuration and b) Input-output illustration of an all-optical switch

with $$\phi_{NL} = n_2(\omega/c)IL = n_2(\omega/c)\,|t|^2\,(n_0 c/2\pi)\,|E_s|^2\,L \qquad (1.16)$$

Recalling $\cos\theta = (e^{i\theta} + e^{-i\theta})/2$, the intensity at output port 1 is then proportional to

$$|E_1|^2 = 2\,|E_s|^2\,RT(1+\cos\phi_{NL}) \qquad (1.17)$$

Similarly, the intensity at output port 2 is given by:

$$E_2 = E_s(r^2 + t^2 e^{i\phi_{NL}}) \qquad (1.18)$$

while the intensity at output port 2 is proportional to

$$|E_2|^2 = |E_s|^2\,[R^2 + T^2 - 2RT\cos\phi_{NL} \qquad (1.19)$$

Plotting equations (1.18) and (1.19), one realizes that a nonlinear phase-shift of π radians is required in order to produce a high-contrast all-optical switch. The requirement that the nonlinear phase-shift be very close to π radians is common to a broad range of all-optical switching devices.

It is obvious that the above mentioned nonlinear phase shift must be applied by the nonlinear branch of the device. If the branch includes a nonlinear material that displays some linear absorption, equation 1.16 becomes

$$\phi_{NL} = n_2(\omega/c)\int_0^L I(z)dz \tag{1.20}$$

which integrated with $I(z) = I_0 e^{-\alpha z}$ (1.21)

becomes $\phi_{NL} = n_2(\omega/c) I_0 L_{Eff}$ (1.22)

where $L_{Eff} = \dfrac{1 - e^{-\alpha L}}{\alpha}$ (1.23)

In the event that the material also displays two-photon absorption, the expression for the absorption coefficient becomes

$$\alpha = \alpha_0 + \beta I \tag{1.24}$$

and the nonlinear refractive index n_2 of the material and the two-photon absorption coefficient β will play opposite roles in the overall nonlinear phase-shift. Two-photon absorption is often a major problem in the design of all-optical switching devices. It will be seen in chapter V that the system we propose as an optical switching device shows very limited TPA behavior.

1.6. The importance of glasses, crystals and nanostructures in Photonic devices

1.6.1. Glasses and Crystals

In the realm of spectroscopy and nonlinear optics, specialty optical crystals and glasses play an increasingly important role and have proven to be an indispensable factor in the advancement of laser technology. Applications for these materials include transparent bulk optics (*waveplates, lenses, prisms, windows, beamsplitters, nonlinear crystals*, etc.), optical fibers, and thin film coatings (*anti-reflective, neutral density filters*, etc.). These applications for the most part require high density and high purity of the materials. High density means that the voids in the material be very small so that scattering is minimized, while high purity is necessary to ensure low absorption throughout the intrinsic transmission region. While defects and inclusions in optical materials are for the most part undesirable, some materials can be purposely doped or combined with other materials in order to serve a specific purpose like controlling spontaneous emission, regenerating and amplifying pulses, trap photons, and make enhanced lasing medium such as laser crystals (*Forsterite, NaF, Nd:YLF*).

The study of glasses and crystals is almost concurrent with the invention of the laser, since it was realized at an early stage that available glassy materials could not handle the increasingly higher power densities delivered by the lasers. However, no matter how plentiful the amount of research dedicated to optical glasses, they fundamentally tackle

three main groups of problems: laser induced damage (LID)[26], enhancement of the laser damage threshold (LDT)[27], imaging and photoluminescence signature of key defects[28].

In the group of glassy materials, fused silica is a very important and versatile optical element. It is the most prevalent material for optical window, with a cutoff transmission around 8 eV. When highly polished, fused silica offers high reflectivity uncoated in the extreme UV at grazing angles due to total external reflection. Based on its OH content, fused silica or amorphous S_iO_2 can be divided into four types: type I and type II have 5 to 20 ppm and 150 to 400 ppm by weight of OH respectively. Both have Al and Na impurities limiting their UV cutoff to 5.4 and 7.2 eV. An oxygen treatment of type II fused silica eliminates the transmission dip observed at 5.2 eV. Type III (*Corning 7940 studied in chapter 3*) is a synthetic fused silica formed by flame hydrolysis while type IV is formed by plasma deposition. Type III has approximately 200 to 1200 ppm OH and type IV has only 3 ppm OH. This trend illustrates the steady progress towards higher performing optical windows. The photoluminescence spectra of fused silica presents PL bands at 1.9, 2.8 4.3 and 6.7 eV. Those bands are closely related to intrinsic defects and are showed to be enhanced via radiation damage[29]. Bulk transparent materials or windows damage catastrophically for Laser Damage Thresholds from 1 to 30 J/cm^2 and intensities above 10^9 W/cm^2 [30]. Laser radiation damage results either from increased absorption of transiently populated excited states or from lattice heating and melting. The absorption of UV light leads to the creation of electron-hole pairs that recombines in times from femtoseconds to microseconds depending on band structure and the density

and cross section of the recombination sites. In general, the number of electro-hole pairs created by a photon of energy E is given by $E/2.8 * E_g$, where E_g is the energy gap.

1.6.2. **Nanostructures**

Nanotechnology has become the science of the 21st century because of the foreseen potential to address many issues that mankind somehow faces today. It is established that the potential impact of Nanotechnology on the health and lives of people[31] could be as significant as the combined influences of microelectronics, medical imaging, computer-aided engineering, and man-made polymers altogether. Some benefits of nanostructuring include lighter, stronger, and programmable materials; lower failure rates that will reduce the cost of material life; higher speed and power reduction in information processing devices. In the area of nano-opto-electronics, topics include developing nanometer structures for minuscule transistors and memory chips that will improve computer speed and efficiency by factor of millions; expansion of mass storage electronics to multi-terabit memory capacity that will increase the memory storage per unit surface a thousand fold and make data available on a pinhead; changes in communication paradigm will increase bandwidth a hundred times. All these applications rely on the very fact that nanotechnology brings a different approach to material tailoring and device structuring.

The essence of nanotechnology is the ability to work at the molecular level, atom by atom, to create large structures with fundamentally new molecular organization.

Compared to the behavior of isolated molecules of about 1 nm or of bulk materials, behavior of structural features in the range of about 10^{-9} to 10^{-7} m (1 to 100 nm) exhibit important changes. The new observed phenomena are not due merely to the size reduction, but to new occurrences intrinsic to or becoming predominant at the nanoscale. These phenomena include but are not limited to predominance of interfacial phenomena, quantum mechanical behavior and size confinement.

With respect to nonlinear optical devices, one of the goals in the use of quantum confinement is to optimize the optical nonlinearity per valence electron in a given frequency or time range. The success of quantum confinement relies on the possibility of artificially modifying the material characteristic, and selectively enhancing or suppressing certain polarization mechanisms with respect to the unconfined bulk material. This is achieved by increasing either the interaction length or the optical nonlinearity. These two confinement approaches cannot be implemented simultaneously in the same material since they address aspects incompatible with each other. For example, confinement by interaction length involves trapping of the interacting optical beam in guides or resonators whose dimension must be larger than the optical wavelength. The second approach to confinement consists in enhancing the optical nonlinearities of materials with very delocalized valence electrons, like metals, semiconductors, or conjugated polymers, by artificially confining the valence electrons in regions much shorter than the natural delocalization length in the bulk. Its most conspicuous feature is the appearance of discrete optical resonances whose position, oscillator strength and dynamics depend on the degree of the confinement. The ratio

between the nanocrystal radius a and the bulk-exciton radius a_x determines the degree of confinement. In general, three degrees of confinement exist. In the strong confinement regime ($a/a_x >> 1$), the Coulomb electron-hole interaction is negligibly small. This is due to the fact that the Coulomb interaction scales with the nanocrystal (NC) radius as a^{-1}, whereas confinement energies are proportional to a^{-2}. Electron and hole can then be treated as independent particles[32]. In the weak confinement regime ($a/a_x << 1$), the electron and hole motions are strongly correlated via the Coulomb interaction and NC energy spectra are determined by quantization of the motion of the exciton center of mass. In the case of intermediate confinement ($a/a_x \sim 1$), the energy structures in a NC material will be determined by the interplay between Coulomb *e-h* interaction.

As can be seen from the previous argument, excitonic behavior occupies a center stage in this report. In this thesis, our main focus has been to modify the optical nonlinearities of the studied nanostructured materials by enhancing excitonic interaction.

1.7. Thesis Overview

This portion summarizes the organizational structure of the thesis. Considering that the first two report chapters involve research performed on bulk materials and the last two report studies of nanostructures, one could be rightfully inclined to claim that this thesis encompasses research performed on both bulk materials and nanostructures. However, the properties studied are common to each chapter, mainly the nonlinear transmission, the nonlinear absorption and the nonlinear refraction properties. This thesis is organized such that in each report chapter, we start off with an extensive introduction of the material being investigated, stating its importance, its present and future use, key characteristics and possible impact in the industry. This introduction section is followed by a general background research on the topic, stressing on the status of previous works if any, along with the physics and dynamics involved. We then lay out our experimental setup followed by the material preparation section. In the next section, we report our results and then discuss the findings before concluding the research. Specifically, *Chapter 2* starts with a survey of our laboratory facilities along with the different experimental setups and techniques currently in use for ultrafast nonlinear spectroscopy. In this chapter, for example, one can find a detailed description of the Zscan technique extensively used to characterize the third order nonlinear susceptibility of materials. Our experimental investigation begins in *Chapter 3* with the report of nonlinear optical absorption in laser induced damaged sections of fused silica substrates. We begin this chapter with a review of the mechanisms of damage initiation and growth in fused silica. This section gives way to optical transmission measurements performed on both pristine polished silica

samples and in laser modified regions of fused silica substrates at different wavelengths. We conclude this investigation with a study of annealing effects on the transmission of high intensity UV light. In *Chapter 4*, we build on the previously established knowledge of defect-enhanced energy absorption to propose a two-photon absorption-based imaging technique allowing to visualize the relative position of absorbing centers in KDP crystals. This study encompasses a wide range of doped and undoped KDP samples and concludes our investigations of nonlinear absorption in bulk materials. Structures with large optical nonlinearities and fast responses are much needed for a breakthrough in optical information processing. The nonlinear optical properties of Cadmium Sulfide quantum dots in a variety of dendritic nanocavities are reported in *Chapter 5*. The first section of this chapter contains a review of the physics of quantum confined structures, stressing on the notions of excitons in both semiconductors and organic polymers. Finally, *Chapter 6* covers our investigations of the nonlinear transmission properties of composite films of single-wall carbon nanotubes with conductive polymers. Part photonic crystal, part nanocomposite, and part polymer, the new samples have potential of providing with some new interesting electrical and optical properties. We performed optical transmission measurements to investigate the contribution of the different components of the new hybrid material. Their potential use in novel optoelectronic devices has also been assessed.

References

1. Stavros G. Demos, Mike Staggs, Kaoru Minoshima and James Fujimoto, *Characterization of laser induced damage sites in optical components*, Optics Express 1444, Vol 10, No 25
2. L. Martin-Samos, Y. Limoge, N. Richard, J. P. Crocombette, G. Roma, E. Anglada and E. Artacho, *Europhys. Lett.*, **66**, pp. 680–686 (2004)
3. T. Mohanty, N. C. Mishra, S. V. Bhat, P. K. Basu and D. Kanjilal, *J. Phys. D: Appl. Phys.* **36,** 3151–3155 (2003)
4. N. F. Borrelli, Charlene Smith, Douglas C. Allan, and T. P. Seward III, *J. Opt. Soc. Am. B* Vol. **14**, No. 7, 1606 (1997)
5. M. A. Stevens-Kalceff, A. Stesmans, Joe Wong, *App. Phys. Lett.* **80**, No 54, (2002)
6. R.A. Ganeev, I.A. Kulagin, A.I. Ryasnyansky, R.I. Tugushev, T. Usmanov, Optics Communications **229**, 403–412 (2004)
7. N. L. Boling, M. D. Crisp, and G. Dube, Applied Optics 12, No 4 (1973)
8. Richard L. Sutherland, *Handbook of Nonlinear Optics*, 2nd Edition (2003)
9. Guang S. He, Song H. Liu, *The physics of Nonlinear Optics*, World Scientific (1999)
10. Nguyen Que Huong and Joseph L. Birman, *Phys. Rev. B* **61**, No 19 (1999)
11. M. Sheik-Bahae, A.A. Said, and E.W. Van Stryland, *High-sensitivity, single-beam n_2 measurements*, Opt. Lett., **14**, 955-957 (1989)

12. Paras N. Prasad and David J. Williams, *Nonlinear Optical Properties of Organic molecules and polymers* (1991)
13. Govin P. Agrawal, Robert W. Boyd, *Contemporary Nonlinear Optics*, Academic Press, (1992)
14. Bahaa E. A. Saleh and Malvin Carl Teich, *Fundamentals of Photonics*, John Wiley & Sons (1991)
15. Govind P. Agrawal, *Fiber-Optic Communications Systems*, John Wiley & Sons (2002)
16. Carlo G. Someda, *Electromagnetic Waves*, Chapman & Hall (1998)
17. Robert W. Boyd, *Nonlinear Optics*, Academic Press (2003)
18. Govind Agrawal, *Applications of Nonlinear Fiber Optics*, Academic Press(2001)
19. G. L. Wood, A. A. Said, D. J. Hagan, M. J. Soileau, and E. W. Van Stryland, *Proc. Soc. Photo-Opt. Eng.* 1105:154 (1989)
20. L. W. Tutt and T. F. Boggess, *Prog. Quant. Electr.* **17**. 299 (1993)
21. J. A. Hermann and J. Staromlynska, *Int. J. Nonlin. Opt. Phys.* **2**. 271 (1993)
22. R. L. Sutherland, Handbook of Nonlinear Optics, Series Optical Engineering **52**. (1996).
23. R. Grane, K. Lewis, E. V. Stryland, and M. Khoshnevisan, Mater. Res. Soc. Proc. 374 (1995)
24. Types of Optical limiting materials (Physics of nonlinear optics Ref 9)
25. Guang S. He, Lixiang Yuan, Jayant D. Bhawalkar, and Paras N. Prasad, Applied Optics **36**, No. 15 pp3387-3392, (1997)

26. A. A. Said, T. Xia, A. Dogariu, D. J. Hagan, M. J. Soileau, E. W. Van Stryland and M. Mohebi, *Applied Optics* **34**, No. 18 (1995)

27. M.D. Feit, A.M. Rubenchik, *Mechanisms of CO_2 Laser Mitigation of Laser Damage Growth in Fused Silica*, Lawrence Livermore National Laboratory (2002)

28. Mitsuru Watanabe, Saulius Juodkazis, Hong-Bo Sun, Shigeki Matsuo, Hiroaki Misawa, Masafumi Miwa and Reizo Kaneko, *Appl. Phys. Lett.* **74**, No 26 (1999)

29. N. Bloembergen, *MRS Symp*, vol 51, (1985)

30. S. C. Jones, P. Braulich, R. T. Casper, X. Shen, and P. Kelly, Opt. Engr., vol 28, P-1039, (1989)

Chapter II

Ultrafast Nonlinear Spectroscopy and Techniques

Although there exists a wide variety of spectroscopic methods based on different techniques of linear and nonlinear optical spectroscopy, ultrafast spectroscopy provides a useful tool for monitoring the real-time photophysics of atoms and molecules. The absorption of energy from a laser pulse triggers a series of processes occurring on a very short time scale (10^{-15}-10^{-10}sec). After excitation, the system can undergo several changes, involving redistribution of the energy, loss of coherence, formation of intermediates, etc[1]… By monitoring the evolution of those changes, one can completely understand the specific light-matter interactions involved. Since the temporal evolutions are extremely fast, it is therefore necessary to probe the system with time-scales shorter than the times it takes for them to evolve. Ultrafast nonlinear spectroscopy essentially studies the behavior of a sample perturbed by a very short and very intense optical pulse, providing an insight on the ultrafast occurring responses. Whether the sample is a semiconductor where we would be interested in a change of the energy band structure through band-gap renormalization or a change in the exciton binding energy, a molecule where we would be monitoring photochemical transformations or a crystal whose refractive index would change under the action of an intense light pulse causing its nonlinear properties to also change, ultrafast spectroscopy provides us with the means to measure those changes and determine their characteristic time scales.

A basic spectroscopic scheme is illustrated in fig. 2.1. A well characterized input beam interacts with a material, and the resulting output beam is deconvolved or compared to the input in order to determine the hidden properties of the material. Common properties include but are not limited to linear absorption coefficient, energy gap, dielectric

constant, nonlinear susceptibilities, bond length, density, dipole moment and two-photon absorption coefficient of the material.

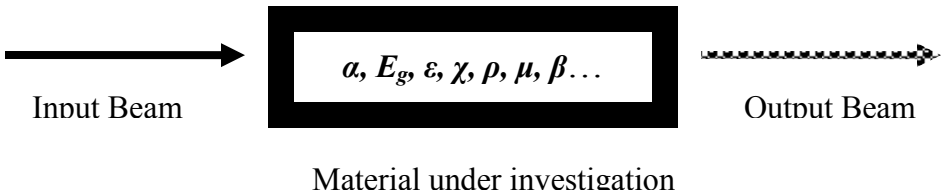

Fig. 2.1 Principle of spectroscopic measurements

Different methods exist to characterize the pulse duration, the spectrum and temporal profile and the phase of optical pulses. In the following sections we will describe the different spectroscopic tools used. For example, for our femtosecond laser system, the pulse duration of the optical pulses is measured using autocorrelation technique; the spectrum and phase profiles can be resolved using the *FROG*[2] technique. The single beam Zscan[3] technique is used to determine the third-order susceptibility of a sample and the time-resolved pump-probe technique is used to investigate the lifetime of the excited-state. We introduce this review by first laying out the different ultrafast laser systems used to perform the experiments.

2.1. Experimental apparatus

The spectroscopic measurements were performed using two ultrafast laser systems. An Nd:YAG picosecond laser generating wavelengths at 1064, 532 and 355 nm and a femtosecond system fundamentally at 800nm, whose second and third harmonic would generate 400 and 266 nm respectively. For more tunability, an optical parametric amplifier is used in conjunction with the femtosecond system allowing a tuning range from 400 nm to 2μm.

2.1.1. Femtosecond Spectroscopy

The femtosecond system used in our experiments is illustrated in Fig. 2.2. The first element is an all solid-state, fiber-diode pumped, visible CW laser outputting 5W at 532 nm. In this laser, two fiber-coupled diode bar laser modules pump an Nd:YVO4 laser crystal emitting 1064 nm. This output goes through a frequency doubling arm made of a non-critically phase-matched LBO crystal that converts the 1064 nm light into 532nm. The 5W output of this laser is then used to pump an oscillator.

The oscillator is a solid-state mode-locked Ti:Sapphire laser. The Ti:Sapphire crystal presents a peak absorption at 500 nm and a peak emission at 800 nm. The passive mode-locking process is assured by an acousto-optic modulator. The folded resonator geometry of the oscillator delivers ultrashort pulses of 80 fs pulse duration, 82 MHz repetition rate and circa 620 mW output power at 800 nm.

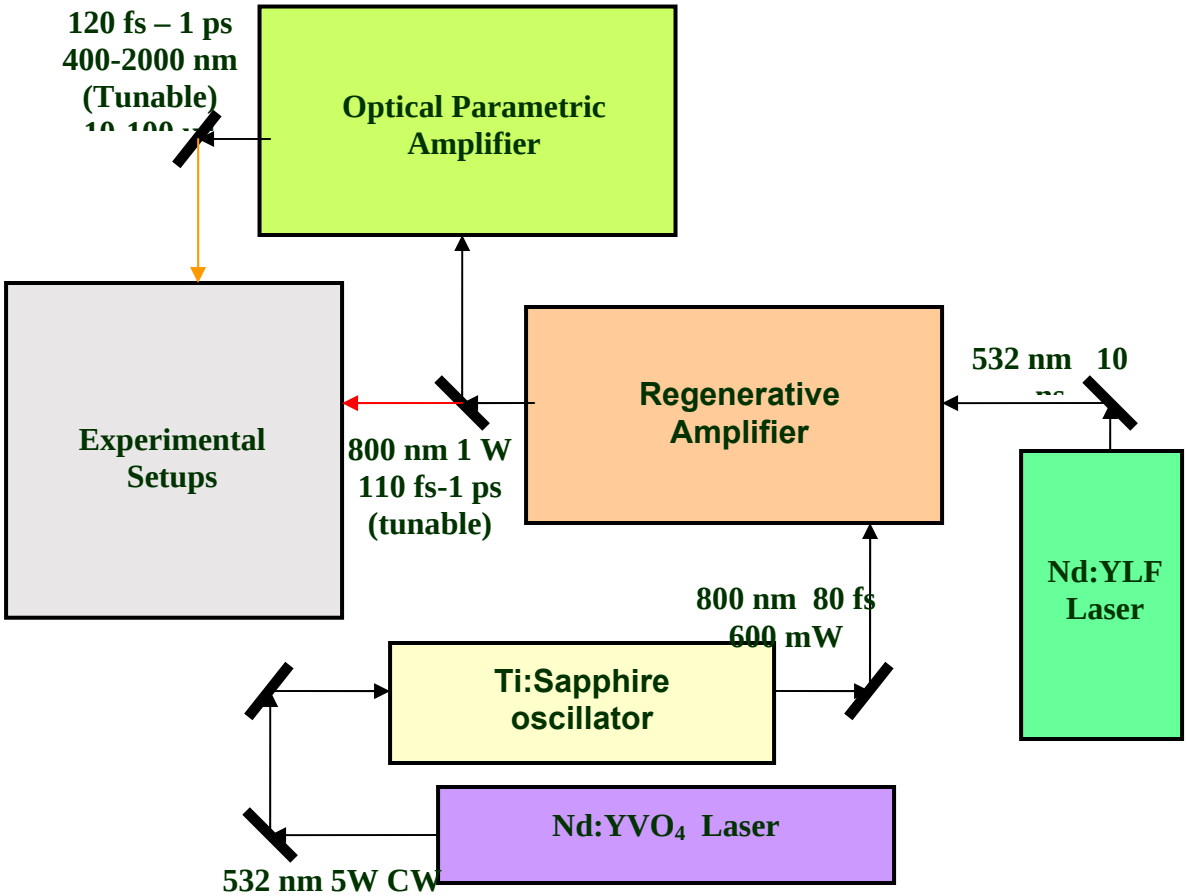

Fig. 2.2 Experimental layout of the Ti:Sapphire femtosecond system

The output of the oscillator is used as a seed beam for the regenerative amplifier. The amplifying process is based on the principle of chirp pulse amplification (CPA) and can be broken down into three stages: a stretcher, a regenerative amplifier, and a compressor. First the incoming pulse is incident on a diffraction grating causing the different frequencies to disperse. The grating is configured so that the bluer frequency components have to travel further through the stretcher than the redder components, as a result the redder frequency components exit the stretcher first thus stretching the pulse. The stretched seed then enters the regenerative amplifier which is pumped by 12W of a 10ns frequency doubled Nd:YLF laser at 527 nm. Both the pump pulse and the seed are focused and overlapped onto the Ti:Sappire crystal. The seed completes a number of round trips inside the cavity, extracting the energy from the nanosecond pump pulse. The amplified pulse is then extracted and sent to the compression module where another set of gratings recompresses the pulse to about 120 femtosecond and extract it out of the laser. The regenerative amplifier provides 800nm wavelength output at 1 KHz repetition rate and allows to change the pulse duration of the beam from 100fs to about 2ps. At the end of the amplification process, the energy per pulse will increase from nearly 8 nJ to over 1 mJ.

The optical parametric amplifier (*OPA*) makes use of frequency down conversion and harmonics generation to deliver an output wavelength tunable from the infrared to the near ultraviolet (2μm to 400 nm). *Figure 2.3* illustrates the physical geometry of the OPA. Using the output of the Ti:Sapphire amplifier, 1% of the incoming beam is used to generate a white light continuum, the rest is used for amplification purpose. The white

light continuum and the imput beam at 800 nm are frequency-down mixed in a LBO crystal to generate a tunable signal (1.03 -1.6 μm) and an idler (1.6 - 2000 μm). The wavelengths of the signal and idler can be tuned by changing the phase matching angle of the crystal and by adjusting time delay for that particular angle. Signal and idler beams can be used to generate second and fourth harmonic wavelengths by using a set of BBO crystals. One can obtain all the wavelengths between 400 nm and 2000 nm by tuning signal and idler wavelengths and by using second and fourth harmonics of these wavelengths.

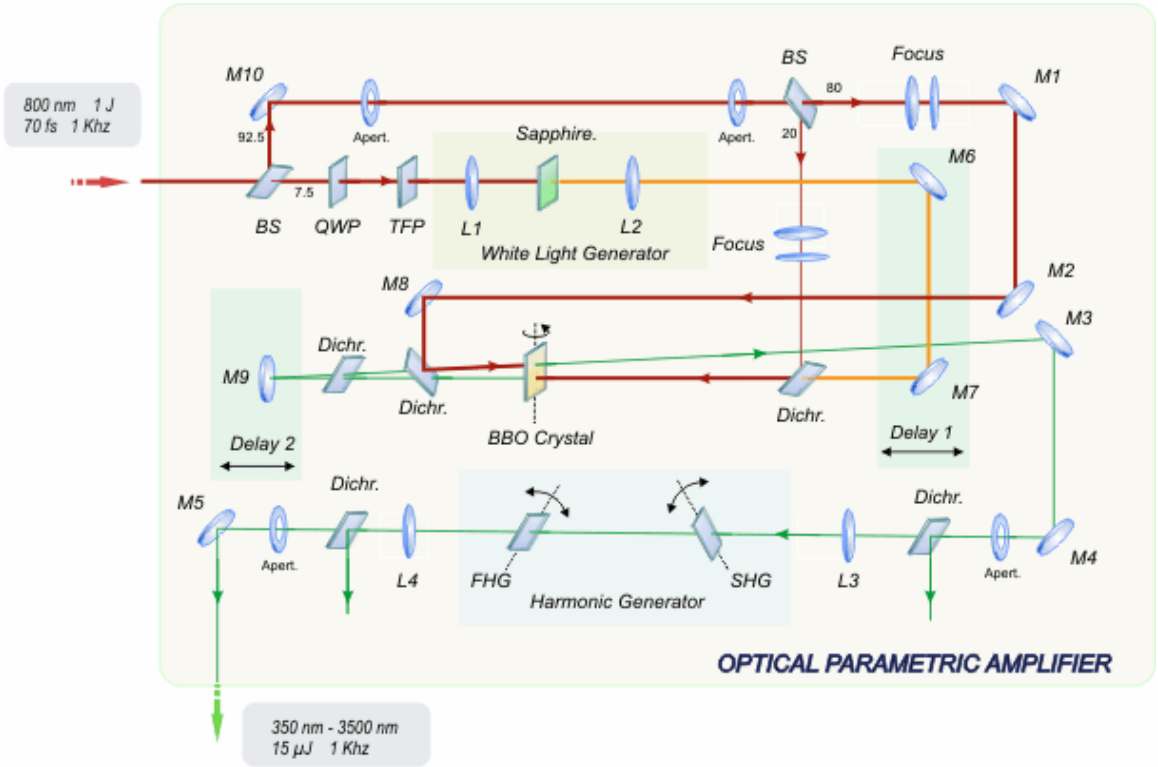

Figure 2.3 Physical representation of the Optical Parametric Amplifier (OPA)

2.1.2. Picosecond Spectroscopy

The picosecond system is a Continuum passively and actively mode-locked Nd:YAG oscillator. The compact optical bench has three main stages: an oscillator, an amplifier, and a harmonic generator. In the oscillator, a single flashlamp pumps an Nd:YAG rod that emits light at the fundamental 1064nm. A passive mode-locking dye solution on the end mirror allows for power build up in the cavity and pulsing. This passive system is enhanced by an active mode-locking system made of an acousto-optic modulator. A Marx board driven electro-optic Pockels cell triggered by a photodiode (pulse selector) ensures the pulse selection process. The photodiode senses for intensity buildup inside the cavity, sends a trigger signal to the Marx bench board which applies a 4 KV voltage to the pockel cell, changing the polarization of the pulse. The pulse is then extracted from the oscillator via a polarizer and sent to the amplifying stage.

The amplifying stage is made of a 3/8 inch diameter amplifier crystal pumped by two flashlamps arranged in a close coupled configuration. A telescope is placed before the amplifier for beam expansion. The amplified pulse is then incident on a harmonic generation crystal (type II $KD^{*}P$) and at the output, both the 1064 nm fundamental and 532 nm second harmonic can be used for experiments or for third harmonic generation.

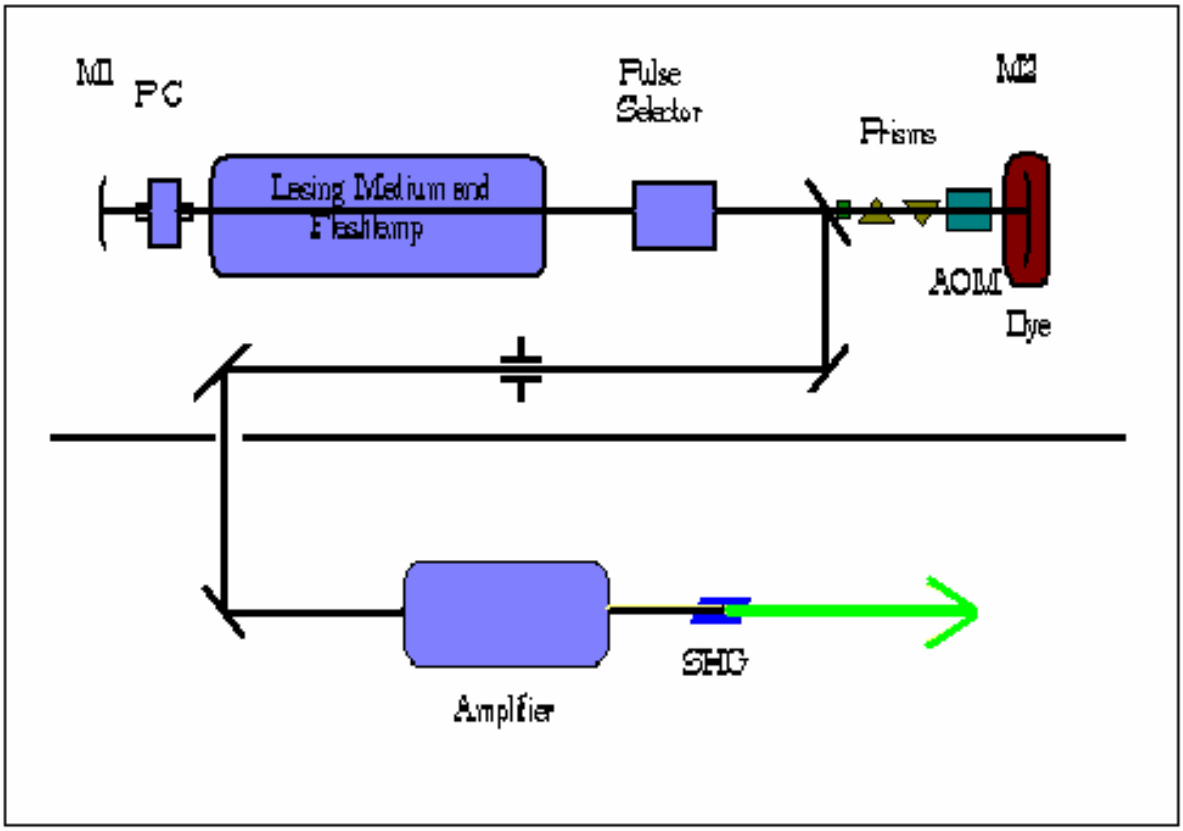

Fig. 2.4 Experimental layout of the picosecond system

2.2. Measurement and characteristics of ultrafast pulses

The advent of femtosecond lasers brought a new problem of measurement. The direct combination of a photodiode and an oscilloscope were no longer adequate to temporally resolve the ultrashort pulses generated. The fastest optical detectors have response times $\sim 10^{-11}$ seconds and so they are unable to measure pulse durations shorter than a few tens of picoseconds. The only thing fast enough to measure these pulses would be the pulse itself.

2.2.1. Pulse duration measurement: Autocorrelation

The technique of autocorrelation allows the conversion of the difficult problem of measuring time scales in the order of 100's of femtosecond into the much easier task of measuring lengths in the order of microns. Most photodetectors have very slow rise and fall times in the order of nanoseconds. In order to make time-domain measurements or to resolve ultrashort laser pulses, it is necessary to slow down the pulse, meaning to delay the pulse in time using a translation stage or a retro-reflector. Since light travels 300 μm per ps, 300 μm of mirror displacement on a delay stage yields a delay of 2 ps.

Correlation techniques can be classified in a number of ways; the first, *cross* correlation, is when one or more distinct signals are correlated. The second is *auto*correlation where two or more replicas (formed by splitting a pulse into equal parts) of a single pulse are used. The experimental arrangement of our second harmonic generation autocorrelator is illustrated in *Figure 2.5*.

The output pulse from the regenerative amplifier passes through a Michelson-type delay arrangement where one of the arms is delayed with respect to the other. The pulses are

then focused onto a KDP crystal. When their overlap is both spatial and temporal, and the phase-matching condition (*Δk=0*) is fulfilled, a second-harmonic signal is generated at the KDP crystal. Moving a mirror backward by a distance *L* in general yields a delay of $\tau=2L/c$

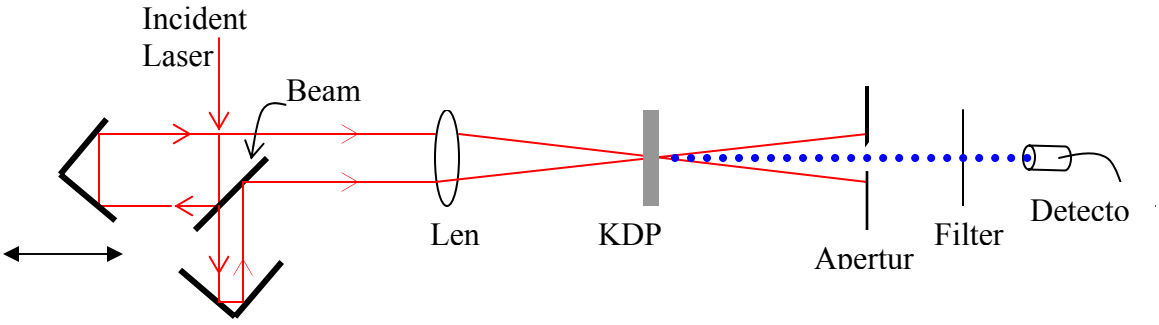

Fig. 2.5 Autocorrelation setup for pulse duration determination

For a travel difference $\Delta S=S_1-S_2$, the time difference between the two pulses is given by $\tau=\Delta S/c$. When the path lengths for the two pulses are equal, the pulses will exactly coincide at the crystal and the amount of second harmonic light generated will be a maximum. This intensity will decrease as the time delay increases between the two arms. In fact, the autocorrelation trace is made up from the second harmonic produced from many pulses, each subject to a different delay time.

The photodetector detects the second harmonic light generated in the nonlinear crystal and the resultant electrical signal is integrated over a period that is long compared to the pulse duration. The average power of the second harmonic light of the recombined beam is then recorded as a function of delay. The pulse duration of the laser can be obtained by deconvolution. For a Gaussian pulse $\Delta\tau_A{}^{FWHM} = 1.41\ \Delta\tau_p{}^{FWHM}$. The autocorrelation

produced has a background level due to the signals from each arm, and a peak corresponding to the second harmonic generation when the pulses overlap. The ratio of the peak to the background is well defined for a perfect modelocked pulse; hence, the autocorrelation can also be used to adjust the laser system for optimum performance[4].

2.3. Nonlinear Characterization of Materials

The nonlinear index of refraction is a result of several diverse microscopic physical effects that contribute to a macroscopic response. As it was shown in equation (*1.12*) for third-order nonlinearities, the response of the materials shows a cubic relationship with the Electric field of the impinging light wave. The third-order nonlinear susceptibility is a parameter that quantifies the response of the material in term of the third degree polarization. It is therefore responsible for a rich array of phenomena that allow useful probing of materials and easy implementation into device applications. We have seen, for example, that the use of light intensity-dependent transmission properties of materials, also known as optical limiters can provide added protection to the human eyes or optoelectronic sensors from unwanted high intensity sources of radiation[5]. For this and other important applications, it is necessary to establish a catalogue of materials with their respective susceptibilities.

Although the characterization of the nonlinear susceptibility is not a straight forward process, a number of experimental techniques has been proposed to obtain information about the dispersion, , the response time, the sign and the contributions of both the real

and the imaginary parts of the nonlinear optical response. In the following sections, we will investigate the methods relevant to this thesis.

2.3.1. Measurement of $\chi^{(3)}$: Close Aperture Z-scan Technique

The Z-scan technique[3] is a straight forward application of spatial beam distortion, where phase distortion is transformed into amplitude distortion during beam propagation. It's a simple and highly sensitive single beam technique where by moving a sample in and out of focus of a tightly focused Gaussian beam, a simple linear relationship between the observed transmittance changes and the induced phase distortion allows to compute both the magnitude and sign of refractive nonlinearities (nonlinear absorption and nonlinear refraction coefficients). The nonlinear susceptibility has both a real part associated with the nonlinear refraction coefficient n_2 , and an imaginary part connected to the nonlinear absorption coefficient β. The close aperture Z-scan technique probes the refractive component of the nonlinearity, while the open aperture Z-scan determines the absorptive component of the nonlinearity.

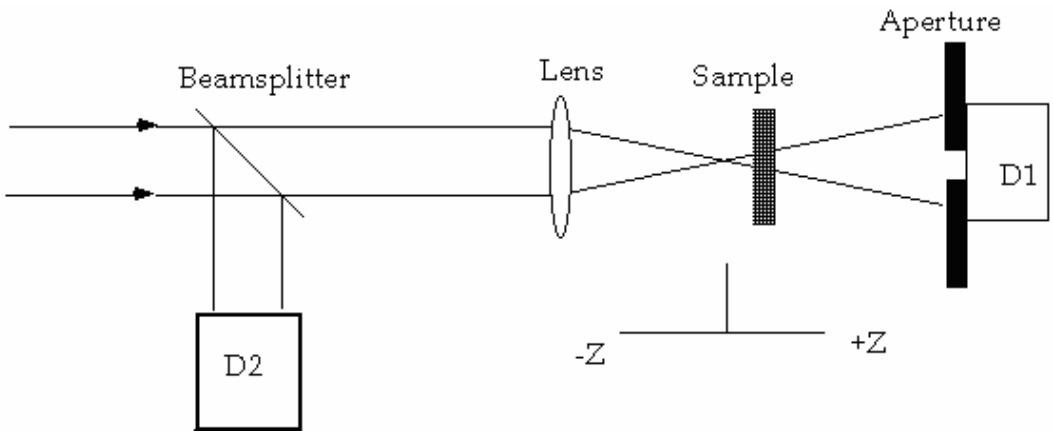

Fig.2.6. The Z-scan experimental setup

The Z-scan apparatus is illustrated in *Figure 2.6*. In this geometry, either an open aperture or a close aperture Z-scan can be performed. In the close aperture Z-scan, the transmittance of a nonlinear medium is monitored through a finite aperture in the far field as a function of the sample position *z* measured with respect to the focal plane. Assuming the material has a positive nonlinearity and is very thin (a thickness less than the diffraction length of the focused beam), as the sample is translated from -z through the focal point to +z, its behavior will be that of a thin lens with varying focal length. When the sample is at –z and far from the focal point, since the intensity is relatively low, little nonlinear refraction occurs and the transmittance remains constant. As the sample is moved towards the focus, the increased irradiance leads to a positive lensing effect that tends to augment diffraction, and the aperture transmittance in the far-field is reduced. When the sample is at the +z side of the focus, the positive lensing effect after the focus

tends to collimated the beam, thus increasing the aperture transmittance in the far-field. This implies that there will be a null at the focus.

For materials with a negative (*positive*) n_2, the profile of the Z-scan transmittance curve will consist of a peak (*valley*) followed by a valley (*peak*) as the sample is translated from -*z* to +*z*. Figure 2.6 shows the valley-peak (*v*-*p*) sequence for positive nonlinearity and a peak-valley (*p*-*v*) sequence for negative nonlinearity. One extremely useful feature of the Z-scan technique is that the sign of the nonlinearity can be deducted immediately from the resulting curve.

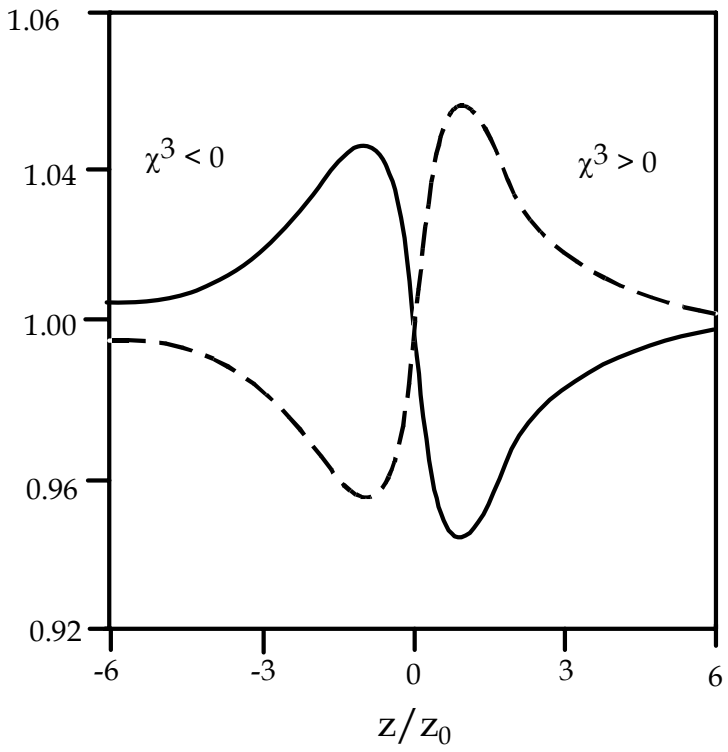

Fig. 2.7 Typical close aperture Z-scan profile

In general, two nonlinear coefficients are used in order to describe the refractive index change of a medium possessing the cubic nonlinearity $\chi^{(3)}(\omega; \omega, -\omega, \omega)$. These coefficients are connected to the refractive index variation via field amplitude (E) and intensity (I)

$$n = n_0 + n_2 \frac{|E|^2}{2} = n_0 + \gamma I \qquad (2.1)$$

where n_0 and n_2 are respectively the linear and nonlinear refractive indices. E and I are connected through the relationship $|E|^2 = (\frac{8\pi}{cn_0})I$ which also shows the connection between n_2 and γ. n_2 and γ are usually measured in esu and $W^{-1}.m^2$, respectively and are related through $n_2 = cn_0\gamma / 40\pi$. The nonlinear susceptibility $\chi^{(3)}$ and n_2 are connected by a simple expression $n_2 = (3\pi / n_0)\chi^{(3)}$.

Assuming a Gaussian beam traveling in +z direction, the magnitude of the E field can be written as:

$$|E(z,r,t)| = E_0(t)\frac{\omega_0}{\omega(z)}\exp[-\frac{r^2}{\omega^2(z)}] \qquad (2.2)$$

where $\omega^2(z) = \omega_0^2(1 + z^2 / z_0^2)$ is the beam waist radius at z, $z_0 = k\omega_0^2 / 2$ is the diffraction length of the beam, $k=2\pi/\lambda$, and λ is the laser wavelength.

When the medium length is short enough so that changes in the beam diameter in the sample due to nonlinear refraction or diffraction can be neglected, the sample is considered thin. Such an assumption assumes $L << z_0 / \Delta\Phi(0)$ and greatly simplifies the

problem. Inside the sample, the amplitude and nonlinear phase change $\Delta\Phi$ of the electric field are governed by

$$\frac{d\Delta\Phi}{dz} = (2\pi/\lambda)\Delta n \quad \text{and} \quad \frac{d\,|E|}{dz} = -\alpha/2\,|E| \tag{2.3}$$

By solving Equations 2.3, one can easily find the nonlinear phase shift $\Delta\Phi$ at the exit surface of the sample

$$\Delta\Phi(z,r,t) = \frac{\Delta\Phi_0}{1+z^2/z_0^2}\exp[-2r^2/\omega^2(z)] \tag{2.4}$$

with the on-axis phase shift at the focus defined as

$$\Delta\Phi_0(t) = \frac{2\pi}{\lambda}\Delta n_0(t)\frac{1-e^{-\alpha L}}{\alpha} \tag{2.5}$$

where L is the sample length, $\frac{1-e^{-\alpha L}}{\alpha} = L_{eff}$ the effective length of the sample, and Δn_0(t) is the instantaneous on-axis index change at the focus ($z=0$). The electric field E_e at the exit surface of the sample z_1 now contains the nonlinear phase distortion term:

$$E_e(z_1,r,t) = E(z_1,r,t)e^{-\alpha L/2}e^{i\Delta\Phi(z_1,r,t)} \tag{2.6}$$

In the following, we will use a Gaussian decomposition method[6] where the complex electric field at the exit plan of the sample is decomposed into a summation of Gaussian beams via a Taylor series expansion of the nonlinear phase term

$$e^{i\Delta\Phi(z_1,r,t)} = \sum_{m=0}^{\infty} \frac{[i\Delta\Phi_0(z_1,t)]^m}{m!} e^{-2mr^2/\omega^2(z_1)} \qquad (2.7)$$

By propagating each Gaussian beam to the aperture plane we obtain the resultant far-field pattern of the beam E_a at the aperture. From there, the normalized instantaneous Z-scan power transmittance is found to be

$$T(z,t) = \frac{\int_0^{r_a} |E_a(\Delta\Phi_0, r, z, t)|^2 \, rdr}{S\int_0^{\infty} |E_a(0, r, z, t)|^2 \, rdr} \qquad (2.8)$$

where r_a is the aperture radius, and S is the aperture transmittance in the linear regime with

$$S = 1 - \exp\left(-2r_a^2 / w_a^2\right) \qquad (2.9)$$

The aperture size *S* is a very important parameter in that a large aperture reduces the variations in *T(z)*, i.e. the sensitivity. This reduction is usually more prominent in the peak, where beam narrowing occurs, and results in a peak transmittance that can not exceed *(1-S)*.

The rapid acceptance of the Z-scan technique is due to the simplicity of the interpretation of the obtained results, since in most cases the index change, *Δn,* and the absorption

change, $\Delta\alpha$, can be retrieved directly from the data without resorting to computer fitting. An easily measurable quantity such as the difference between the normalized peak and valley transmittance ($\Delta T_{p-v} = T_p - T_v$) can be used to estimate the nonlinear index (n_2) with considerable accuracy (i.e. ΔT_{p-v} variations within +/- 2%) by using the following expression

$$\Delta T_{p-v} \approx 0.406(1-S)^{0.25}\left|\Delta\Phi_0\right| \tag{2.10}$$

for $\left|\Delta\Phi_0\right| \leq \pi$ after a Z-scan is performed. For small $|\Delta\Phi|$, the peak and the valley occur at the same distance with respect to the focus, and for a cubic nonlinearity, their separation is found to be $\approx 1.7\, z_0$. This distance allows to calculate the order of the nonlinearity. Using samples with high optical quality, phase changes corresponding to less than $\lambda/250$ wavefront distortion can be resolved, revealing the sensitive nature of the Z-scan technique.

2.3.2 Open Aperture Z-scan, nonlinear absorption effects

In materials with large nonlinear refractive responses, there may be considerable contribution from the nonlinear absorption coefficient due to single or multiphoton resonance, saturation of the single-photon absorption, or free carrier dynamic absorption. This in turn can have an appreciable effect on the Z-scan profile. While the close aperture Z-scan is sensitive to both nonlinear refraction and nonlinear absorption, removing the aperture will eliminate the effect of nonlinear refraction, leaving the setup sensitive only to nonlinear absorption. The nonlinear absorption coefficient β related to the Two Photon Absorption phenomenon can be calculated from such an *open* aperture experiment.

Two Photon Absorption (TPA) is a third-order nonlinear optical process, in which two photons are absorbed simultaneously such that the energy of the photons add up to reach the energy of the excited state of the molecule (*Fig 1.3*). TPA has important application in three-dimensional optical data storage[4-5], photolithography, scanning fluorescence microscopy[6], optical power limiting[7-8], etc. These applications exploit the fact that the rate of TPA has a quadratic dependence on the illuminating laser intensity.

If we consider only the effects of TPA, the third-order nonlinear susceptibility can be considered complex, with a real ($\chi_R^{(3)}$) and an imaginary ($\chi_{\mathrm{Im}}^{(3)}$) part as follow:

$$\chi^{(3)} = \chi_R^{(3)} + i\chi_{\mathrm{Im}}^{(3)} \qquad (2.11)$$

where the real part is related to n_2(mks) through

$$\chi_R^{(3)} = 2n_0^2 \varepsilon_0 c n_2 (mks) \qquad (2.12)$$

and the imaginary part is related to the TPA coefficient β through

$$\chi_{\mathrm{Im}}^{(3)} = \frac{n_0^2 \varepsilon_0 c^2}{\omega} \beta \tag{2.13}$$

with

$$\beta = \frac{\Delta T \; 2\sqrt{2}}{I \frac{(1 - e^{-\alpha L})}{\alpha} (1 - r)} \tag{2.14}$$

where r is the Fresnel reflection coefficient.

As illustrated in *Fig 2.8*, the open aperture Z-scan profile is symmetrical with respect to the focus plan ($z=0$) where the transmittance is a minimum (i.e., multiphoton absorption) or a maximum (i.e., absorption saturation). Provided that $\beta I_0 L_{eff} < 1$ and $\beta / 2kn_2$ (mks) are satisfied there is a simple method for separating β and n_2 (mks). The refractive part of $\chi^{(3)}$ can be determined by dividing the closed aperture ($S<1$) normalized Z-scan (with a low irradiance background Z-scan subtraction to reduce sample inhomogeneities) by the open-aperture ($S = 1$) normalized transmittance. This will result in a new Z-scan where ΔT_{p-v} agrees to within ± 10 % of that obtained from a purely refractive Z-scan.

One can ultimately calculate $\chi^{(3)}$ relative to a reference under the same excitation and experimental condition. In this case the following equation, which is the combination of equations (2.5), (2.10) and (2.12) can be used.

$$\frac{\chi_{sample}^{(3)}}{\chi_{reference}^{(3)}} = \left(\frac{n_0^2 \Delta T_{p-v}}{L_{eff}} \right)_{sample} * \left(\frac{L_{eff}}{n_0^2 \Delta T_{p-v}} \right)_{reference} \tag{2.15}$$

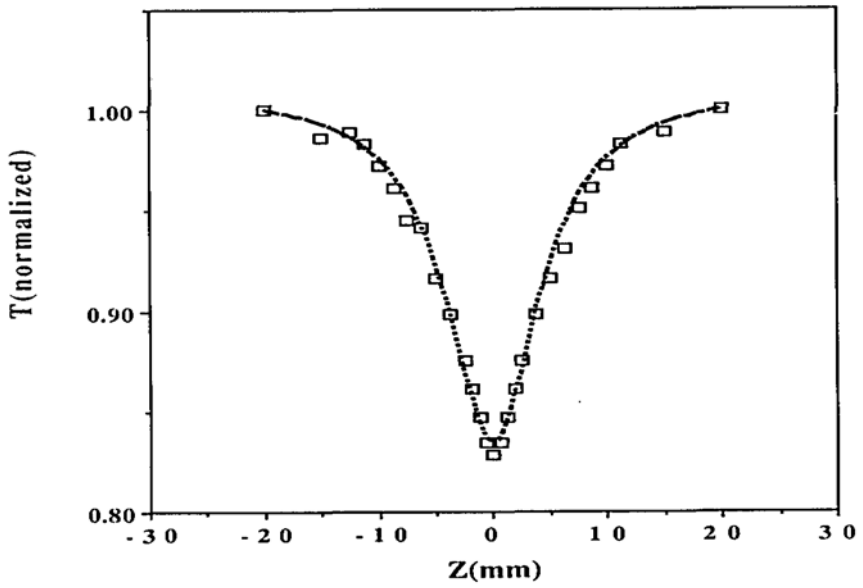

Fig. 2.8 Illustration of a typical open aperture Z-scan profile

2.4. White-light continuum generation and spectroscopy

Although lasers are very good sources of highly coherent monochromatic and intense light pulses, more too often in nonlinear spectroscopy, it is required the use of a wide-band, short-pulse light source in order to monitor the photophysical and photochemical properties (transient absorption spectrum) of a sample at different regions of the visible spectrum. A white-light supercontinuum pulse provides just that: it is broadband (~300 to 1000 nm), has relatively short pulse duration and intense enough to induce exited state absorption from the sample. White-light continuum (WLC) can be generated by focusing a short optical pulse into a material with high third-order nonlinearities. WLC finds its origin in the third-order effect known as self-phase modulation (SPM). SPM is the change in the phase of an optical pulse due to the nonlinearity of the refractive index of the material. Since the intensity $A^2(\tau)$ of the pulse has a Gaussian distribution, various part of the pulse undergoes different phase shifts, leading to a frequency shift that is directly proportional to the distance traveled *z* (*chirp*). *Figure 2.9* shows a $sech^2$ pulse propagating in a material with $n_2 > 0$ and the corresponding phase shift applied due to the intensity variation of the pulse envelop in the material.

The process of SPM is developed here:

Considering an intense short pulse described by the following electric field

$$\vec{E}(z,t) = \vec{A}(z,t)e^{i(k_0 z - \omega_0 t)} + c.c. \qquad (2.16)$$

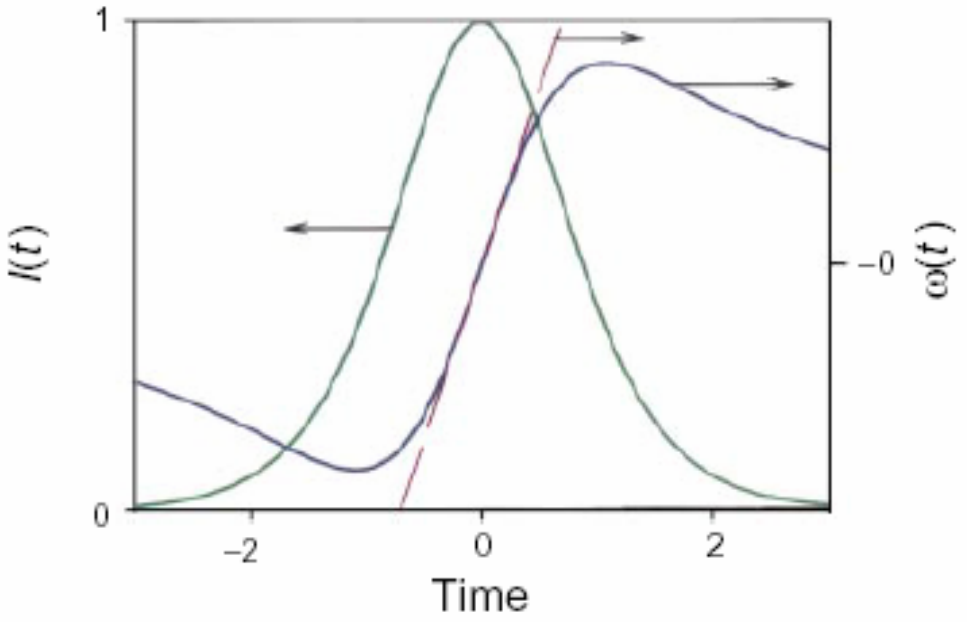

Fig 2.9 Variation in instantaneous frequency due to SPM in a $sech^2$ pulse propagating through a material with $n_2>0$

propagating through a nonlinear medium, the phase of the electric field of the pulse can be written as:

$$\phi(z,t) = \omega_0 t - kz = \omega_0 t - \frac{\omega_0 n(t)}{c} z = \omega_0 t - \frac{[n_0 + n_2 I(t)]\omega_0}{c} z \qquad (2.17)$$

The temporal variation $d\phi/dt$ of the pulse gives the frequency $\omega(t)$:

$$\omega(t) = \frac{d\phi(z,t)}{dt} = \omega_0 - \frac{n_2 z \omega_0}{c} \frac{dI(t)}{dt} \tag{2.18}$$

As it can be seen from equations 2.17 and 2.18, the time-dependent refractive index modulates the instantaneous phase of the pulse, consequently, generating different frequency components. Therefore, both redder and bluer frequencies relative to the input frequency are generated. In *Fig 2.9*, for example, for the $sech^2$ pulse propagating in the nonlinear medium, if the nonlinear refractive index is positive ($n_2>0$), leading edge of the incident pulse $\left(\frac{dI(t)}{dt} > 0\right)$ generates lower frequencies (redder components) and trailing edge of the pulse generates higher frequencies (bluer components). A WLC pulse is therefore the perfect seed for an optical parametric amplifier.

References

1. Claude Rulliere, Femtosecond Laser Pulses : Principles and Experiments, Springer (2005)
2. Rick Trebino, Kenneth W. DeLong, David N. Fittinghoff, John N. Sweetser, Marco A. Krumbugel, Bruce A. Richman, and Daniel J. Kane, "Measuring ultrashort laser pulse in the time-frequency domain using frequency-resolved optical gating," Rev. Sci. Instrum., vol. 68, 3277-3295 (1997)
3. M. Sheik-Bahae, A.A. Said, and E.W. Van Stryland, *High-sensitivity, single-beam n_2 measurements*, Opt. Lett., **14**, 955-957 (1989)
4. J. Michael Hollas, **Modern Spectroscopy**, John Wiley and Sons (2004)
5. Donald L. Wise, Gary E. Wnek, Debra J. Trantolo, *Electrical and Optical Polymer Systems*, (1998)
6. D. Weaire, B. S. Wherrett, D. A. B. Miller, and S. D. Smith, Opt Lett. **4**, 331 (1979)
7. Mansoor Sheik-Bahae, Ali A Said, Tai-Huei Wei, David J. Hagan and E. W. Van Stryland, Sensitive *Measurements of Optical Nonlinearities Using a Single Beam*, IEEE J. of Quantum Electronics **26**, No. 4, 760-769 (1990)
8. D.A. Partenopoulos and P.M.Rentzepis, *3-Dimensional Optical Storage Memory*, Science **245**, 843-845 (1989).
9. J.H. Strickler and W.W.Webb, *Three-dimensional optical data storage in refractive media by two-photon point excitation*, Opt. Lett. **16**, 1780-1782 (1991).

10. W. Denk, J.H.Strickler, and W.W. Webb, *Two-photon laser scanning fluorescence microscopy*, Science **248**, 73-76 (1990).

11. G.S.He, et al. Appl. Phys. Lett. **67**, 2433-2435 (1995).

12. C.W. Spangler, *Recent developments in the design of organic materials for optical power limiting*, J. Mater. Chem. **9**, 2013 (1999)

Chapter 3

Nonlinear optical absorption in laser induced modified regions of fused Silica substrates

3.1 Introduction and motivation

The purity of optical material has been a constant and intense research topic since the early days of the Laser. In the quest for developing high powered laser, it has been established that a laser system is not stronger that its weakest optical element. While the purity of the components is not critical at low power levels, the presence of minute inhomogeneities along with nonlinear absorption processes can lead to catastrophic material failure when submitted to extremely high energies. The situation is no different in telecommunications, where the input power launched into a fiber should ideally be as high as possible to ensure proper signal detection level at the output. However this practice is inhibited by nonlinearities arising in the fiber due to impurities, inclusions and nonlinear susceptibilities. Optical communications thus requires the use of ultra-high purity optical fibers.

Because of its transparency in the visible and infrared regions, high purity silica (SiO_2) glass has been incorporated in numerous applications in modern optoelectronics and photolithographic systems. Its use ranges from being the key material for low-loss optical fibers to its utilization in optical windows in high vacuum confinement chambers. While defects are generally unwelcome but omnipresent guests in glassy materials, inclusions of dopants into oxide glass systems allow the emergence of borate, germinate, phosphate,

telluride and tantalite glasses, each with particularities tailored to address a specific issue. It has been suggested that laser induced structural changes in glasses could be used to achieve 3-dimensional data storage[1]. With this broadening in the range of utilization, the specifications of this material have become more demanding, keeping this material in the forefront of scientific research.

The advent of large aperture optical elements requiring optimum UV transmission has generated more stress into using Fused Silica of ultra-high purity for the manufacturing of optical components. In such large aperture laser system, fused silica optics are required to withstand increasingly higher power densities without sustaining irrevocable damage leading to significant optical losses although small amounts of damage may not hinder performance[2]. Damage initiation under high power pulsed laser irradiation is believed to be the results of excessive absorption by various types of defects embedded in the materials during both manufacturing and exposure to laser radiation, and results in discrete damage sites, or pinpoints, on the surface or the bulk of materials at fluences much below the dielectric breakdown threshold of the pure material[3,4]. The presence of a large damage pinpoint density can give rise to beam losses and intensity modulations, ultimately impeding laser system performance[5]. One key issue in fused silica optics related to its performance in large aperture laser systems is associated with the growth in size of laser induced damage sites under subsequent near UV (355-nm) laser irradiation. This effect, known as “damage growth”, can lead to failure of the material within a short period of time[6].

It has been shown[7] that laser induced damage in optical materials with nanosecond pulses is associated with the formation of dense plasma accompanied by temperatures on the order of 1 eV. These extreme conditions lead to irreversible material modifications including mechanical failure and defect formations. In fused silica, spectroscopic studies of defects located at damage sites under femtosecond and nanosecond pulsed irradiation indicate a similarity in their optical properties suggestive that the dominant defect species are the same, independent of the pulse-width or laser wavelength[8,9]. It has been postulated that these defects are responsible for re-ignition of the damage process at pre-existing damage sites leading to damage growth[6].

Although damage initiation has been the focus of intense investigation since the early days of laser development[2,3], the early stage mechanisms under nanosecond laser irradiation leading to the formation of plasma have still not been resolved. Recent work suggests that defect-assisted multiphoton ionization may be a common mechanism for damage initiation[10]. It is the objective of this work to determine the effects of laser induced damage in the transmission of large aperture optical elements and also to examine if defect assisted multiphoton absorption processes are present at damage sites in fused silica during high power laser irradiation. Such processes can be related to the plasma "re-ignition" and damage growth observed in fused silica. Identification of the process leading to damage growth is important in order to devise methods to mitigate this problem.

3.2 Background investigation

Although one could argue that laser induced damage in bulk materials is the result of a number of miscellaneous effects, in fact, the number of concurring phenomena is rather small. Table 3.1[11] provides a summary of four fundamental damage mechanisms along with the type of materials where they predominantly occur. In this thesis, we will pay special interest to surface defects in fused silica materials. In general, surface defects and

Damage Mechanism	Category of Damage				
	Bulk Active	**Surface**	**Nonlinear Materials**	**Thin Films**	**Infrared Components**
Particulate Inclusions	●		●	●	●
Self-focusing	●		●		
Electron Avalanche	●	●	●	●	
Thermal Effects			●	●	●

Table 3.1. Operative Damage Phenomena from reference [11].

subsequent damages can be the result of two different phenomena. In the first scenario, superficial damage can be the result of extensive energy absorption by micro-inclusions and micro-cracks generated in the lattice of the material during the polishing process. The

second case concerns overwhelming energy absorption from an otherwise normal lattice. In this case, when the absorbed energy is much higher than the binding energy of the Si and O atoms, the breaking of bonds creates energy traps that will act as nanoreactor for the initiation of the damage process. Whichever the origin of the defect, damage formation, subsequent growth and possible mitigation pathways have been extensively documented[12]. Some of the mathematical development following in this background investigation can be found in [12].

Preliminary study[13] has established that the predominant phenomena leading to optical bulk surface damage is intrinsic electron avalanche breakdown. Moreover, such breakdown is further facilitated by the mere presence of microscopic cracks, pores and absorbing inclusions at the surface, which dramatically decreases the performance of the transparent dielectric material. Electron avalanche in optical components finds its roots in the high intensity level of a focused laser radiation. When the material is irradiated with an intense energetic optical light, the powerful radiation initiates breakdown. Assuming that some level of impurities (with free electrons) exists in the material, due probably to metallic inclusions, easily ionized impurities or background scattering, under the influence of the applied optical field, these electrons are accelerated to high enough energy to cause impact ionization within the medium. The physics of damage is evident for the case of ultra-short laser pulses. If the laser pulse duration is shorter than the electron-phonon scattering time of about 10 ps, energy transfer between heated electrons and the lattice are restrained or non-existent during the laser pulse. This creates a state of accumulative thermal behavior. The temperature of the affected region rises, along with

the pressure. Oscillating in an intense laser field, the electrons collide with atoms and are heated. When the electron energy exceeds the bandgap a new electron is produced by impact ionization and an electron avalanche is initiated. For short pulses, the only factor limiting development of the avalanche is the pulse duration. If the pulse duration is well above 10ps, the energy gained by electrons through collisions with atoms is well balanced by the energy transfer from electrons to the lattice. In this case, avalanche can only be achieved when energy gain overcomes the losses giving the criteria for avalanche existence[14]:

$$\sigma E^2 > \gamma U_{ph} \tag{3-1}$$

where E is the laser electric field, U_{ph} is the typical phonon energy, σ and γ are respectively the electrical conductivity and the rate of energy transfer for electron energy near the bottom of the conduction band. If the rate of electron production from ionization exceeds the electron loss, by diffusion out of the volume, by trapping, or recombination, the avalanche ensues, leading to a strongly absorbing plasma. Material damage usually occurs in the vicinity of the plasma. In general, the surface damage, identified by postmortem examination of the surface, is always accompanied by the formation of a luminous plasma. Below the threshold for surface damage, dielectric surfaces are observed to emit electrons under intense illumination. This photocurrent increases with increased light intensity, and the damage threshold can be correlated with a critical photocurrent density at the surface[11]. Assuming the Drude formula for the conductivity

for 355nm light, the lower limit for critical intensity I_d to establish avalanche can be estimated to be I_d = 150GW/cm^2 in fused silica.

The creation of a damage site is usually followed by a transverse growth of the modified region that varies exponentially with the number of impinging optical pulses. When temperature levels around the affected area reaches a critical value, a thermal explosion ensures. Thermal explosion refers to the rapid expansion of the heated region into the glass, which is then ionized. Plasma produced by the initially absorbed light radiates UV which is absorbed in the matrix resulting in more heating and in an increase of the absorption coefficient of the glass. If most of the energy is assumed to be spent ionizing the material and only a fraction is spent heating the material, then the rate of growth of the luminous plasma ball can be estimated from energy balance[12]:

$$n_e I_0 4\pi a^2 \frac{da}{dt} = \sigma I(t) \tag{3.2}$$

where n_e is the electron density, $I_{0\,\mathrm{is}}$ the ionization potential and σ is still the electrical conductivity. It can be found after some mathematical manipulations that the plasma ball grows exponentially *a = a(0) exp (G),* where *G* the growth factor is given by[12]

$$G = 10\frac{F\omega}{nI_0 c}\,\mathrm{Im}\frac{1}{\varepsilon + 2} \tag{3.3}$$

here ε is the dielectric coefficient of the plasma evaluated through the Drude model. As can be seen in equation 3.3, the growth factor is independent of the pulse duration and is determined by the fluence only.

Another important factor in the creation of surface damage in bulk materials is related to the importance of reflections at interfaces. It has been established[15] that a transparent dielectric material exposed to a collimated beam of light will damage at the exit surface at a lower power level than at the input surface. This oddity is a result of Fresnel reflection and will be explained in the following. At normal incidence to a dielectric surface, part of the incident light is reflected and part transmitted as determined by the Fresnel relations. At an entrance surface, the reflected wave is 180° out of phase with the incident light, and the transmitted light intensity is related to the incident intensity by[15]

$$I_{ent} = [4/(n+1)^2]I_0 \qquad (3.4)$$

where n is the linear refractive index of the medium and I_0 is the incident intensity. If $n = 1$ (*air*), then $I_o = I_{ent}$. Since in general $n > 1$ (*glass*), then I_{ent} is less than I_o. At the exit surface, the reflected wave suffers no phase shift, so that the intensity at the exit surface is related to the intensity incident at the entrance surface by[15]

$$I_{exit} = [4n/(n+1)^2]^2 I_0 \qquad (3.5)$$

Thus the ratio of the intensity inside the medium at the exit surface (I_{ext}) to the intensity inside the medium at the entrance surface (I_{ent}) is

$$\frac{I_{exit}}{I_{ent}} = (2n/n+1)^2 \qquad (3.6)$$

Thus the intensity at the exit surface of the material will be much higher than that at the entrance surface. Therefore the exit surface will be more prone to damage. Since in this investigation we are specially concerned with surface damages originated in fused silica substrates, special care was taken to generate the damage regions on or around the entrance surface of the studied samples.

In the previous analysis, we have presented a brief summary of different mechanisms responsible for surface damage creation and growth. However, in this thesis, our principal investigation will focus on the absorption processes taking place inside the damaged area. In particular, we will determine the influence of laser induced optical breakdown on the performance of fused silica-based optical elements and study their absorption behavior in order to determine whether or not multiphoton absorption processes are present in such damage regions.

3.3 Experimental Technique

The experimental setup shown in the schematic diagram in *Figure 3.1* was used to measure the intensity–dependent transmission in fused silica substrates. A single Gaussian beam obtained by a mode-locked Nd:YAG laser is tightly focused into the sample using a 10 cm focal length lens. This produces a $1/e^2$ beam radius ω_o, of approximately 50-μm at the focus. The laser spot size was obtained by measuring the laser energy as a function of the position of a metal blade, scanned across the laser beam. The laser produces 25-psec pulses at 1.06 μm with energies per pulse ranging from few μJ to 30-mJ. Using second and third harmonic generation crystals, optical pulses at 532nm and 355nm are generated with a 20 Hz repetition rate. The incident optical pulse energies were constantly monitored by reflecting about 8% of each pulse into the probe of an energy-meter before entering the fused silica substrate. The intensity of the incident beam is adjusted by an attenuation setup consisting of a half wave plate and two crossed polarized Glan-Thompson polarizers. Using a second energy meter, the light transmitted through the medium was measured as a function of the intensity of the incident beam.

The samples used in our experiments were 1-cm thick, polished amorphous silicon dioxide substrates (*Corning 7940, manufactured by flame hydrolysis*). Damage spots were generated on and near the surface of the substrates using the third harmonic of a 3-ns Q-switched ND:YAG laser as described in reference[6]. The damage sites were initiated using a fluence of 24±4 J/cm^2. These sites were subsequently exposed to ten additional pulses at 10 J/cm^2 to increase their size through the re-ignition of the damage process.

The modified material, that is the focus of this investigation, was generated during the laser induced damage process in the crater of the damage site. The visible damaged areas were about 1-mm in diameter.

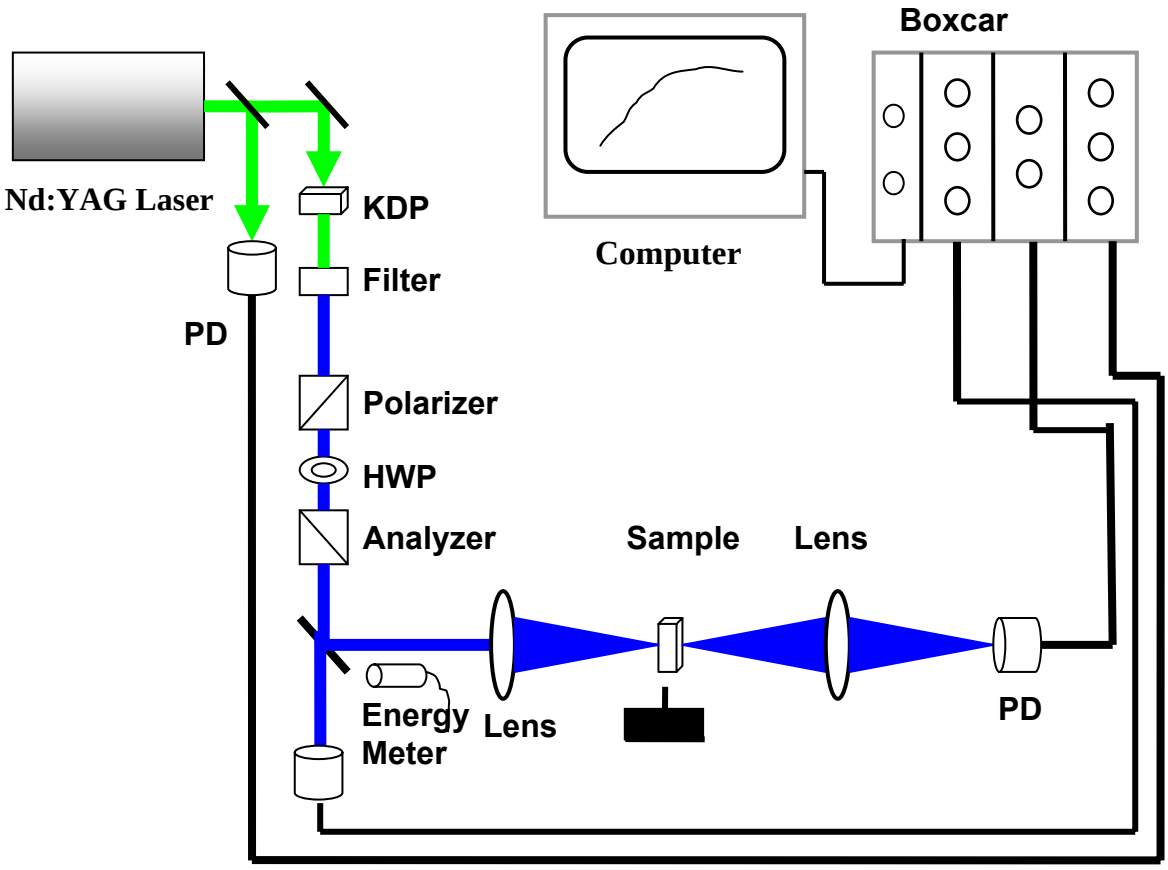

Figure 3.1. Experimental setup for the transmission measurements.

3.4 Results

The experiments involved measurement of the intensity-dependent transmission in damaged and pristine regions of fused silica substrates. It is very important that the input/output detection devices have linear responses in optical transmission measurements. Therefore, before the actual experiment, both the energy meter used to monitor the input energy and the photodetectors used to measure the transmitted signal have been checked for linearity. This is done by using the same experimental set-up but with a fully transparent sample in the beam path. The input intensity is varied while recording the response of either the energy meter or the photodetectors. *Figure 3.2a* and *3.2b* illustrates the linear response of the system at 355nm which was also verified at the remaining two investigating wavelengths.

Figure 3.3 a) shows the experimental data for one of the fused silica samples where the normalized transmitted signal is plotted as a function of the incident pulse energy. The irradiance at all the wavelengths was varied in the range of 3-70 GW/cm^2. Due to the presence of scattering at damage sites and the non-uniformity of the scattering properties at (or within) each damage site, a different fraction of the incident light is transmitted through each point studied. To compensate for the variation in scattering, the data shown in all figures are normalized to the value of the transmitted signal for incident pulse energy of 550-μJ. The measurements shown in *figure 3.3* were taken at one spot in a damaged site and represent a typical representation of our experimental observations**.** The maximum energy per pulse used in this experiment was the upper limit for which the

a)

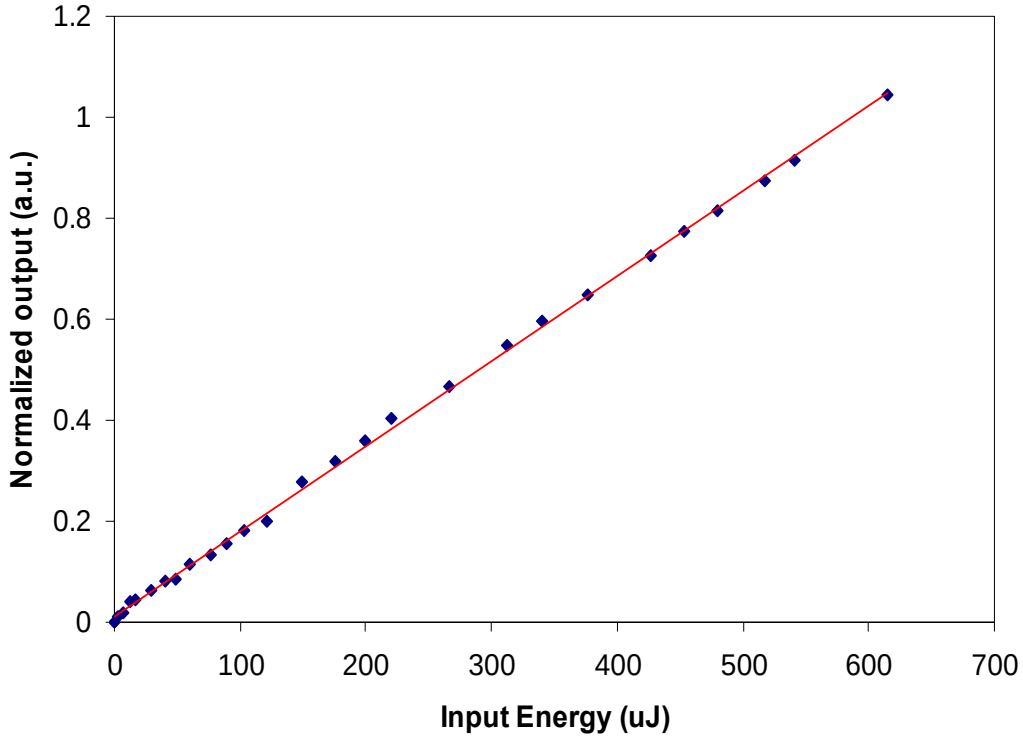

b)

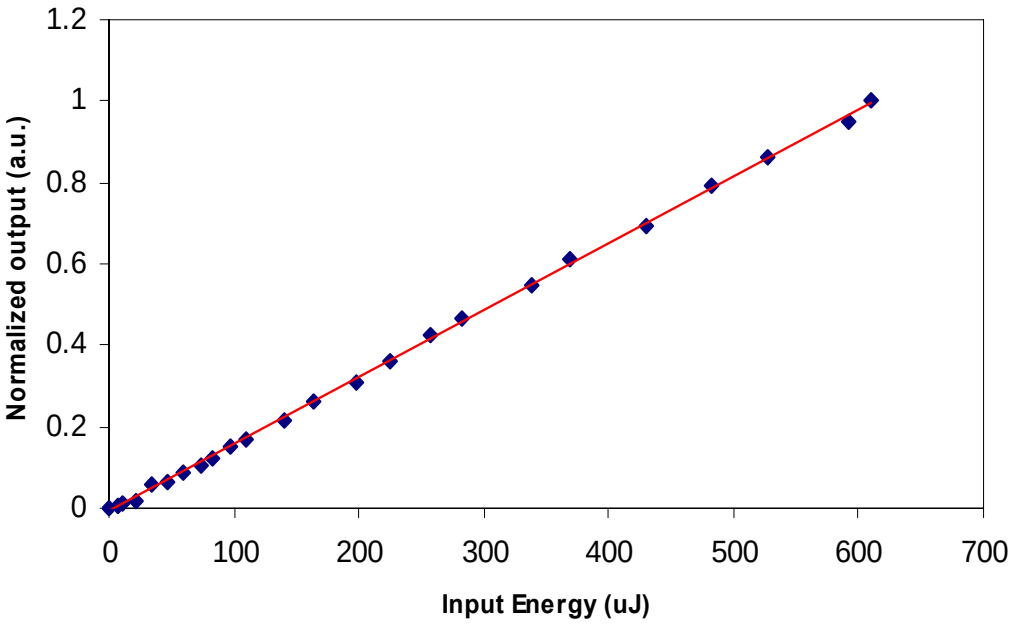

Figure 3.2. Linearity of the detection system at 355nm **a)** Input Energy meter **b)** Output photodiode

experimental data taken at lower energies could be consistently reproduced when the laser pulse energy was lowered after measurements at high power. More specifically, pulses with energy higher than ≈ 600-μJ at 355 nm resulted in alteration of the scattering signal when compared with prior measurements at the same or lower irradiation level. This suggested the initiation of structural changes and damage growth within the damage site as a result of exposure to pulse energies higher than ≈ 600-μJ. Hence, the maximum pulse energy used in this experiment is just below the onset of damage growth under 355nm irradiation using our laser system.

It is clear, as can be seen in *figure 3.3 a),* that the intensity of 355-nm pulses transmitted through a damage spot as a function of the incident intensity demonstrates a nonlinear behavior (solid diamonds). On the other hand, using the same laser intensities but laser pulses at 532-nm (open triangles) and 1064-nm (solid squares), we found that the response is linear. The nonlinearity of the response at 355nm can be further appreciated in *figure 3.3 b)* where the logarithmic plot of the absolute transmission of the sample shows a rapid decrease in the transmission at higher incident power. At 1064 and 532nm, the transmission at the damage spot shows a predominantly horizontal behavior indicating a linear relationship between input power and output energy. When the same measurement is performed in pristine regions of the sample we found that the transmission was essentially linear at all three wavelengths used in our experiments (532nm, 1064nm and 355nm). These results strongly suggest the presence of a nonlinear absorption process at 355 nm, possibly two-photon absorption (TPA), in the modified region of the fused silica substrate.

a)

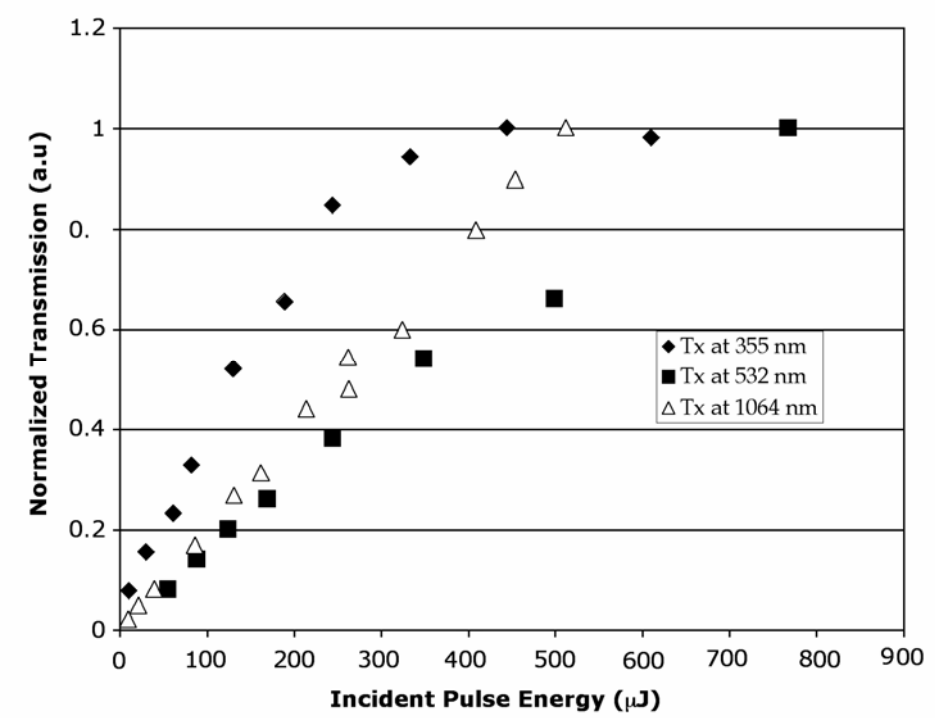

b)

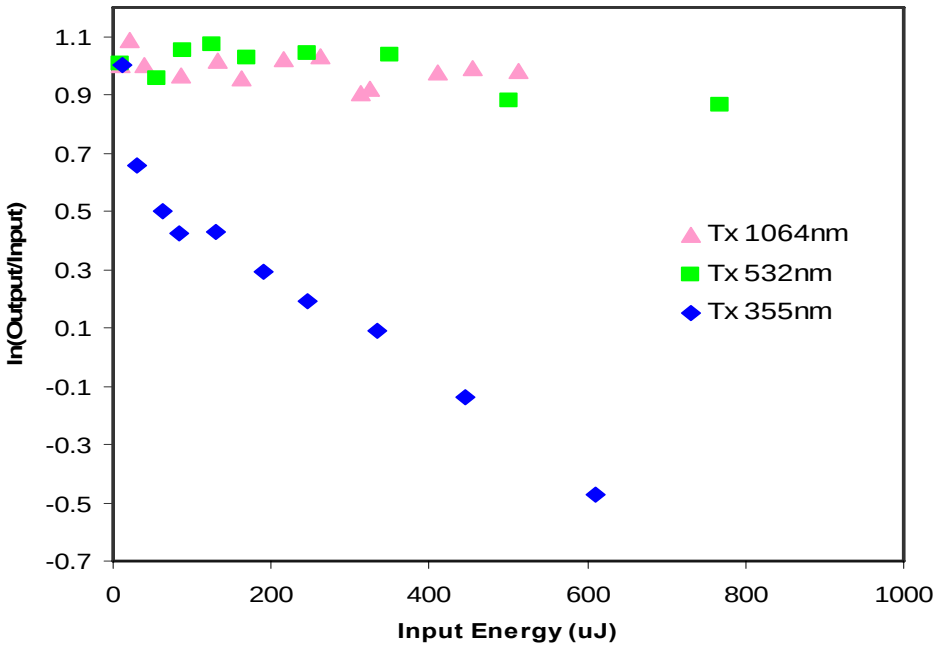

Figure 3.3 a) Relative transmission b) absolute transmission of high-energy optical pulses at 355nm, 532nm and 1064nm through the damaged region of a fused silica substrate as a function of the incident energy. The plots are normalized to unity for comparison purpose.

Fig. 3.4 shows the transmission dependence on the incident intensity at 355-nm for a pristine region (open circles) and a modified spot (solid squares). The solid line in figure 4 shows a fit to the transmission curve of 355-nm pulses through a damage spot. The fit assumes an intensity dependent loss coefficient $\ln(I_{tr} / I_{in}) = -C-I_{in}\beta\delta$, where C is the constant linear loss term, β is the TPA coefficient, δ is the interaction length in cm and I_{tr} and I_{in} are the incident and transmitted intensities (in W/cm^2). A transmission

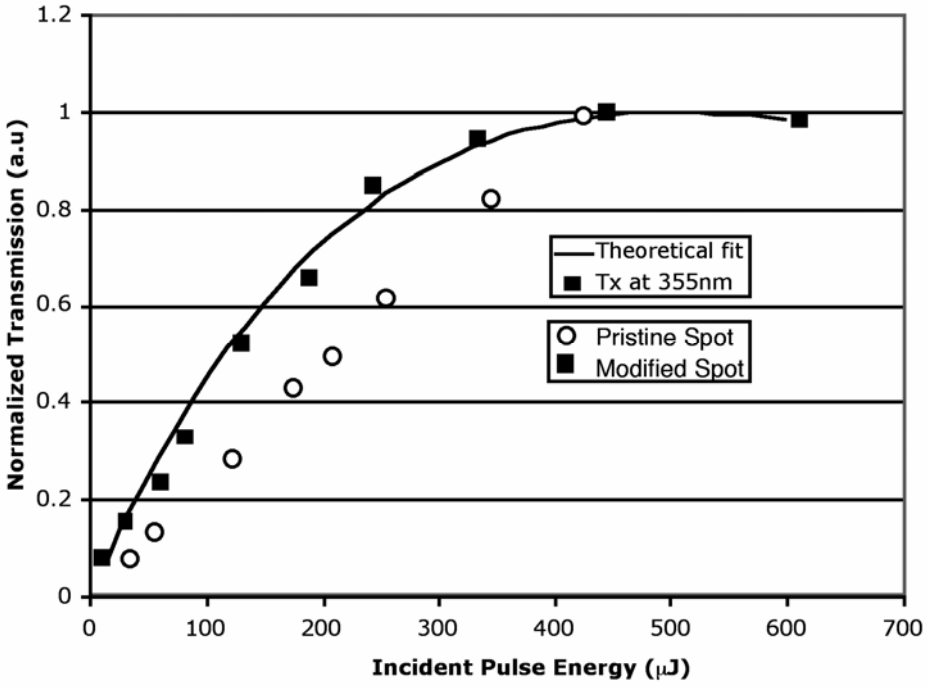

Figure 3.4 The transmission of high-energy optical pulses at 355nm through the damaged region of a fused silica substrate as a function of the incident energy. The solid line in Fig. 3 shows a theoretical fit to the transmission curve at a damaged spot.

measurement at very low intensity is used as the linear loss term C. Good agreement with the experimental data is obtained for $\beta\delta = 1.5 * 10^{-11}$ cmW^{-1}. This seems to confirm the TPA hypothesis. Based on the reported value of the TPA coefficient of fused silica at 355-nm[16], the linear response observed in our experiments in the pristine polished region at all wavelengths is not surprising since the range of irradiance used (I_o = 0 to 70 GW/cm^2) is too low to alter the linearity of the response.

The experimental results clearly suggest that the TPA losses occur mainly at the damage spots. Earlier reports[6,7,9,17] have suggested that the high temperature plasma created during the formation of the damage spot modifies the surrounding silica to produce a thin layer of defects. SEM examinations show that the damage sites consist primarily of a molten core, surrounded by a region of fractured material. X-ray tomography has allowed identifying a compaction layer that is approximately 10 microns thick with a density that is approximately 20% higher at the bottom of the damage crater[18]. The above experimental results suggest that the modified layer of fused silica is responsible for the observed TPA. As we mentioned previously, defect assisted ionization via multiphoton absorption can lead, in the presence of a high irradiance laser pulse, to cascade electron multiplication and the creation of dense plasma which results in additional absorption of laser light and energy deposition on the material. The relationship between the re-formation of plasma at damage sites under subsequent laser irradiation with damage growth has been documented elsewhere[6]. In our experiments we have observed that following the onset of the nonlinear behavior at about 400-μJ (at 355 nm), damage growth is observed at about 600-μJ suggesting a direct relationship between these

processes. The observation of nonlinear absorption followed by plasma formation should be present at longer wavelengths (532 nm) but at higher pulse energies. The laser energies available using our laser system did not allow the observation of these anticipated effects.

A variety of techniques, including fluorescence microscopy, optical coherence tomography, photoluminescence and cathodoluminescence spectra have been used to resolve and characterize the different defects generated optically in fused silica. Those point defects, generated by the breaking of Silicon and Oxygen bonds due to the high-intensity optical pulses, are usually associated with interstitial O_2 molecules, E' centers (paramagnetic positively charged oxygen vacancies, ≡Si•Si≡, or neutral dangling Si bonds, ≡Si•), non-bridging oxygen hole centers (NBOHC; dangling oxygen bonds, ≡Si–O•), peroxy radicals (PORs; ≡Si–O–O•) and oxygen deficient centers (ODC), which can occur as neutral oxygen vacancies, ≡Si–Si≡, or as two-fold coordinated Si atoms, ≡Si–O–Si–O–Si≡ [19]. Comparison of the photoluminescence emission spectra of typical defects in silica and the defects that we studied revealed perfect overlap at 1.9 eV and at 2.27 eV corresponding to NBOHC and ODC respectively.

An important step in the study of damage precursors in large aperture optical element is the determination of damage mitigation processes allowing to extend the life cycle of such optical components. The process of laser-induced optical defect formation and subsequent correction is illustrated in *Figure 3.5*[20]. Among the treatments available to ensure damage mitigation, optical annealing through intense laser radiation seems to offer

the best alternative. It has been reported that annealing fused silica reduces the photoluminescence associated with optically produced damage sites[8,21]. This effect suggests the passivation of defects responsible for the observed photoluminescence. The annealing process can be defined as the correction of an optical defect (*micro-cracks, inclusions, broken bonds*) through the creation of an intense local heating. Local heating increases the surface temperature and evaporates the material. Following evaporation, the

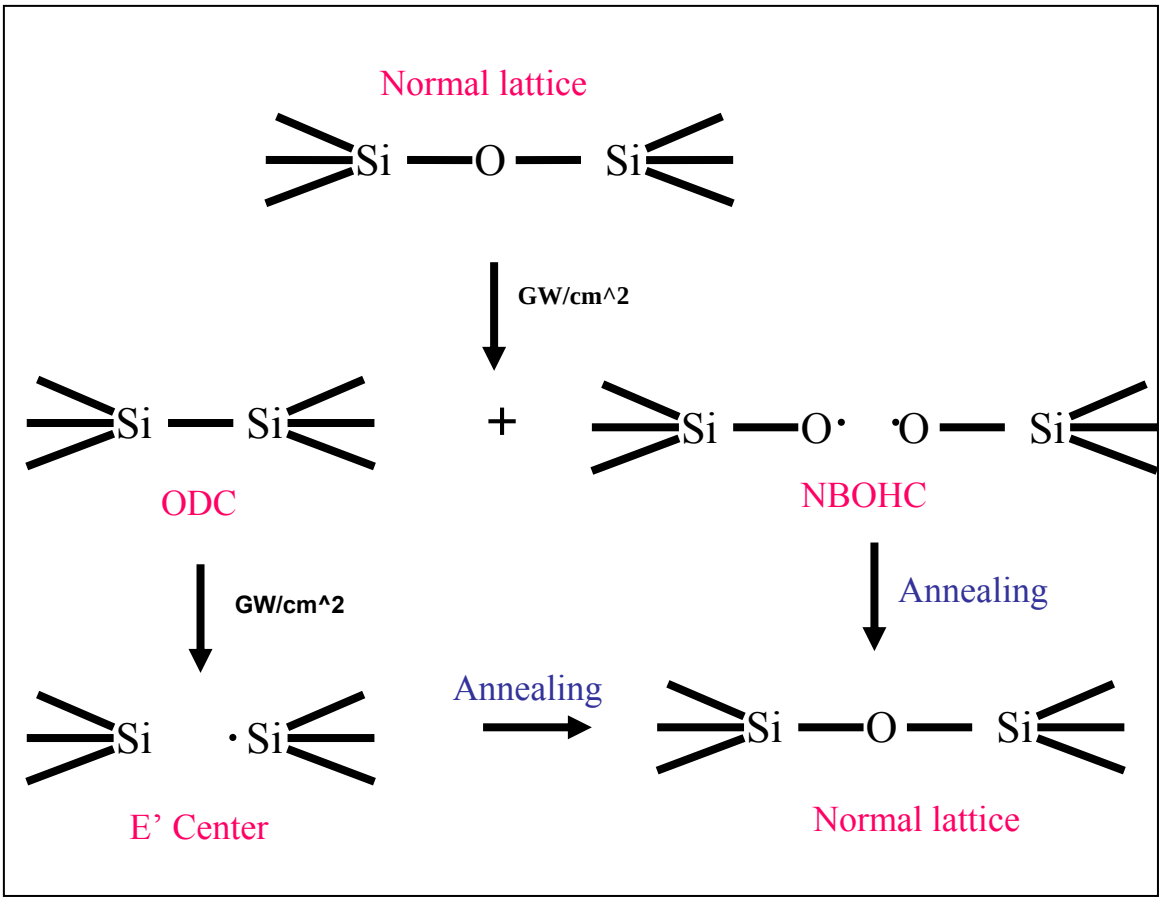

Figure 3.5 [20] Mechanism of defect formation and subsequent annealing in Silica

material is revitrified, the viscosity of fused silica is reduced, rearrangement occurs, surface tension closes the cracks, thus healing the defective region. In most cases, the treatment replaces the damage spot with a smooth Gaussian shaped pit and an increase in the laser damage threshold can be observed[22].

If this procedure is applied to our damage sites and if the same defects are responsible for TPA, annealing should lead to reduction or removal of the nonlinear response for the laser intensities used in this experiment. We tested this possibility by annealing damage sites using long exposures to laser irradiation. *Figure 3.6* shows the transmission response of the fused silica substrates at a damaged spot for freshly modified spot and for an "old" modified spot, which has been subjected to hours of repeated exposure to the 355-nm, 20-Hz, 600-μJ focused beam. For comparison a curve for a pristine region is also shown. As in the previous figures, the data shown are normalized to the value of the transmitted signal for the incident pulse energy of 550-μJ. The transmission dependence of the overexposed ("old") spot is clearly linear and indistinguishable from the polished pristine spot response. These results suggest that repeated exposure to the 25-ps, UV radiation at 355nm has subjected the sample to a process equivalent to etching or/and thermal annealing, although a visual inspection did not reveal any obvious modifications to the damage spot. Based on these results we can make the assumption that most of the nonlinear absorption occurs within a very thin layer and that the interaction length is not longer than the depth of the compaction layer or about $\delta \sim 10\mu m$ [18]. This yields TPA values for the damage sites as high as $\beta \sim 1.5 * 10^{-6}\ cmW^{-1}$.

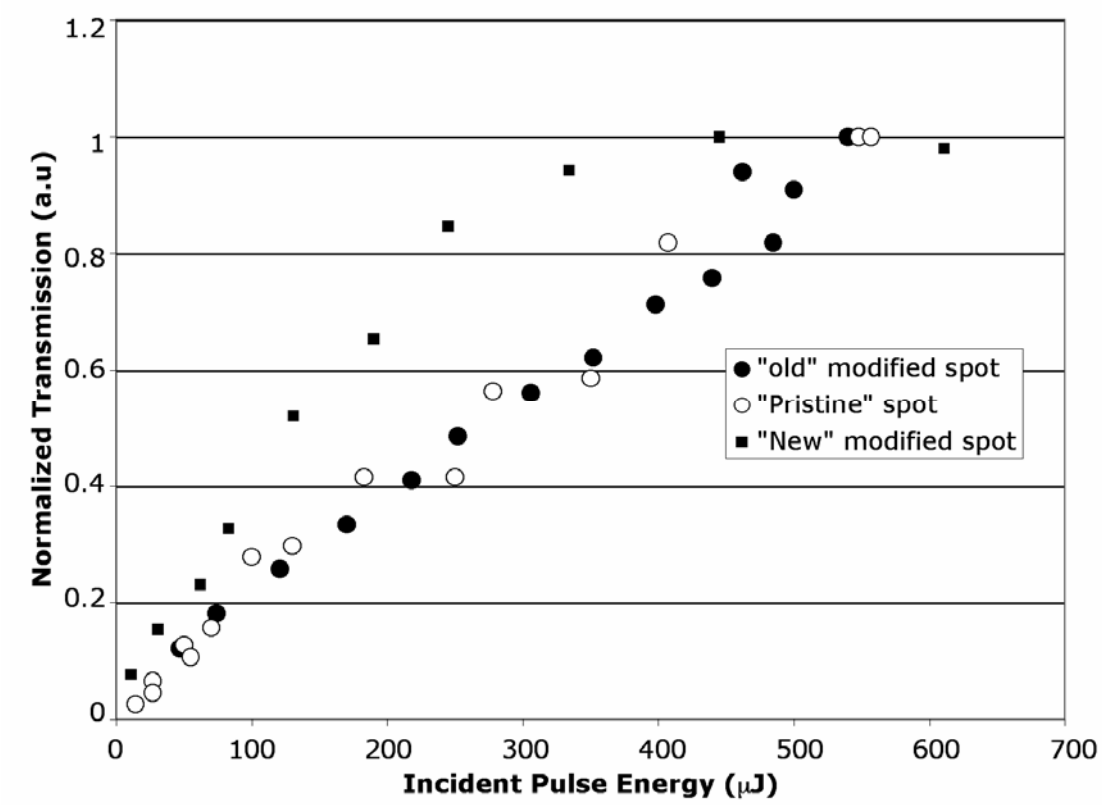

Figure 3.6. The transmission response of the fused silica substrates at a damaged spot for freshly modified "new" sample and for an "old" sample. For comparison, a curve for a pristine region is also shown.

3.5 Conclusion

In conclusion, we have shown that damage sites in fused silica show nonlinear absorption properties at 355-nm arising from the presence of a layer of modified material. TPA effects may lead to additional absorption in existing small surface damage pits which in turn may lead to damage growth and optical component failure. This work does not allow for identification of which defect species known to be present at damage sites is responsible for TPA. Such information may be obtained by repeating these measurements using a tunable laser source and comparing the threshold for the observation of TPA to the absorption spectrum of the different defect species.

References

1. Jianrong Qiu, K. Miura, K. Hirao, "Three dimensional optical memory using glasses as a recording medium through a multi-photon absorption process," Jpn. J. Appl. Phys., 37, 2263 (1998)
2. M. Runkel, A. K. Burnham, D. Milam, W. Sell, M. Feit, and A. Rubenchik, "The results of pulse-scaling experiments on rapid-growth DKDP triplers using the Optical Sciences Laser at 351 nm" Proc. SPIE 4347, 359 (2001).
3. N. Bloembergen, "Laser induced electric breakdown in solids" IEEE J. Quantum Electron., 10, 375 (1974).
4. X. A. Shen, S. C. Jones, and P. Braunlich, "Intrinsic optical damage in KBr at 532 nm", Phys. Rev. Lett. 62, 2711 (1989).
5. A. K. Burnham, M. Runkel, M. D. Feit, A.M. Rubenchik, R. L. Floyd, T. A. Land, W. J. Siekhaus, and R. A. Hawley-Fedder, "Laser-Induced Damage in Deuterated Potassium Dihydrogen Phosphate" Applied Optics, 42, 5483, 2003.
6. Stavros G. Demos, Mike Staggs, Mark Kozlowski, "Investigation of processes leading to damage growth in optical materials for large-aperture lasers," Applied Optics 41, 3628 (2002)
7. C.W. Carr, H. B. Radousky, A. M. Rubenchik, M.D. Feit, S. G. Demos, "Localized dynamics during laser-induced damage in optical materials", Phys. Rev. Lett., In Press. (2004)
8. S. Juodkazis, M. Wantanabe, H. Sun, S. Matsuo, J. Nishii, H. Misawa, M. Miwa, " Optically induced defects in vitreous silica," Optics Letters 21, 1729 (1996)
9. S. O. Kucheyev, S. G. Demos, "Optical defect s produced in fused silica during laser-

induced breakdown", Applied Physics Letters, **82**, 3230, 2003

10. C.W. Carr, H.B. Radousky, S.G. Demos, "Wavelength Dependence of Laser Induced Damage: Determining the Damage Initiation Mechanisms", Physical Review Letters, 91, 127402, 2003
11. Alexander J. Glass and Arthur H. Guenther, *Laser induced damage of optical elements: a status report*, *Appl. Optics*, **12**, No 4, 637 (1973)
12. Compilation of status reports available from the Lawrence Livermore National Laboratory (LLNL) library
13. L.W. Hrubesh, R.M. Brusasco, W. Grundler, M.A. Norton, E.E. Donohue, W.A. Molander, S.L. Thompson, S.R. Strodtbeck, P.K. Whitman, M.D. Shirk, P.J. Wegner, M.C. Nostrand, A.K. Burnham. "Methods for mitigating growth of laser-initiated surface damage on DKDP optics at 351 nm", Proc. SPIE vol.**4932**, 180, 2003.
14. B. C. Stuart, M. D. Feit, S. Herman, A. M. Rubenchik, B. W. Shore, and M. D. Perry, "Nanosecond-to-femtosecond laser-induced breakdown in dielectrics", ***Phys. Rev.* B** 53, 1749 (1996).
15. N. L. Boling, M. D. Crisp, and G. Dubé, *Laser induce surface damage*, *Appl. Optics*, **12**, No 4, pp650, (1973)
16. R. DeSalvo, Ali A. Said, David J. Hagan, Eric W. Van Stryland, Mansoor Sheik-Bahae, "Infrared to ultraviolet measurements of two photon-absorption and n_2 in wide band solid," IEEE J. of Quantum Electronics **32**, 1324 (1996)

17. Stavros G. Demos, Mike Staggs, " Application of fluorescence microscopy for noninvasive detection of surface contamination and precursors to laser-induced damage." Applied Optics **41**, 1977 (2002)

18. J. Wong, D. Haupt, J. H. Kinney, M. Stevens-Kalceff, A. Stesmans, J. Ferreira, E. Lindsey, I. Hutcheon, " Morphology microstructure and defects in fused silica induced by high 3w (355nm) laser pulses," LLNL report UCRL-ID-142167, January 2001; A summary can be found at Proceedings of SPIE 4347, 466 (2001)

19. L. Skuja, J. Non-Cryst. Solids **179**, 51 (1994) Skuja L, Guttler B, Schiel D and Silin A R 1998 *Phys. Rev.* B **58** 14296

20. Jeff Latkowski, Joel Speth, and Steve Payne, *Laser Inertial Fusion meeting*, LLNL contract No. W-7405-Eng-48, (2001)

21. M. Wantanabe, S. Juodkazis, H. Sun, S. Matsuo, H. Misawa, M. Miwa, R. Kaneko, "Transmission and photoluminescence images of three-dimensional memory in vitreous silica," Appl. Phys. Lett. **74**, 3957 (1999)

22. Temple, P.A.; Lowdermilk, W.H.; Milam, D.; "Carbon dioxide laser polishing of fused silica surfaces for increased laser-damage resistance at 1064 nm", *Appl. Opt.* 21, 3249-55 (1982).

Chapter 4

Two-photon Absorption Spectroscopy and Imaging of glasses and crystals

4.1. Introduction and motivation

Nonlinear optical crystals of potassium dihydrogen phosphate, KH_2PO_4 (KDP), and its analogs have been incorporated in numerous laser systems as electrooptical elements (optical modulators, Q-switches, and deflectors) for modern short-wave laser technology and nonlinear and integrated optics; as frequency converters of high-power ultrafast laser radiation (generators of sum and difference frequencies and of the second to fifth harmonics of Nd:YAG and Ti:Al_2O_3 lasers); as optical parametric oscillators for the IR region, and also as integrated optical waveguides[1]. The importance of KDP crystals stems from their high efficiency of nonlinear conversion coupled to a substantially high resistance to laser induce damage (LID) along with a wide transparency band. For example, the 50% transparency band of a 2 mm thick sample extends from 176 to 1550 nm[2, 3]. Other key characteristics include a relatively easy and straight-forward preparation process along with reproducible growth to large size and easy finishing. But the use of large plates of such nonlinear crystals in very high power laser systems such as National Ignition Facility (NIF) in the US or the Laser Megajoule Project (LMJ) in France, has revealed a major drawback in the fabrication process of KDP: a relatively slow growth rate. Since typical crystal size used in those projects range from 50 to 100 cm per side, at a growth rate of 0.5-1 mm a day per side, one to two years growth cycles would be necessary to produce one crystal. Successful attempt had been made to accelerate the growth process, but while growth rates of 20-40 mm a day have been achieved, it has

been shown[4] that in such fast grown crystals the purity of the material is greatly reduced due to an increase in optical defect densities. The very use of KDP in harmonic generation, in UV lithography or as large aperture element in high-powered system for laser fusion requires the crystals to be defect-free. The crystals must exhibit a high degree of optical homogeneity, low anomalous birefringence, low absorption, uniform phase matching and high laser damage threshold at the 1^{st}, 2^{nd} and 3^{rd} harmonics of Nd:YAG in order to meet the NIF goals for conversion efficiency, energy on target and beam focusability. Just as fused silica, localized defects inherent to the growth process in KDP crystals can act as *energy traps* leading to localized absorption, heating and subsequent damage of the crystal translating into a decrease in energy conversion efficiency. Besides growth-based defects, other micrometer to nanometer-size energy traps have been identified in such crystals. They have been related to scratches, steps, filaments, polishing or cleaning residues and, more generally, impurities, contaminants or bulk inhomogeneities resulting from the fabrication and finishing processes. The very same variation in origin of these optical scatterers will obviously give rise to different optical behavior from the material, where absorption, scattering, reflection, local heating and bond ruptures are common. It is therefore of considerable importance to develop imaging techniques allowing to resolve the different absorbing centers or optical scatterers and offer an insight in ways to cure the sample from such imperfections.

There have been many attempts at identifying defects in optical glasses and crystals. Particularly, the use of imaging in the study of defects in dielectric materials has been of great interest and has led to the creation of a number of techniques such as microscopic

fluorescence imaging[5], light scattering[6], electron paramagnetic resonance[7], field scanning optical microscopy[8], total internal reflection microscopy[9,10], etc. These techniques, for the most part yield different information about the material under investigation. This information can either be a visual representation of the positions of defects in the crystal as in the case of the AFM or a local deflection or scattering of light showing the position of a probable defect site. However, in general, these techniques although sensitive to structural inhomogeneities, refractive-index and surface profile variations do not offer any insight into the linear or the nonlinear absorption coefficient of the material under investigation.

The procedure we will outlay in this thesis presents two advantages. First, it will bridge the gap between defect characterization and the nonlinear optical properties of the studied sample, second, a two-dimensional mapping of the entire crystal can be readily obtained. This will be achieved by conducting two photon absorption measurements in various KDP crystals. In the first part of the experiment, we correlated the variation in the linear absorption of the materials to their local two-photon absorption (TPA) coefficient. This variation is shown to be related to both the growth direction (*sector*) of the samples and their impurities (*doping*) concentration. In a second experiment, we performed a series of open aperture Zscan measurements in order to optically image the samples. The resolution of the system was such that we could resolve both optically induced defects intentionally generated at the surface of the samples and intrinsic defects inherent to the growth process. The optically generated artificial defects had an average size of 0.5 to 1 mm while the intrinsic defects ranged between 50 and 200μm. The results of this

investigation have shown that not only is two photon absorption (TPA) at 355nm always present in KDP crystals, as has been determined by other groups[11], but also that it is strongly dependent on the local crystal composition. By correlating the two-photon absorption coefficient at 532nm with the distribution of the impurities in the crystal, a TPA-based two-dimensional image of a crystal can be obtained. Here we wish to continue our previous work[12] on these materials by demonstrating the feasibility of using nonlinear absorption as a means of imaging nonlinear crystals.

4.2. Defects in KDP

KDP is a non-centrosymmetrical crystal belonging to the orthorhombic crystal system, with point symmetry group *mm*. Its lattice consists of two phosphate groups distinguished by orientation, and the lattice cell is made of a four formula units[13]. Each group is an almost regular tetrahedron PO_4 and is surrounded by four groups of the other type. Potassium ions are located between the tetrahedrons, each ion being surrounded by eight oxygen ions related to PO4 tetrahedrons. The binding between PO_4 groups is assured by 0.24nm long covalent bonding, which binds two oxygen atoms of neighboring tetrahedrons PO_4.

KDP is an optically negative uniaxial crystal; i.e., the index of refraction for the ordinary polarized (fundamental) beam, n^o, is greater than that for an extraordinary polarized (second-harmonic) beam, n^e. It has a relatively low and constant birefringence for

wavelengths greater than 300nm, with $\Delta n = n^e - n^o = 0.04$. Although mostly transparent all across the visible spectrum, repeated investigation of the linear absorption characterization of KDP reveals the apparition of two defect-related absorption bands. The first unwanted optical absorption band has a peak near 270 nm. It is always accompanied by an additional peak near 210–215 nm. Dieguez et al.[14] and Pritula and Velikhov[15] observed that the 270-nm band, and its related band at shorter wavelength, was significantly enhanced when a KDP crystal was doped during growth with Fe. It has thus become common practice to associate the 270 nm absorption peak with the presence of transition metal ions like Fe3+ and the creation of insoluble metal phosphates. These broad bands are usually taken as a measure of the purity of the crystal since they are present in most KDP crystals.

Although we have investigated the effects of impurity ions inclusions on the optical characteristics of KDP crystals, doping however is not the main source of defects in the lattice of the crystal. Undesired inclusions can have a number of effects on the growth or the overall performance of the host material. Just like for fused silica, various types of defect states can co-exist in a KDP crystal. These include both hole-like and electron-like centers.

Studies have shown that most optical imperfections are related to one of four features of the growing crystal: 1) dislocation bundles generated during either seed regeneration or later incorporation of inclusions, 2) differences in impurity incorporation across boundaries separating the (100) and (101) crystal sectors (*sectorality*), 3) differences in

impurity incorporation across boundaries separating the three vicinal sectors of dislocation growth hillocks on the (101) face (*vicinal sectorality*), and 4) inclusion of sub-micron absorbing particles or defect clusters. Generally, dislocation bundles are a minor source of anomalous birefringence and have little effect on index homogeneity. Sectorality is a major source of index and phase matching inhomogeneities but is strongly dependent on the purity of the starting salt. Studies have also shown that Fe in the raw materials is the only important source of absorption at 3rd harmonic and that Fe both in solution and in the crystal exhibits optical properties similar to FePO molecules. For the highest purity salts available, vicinal sectorality is an important source of index inhomogeneity at growth rates in excess of about 20 mm/day and becomes important at lower growth rates only with lower quality salt[16].

The first center to be reported in KDP was the $[HPO_4]^-$ hole-center. Subsequent studies have shown that it consists of a hole trapped on an oxygen ion adjacent to a hydrogen vacancy [17-23]. The second center to be investigated was the $[H_2PO_4]^0$ hole-center, and its well-established model is a hole shared by two oxygen ions on one PO_4 unit in the otherwise perfect lattice [21-23]. In other words, the $[H_2PO_4]^0$ center is a self-trapped hole. A third intrinsic defect of significant interest in KDP is the interstitial hydrogen atom. EPR study[21,22] revealed a trapped electron center. Finally, the $[H_2SiO_4]^-$ hole-center is a fourth intrinsic defect of significant interest in KDP where a hole is trapped on an oxygen ion adjacent to a silicon impurity substituting for a phosphorus ion. The first three centers are not stable at room temperature; they will appear only in a transient form during harmonic generation applications of KDP. Previous investigators [24,25] have attributed the laser-

induced transient absorption observed in the visible and near-ultraviolet to the broad bands associated with the $[HPO4]^-$ and $[H_2PO_4]^0$ hole centers. The fourth center however is stable at room temperature. It is suggested that this greater thermal stability will introduce long-lived absorption bands that may adversely affect the performance of KDP crystals used as harmonic generators in high-laser-power environments.

In general, the pernicious effects of impurities on the performance of the crystal can be summarized as followed. When the distribution coefficient of impurity is high enough, the impurities become part of the crystal lattice. Upon excitation, an increase in the chemical potential in the vicinity of the point defects generates considerable lattice stresses. The lattice stresses can have different impact on the growth kinetics, morphology and the quality of the crystals. The adsorption processes at different sites[26–28] on the growing surface can cause growth inhibitions, which are well known in crystal growth[26–34]. Adsorbed impurities can even block the growing surface and, in consequence, stop the growth process. On the other hand, however, the adsorbed impurities may simultaneously lead to a reduction in the edge free energy *g* (so-called thermodynamic effect of impurities[34]), which results in an increase in the crystal growth rate (*growth promoting effect of impurity* (GPEI)). With increasing impurity concentration in solution, these opposing effects of adsorbed impurities may cause the growth rate to increase at first and then decrease passing through a maximum. Growth inhibition, however, is not the only consequence of adsorbed impurities. A comparison between the study of birefringence loss through depolarization loss technique and UV

absorption spectroscopy shows that the incorporation of impurities is one cause of optical distortion affecting the quality of crystals used in harmonic generators.

Nonlinear materials

Conventional KDP crystals with sizes longer than 20cm have been grown from saturated aqueous solutions at growth rates of approximately one millimeter per day along the primary optic (z) axis. Large KDP crystals (40 x 40 cm^2) have been grown from highly supersaturated solutions at rates exceeding 10 mm per day[35]. Depending on the growth process and the conditions, two sectors can be identified in a single KDP crystal. The pyramidal sector is a high-purity section grown along the optic (z) axis of the crystal using the conventional (*slow growth*) method. The prismatic sector, developed in directions (x, y) perpendicular to the primary optic axis, is a high-impurity region grown at supersaturation during the rapid growth process. Typically the impurity levels of materials from the two growth sectors differ. The prismatic sector of the crystal has significantly higher levels of impurities, while the pyramidal sector is relatively pure[36]. The level of impurity depends on the starting materials and the growth rate. Impurities in the crystals are measured by inductively coupled plasma-mass spectrometry (ICP-MS). The data in Table 4.3 shows that the level of impurities is different in the two growth sectors and depends on the identity of the individual impurities. Compared to the prismatic sector, the pyramidal region also shows considerably lower linear absorption. This trend is illustrated in Figure 4.1. The broad Fe defect-related absorption bands aforementioned depend on the impurity or doping content of the crystal. For this particular sample (KDP 303 MG-1), an apparent absorption band appears at around

Impurity Ions	Starting Salt (ppm)	Pyramidal Sector (ppm)	Prismatic Sector (ppm)
Sb (Antimony)	3.5	0.17	12.5
Pb (Lead)	0.2	0.1	0.2
Al (Aluminum)	<0.6	<0.3	7
Fe (Iron)	<0.2	<0.06	0.6
Rb (Rubidium)	3.8	0.8	0.8

Table 4.3. Impurity Analysis of KDP salt and different growth sectors

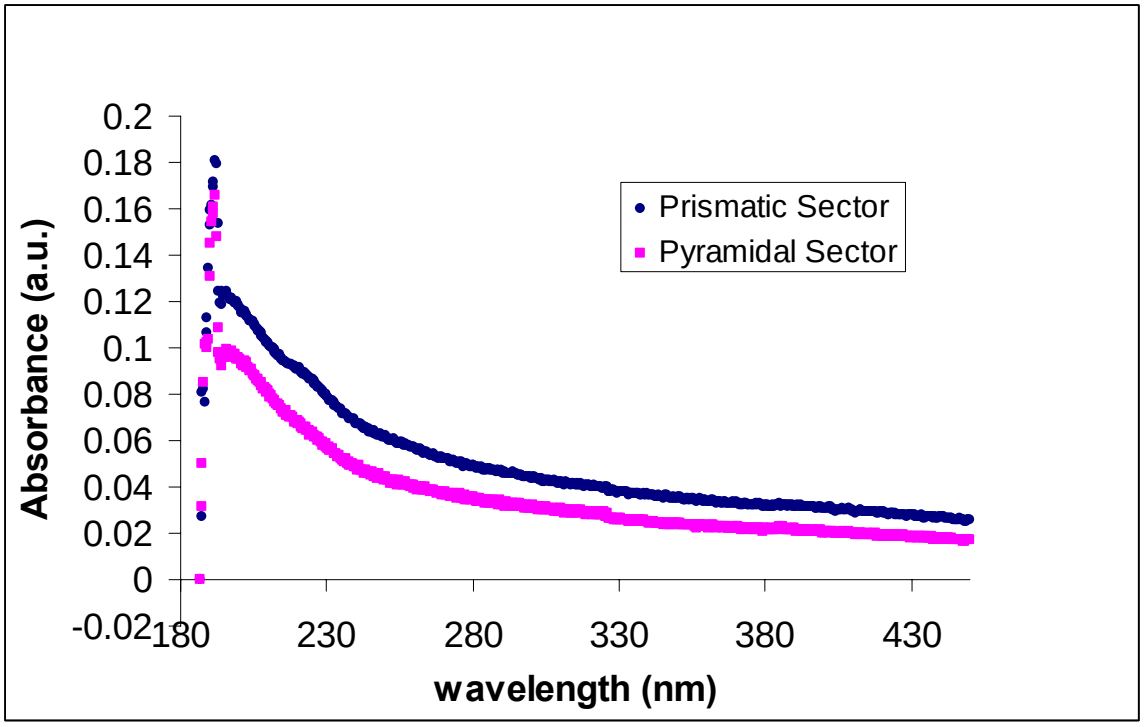

Fig. 4.1. Linear absorption spectra of two sample sites in the prismatic and pyramidal sectors of sample KDP 303-MG1

230nm in the prismatic sector, while no such particularity appeared in the pyramidal sector. This is indication that the sample was relatively undoped.

4.3 Experimental Setup

The experimental investigation carried on KDP crystals can be divided into two main sub-sections. Using the single beam open aperture (OA) Zscan technique, as described in *Chapter 2*, the nonlinear absorption coefficient of various doped KDP crystals was investigated. Since TPA is always present in KDP, we make use of the previously established knowledge[37] of the relationship between defects in the crystal and the observed enhancement of the TPA coefficient β to develop a new imaging technique that allows a two-dimensional TPA-based mapping of the entire crystal. The second part of this investigation concerns with the description and results of the TPA-based imaging of KDP crystals. In either part of this report, the laser source is a mode-locked Continuum Nd:YAG laser, which produces 25psec pulses at 355nm with excitation intensities ranging between 5-100 GW/cm^2 at the focus of a 20-cm lens. Illustrated in *Figure 4.2* is the experimental setup. The frequency tripled beam at 355nm is tightly focused into the nonlinear medium (i.e. KDP crystal), while special care is taken in order not to create additional damage in the material. This produces a beam radius, ω_o, ranging from 20-30 μm at the focus. By fixing the focal plane as the origin ($z=0$), the light transmittance through the medium is measured as the sample is moved along the propagation path (z) of the beam, in ($+z$) and out ($-z$) of focus. The measured transmittance is a function of the nonlinear absorption. To compensate for any laser intensity fluctuations the signal is

normalized by a reference signal produced by a beam-splitter placed before the Z -scan setup. The experimental data is collected using a custom-made LabView program.

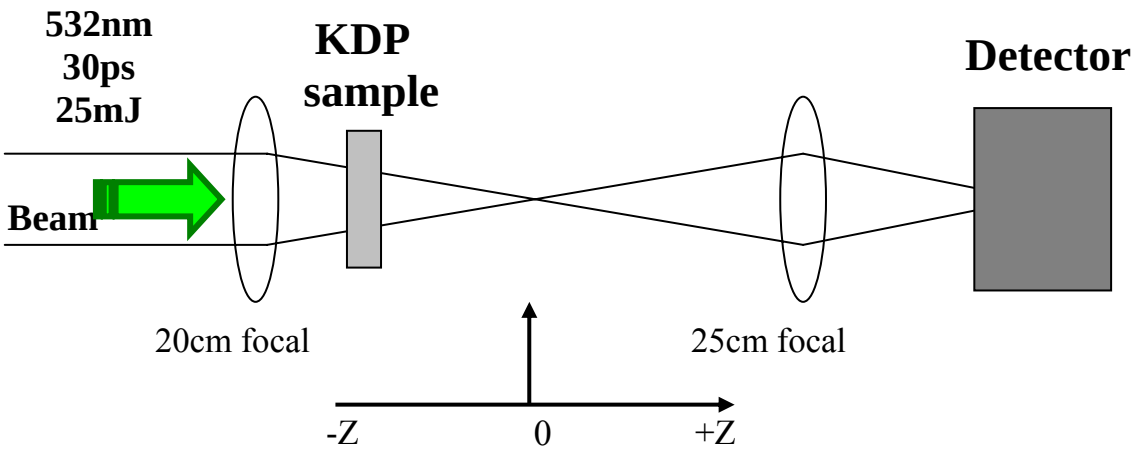

Figure 4.2. Experimental setup

The software controls the incremental step motion of the sample, fetches and processes data from the boxcar averager, and translation stages.

4.4 Nonlinear absorption in doped crystals

Two photon absorption (TPA) measurements of doped KDP crystals were performed. We scanned the face of the crystal samples while measuring TPA from point to point and then compared those measurements with the corresponding doping concentration.

Illustrated in Figure 4.3 is the experimental data for one of the KDP crystals (248PL#2). The measurement shown was carried out at position (1.5, 1.5). Positions are given in (x, y) coordinates relative to the lower left corner of the crystal surface facing the laser beam. The solid line in Figure is a theoretical fit using the equation for the nonlinear transmittance with open aperture Z-Scan. The fit gives a TPA coefficient β = 0.025±0.005 cm/GW. The peak irradiance at focus, I_o was 6 GW/cm^2. The peak intensity was calculated using the beam diameter inside the crystal obtained from the z-scan experiment. Due to self-focusing this value is about half the focal diameter measured in air. The crystal was inspected for optical damage before and after the measurement by monitoring visible light scattering from the crystal with a second harmonic beam at 532nm. No damage was observed at the pump energy and power (5-10μJ, 5-20GW/cm^2) used in these experiments.

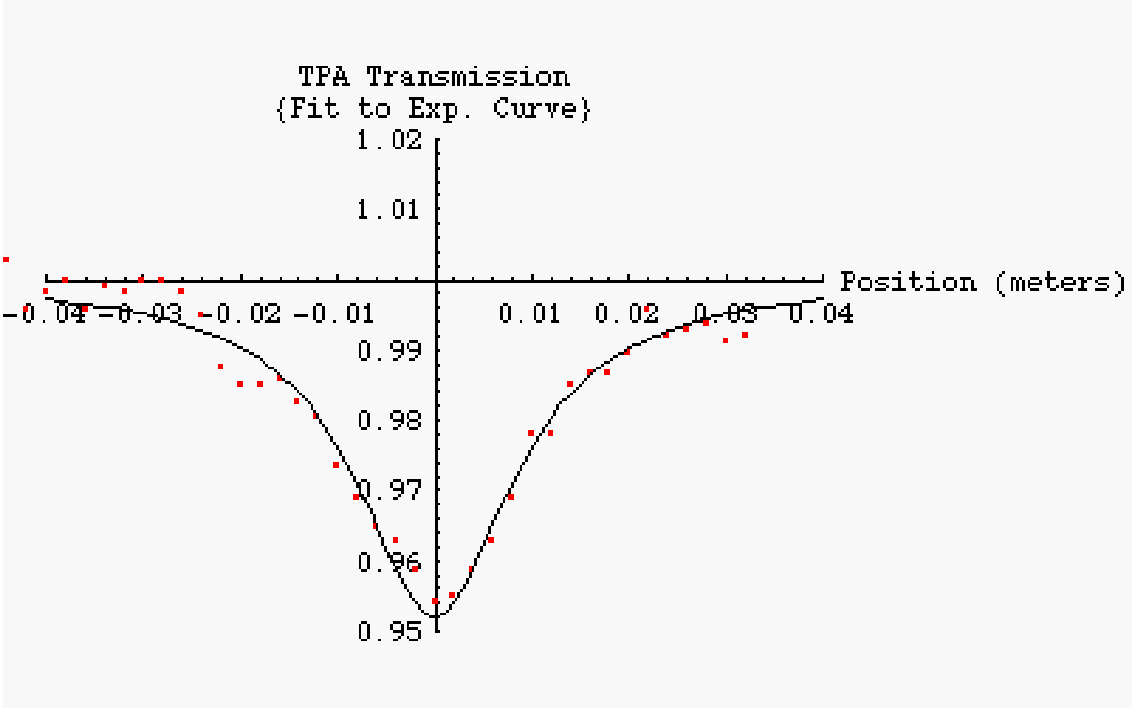

Figure 4.3 Results of the open-aperture Z-scan transmittance in a 1cm thick KDP crystal (sample 248PL#2). The solid line represents the theoretical fit. The dotted line represents experimental data. The fit gives $\beta = 0.025 \pm 0.005$ cm/G

Some results from our measurements are summarized in *Table 4.2*. The first column in the table identifies the samples. They were all KDP crystals grown using the rapid growth method. The second column gives the position in the crystal where the measurement was carried out. The third column gives the pump intensity. The fourth shows the relative

change in transmission due to two-photon absorption. The fifth column gives the optical density at 260nm. The optical density at this wavelength is a measure of doping concentration. All the samples showed some two-photon absorption. In some samples we observed good correlation between the magnitude of β and the doping concentration. For example, in the Fe doped sample, a larger two-photon absorption coefficient was measured in the prismatic sector where the Fe concentration level is higher. With 1ppm Fe doping, the two-photon absorption loss can be as high as 8% in the region with the highest concentration. The Fe doped sample results are illustrated in *Figure 4.4* and *Figure 4.5*. *Figure 4.4* presents the optical density at 260 nm at different positions in the crystal and clearly shows larger optical densities (higher impurity concentration) in the prismatic sectors.

TPA Coefficient (β) and Optical Densities (OD) of doped KDP Crystals					
Crystal	**Position/Sector (x, y) (cm)**	**Pump Intensity (GW/cm^2)**	**Modulation (%)**	**Optical Density At 260 nm**	**TPA coefficient (β) (cm/GW)**
KDP-Fe-1ppm (Sample#1)	(1.2, 1.5) Prismatic	16	9	0.9	0.015
"	(3.5, 2.5)	16	6	1.7	0.013
"	(3, 3)	16	4.5	1.8	0.012
"	(3.8, 2)	7	8	1.65	0.025
KDPFe-1ppm (Sample#2)	High Impurities Prismatic	23	6.12	1.4	0.010
"	High Impurities Prismatic	24	6.4	1.8	0.010
"	Low Impurities Pyramidal	23	2	0.3	0.002
"	Prismatic (3.8, 1)	7	8.1	0.15	0.03
KDP-As-10ppm	Prismatic (2.3, 1)	12	4	.35	0.008
"	(2, 1)	12	3.3	.35	0.008
"	(2.6, 1.5)	10	6	.38	0.02
"	(1.5, 1.5)	6	4.5	.35	0.025
"	(1,1)	9	2.5	.36	0.008
"	Pyramidal		2	0.12	0.004

Table 4.4. Summary of TPA measurements in doped rapid growth KDP crystals.

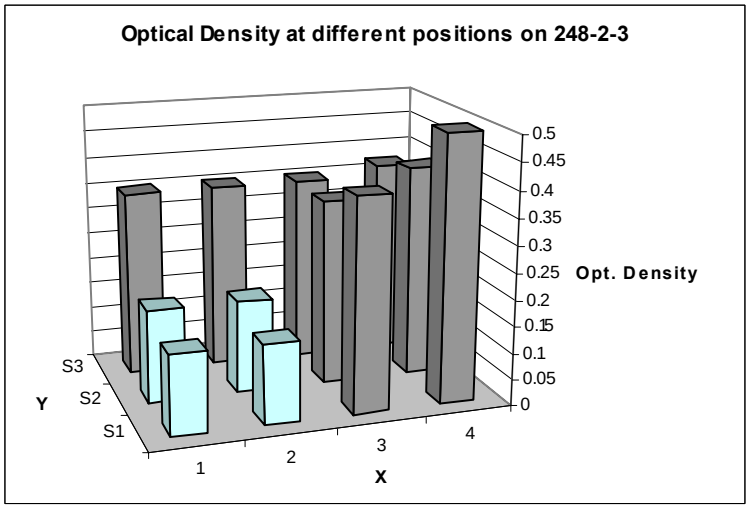

Figure 4.4 Optical Density (OD) at 260nm at different positions in a Fe doped KDP sample.

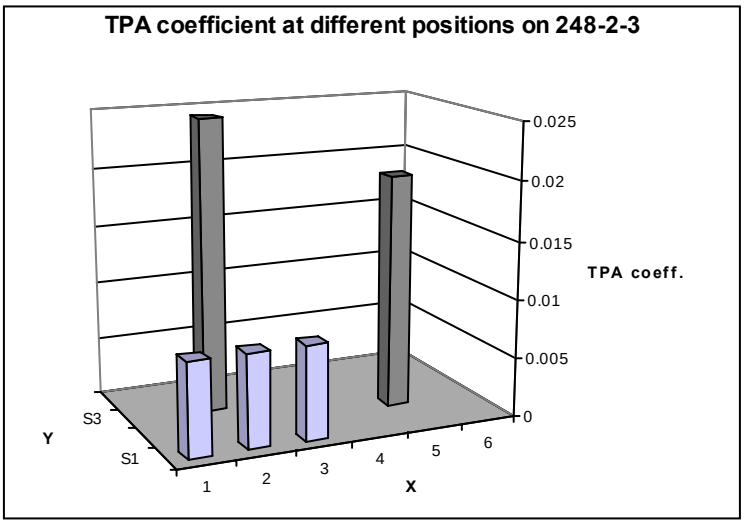

Figure 4.5 TPA coefficient β in the same Fe doped KDP sample as in **Figure 4.4**.

Figure 4.5 illustrates an excellent correlation between higher impurity concentration (larger OD values) and larger TPA coefficients. We believe that these results are of great interest because, such TPA changes within the same crystal could affect third harmonic generation efficiency. The measurements also show some TPA coefficient variations across the various crystals seemingly uncorrelated to impurities. The causes of these variations are not clear.

4.5 Two Photon Absorption Imaging

The TPA-based imaging section of the report can be divided into two sub-sections: imaging of optically induced damage sites created on the surface of KDP samples, and high resolution imaging of intrinsic defects in various KDP crystals.

The optically induced damages were created on pristine KDP crystals using an intense optical beam at 532nm. This resulted in the creation of visible damage sites ranging from 1 to 3mm in size. The face of the crystal was then imaged by performing open aperture Zscan measurement at each pixel site, revealing the two-photon absorption coefficient β at each point. This TPA-based mapping of the crystal revealed the position of the damage spots on the surface of the crystal as well as the value on or around the damage area. The measurements were carried out at 532nm using the same experimental setup shown in *figure 4.2*. The samples were mounted on a three-dimensional translation stage controlled by a home-made LabView VI program. The laser produced 25-psec pulses with energies per pulse ranging from a few micro joules to 3-mJ. Light transmittance through a KDP sample was measured in the far field as the crystal was moved along the propagation path

(z) of the beam, in (+z) and out (-z) of focus. The nonlinear absorption coefficient at every point on the surface was calculated from the measured minimum transmittance of the z-scan curve. The face of the crystal was scanned using the *XYZ* translational stage with less than 2 μm resolution. However, the actual resolution was limited by the diameter of the probe beam at the focus (in this case > 100 μm) and by time constraints (up to several hours for one scan depending on the resolution). In the resulting image, the position of a pixel is given by its X and Y-axis coordinates while the pixel itself represents the color coded value of the TPA coefficient β at that particular point. The scale on the right shows the variation of the TPA coefficient. *Figures 4.6, 4.7* and *4.8* show some of our experimental results. *Figure 4.6* shows a pixel-by-pixel plot of a 1 cm X 0.5 cm section of a KDP sample with a damage spot. The image is color coded according to the magnitude of the nonlinear absorption coefficient. The pixel size corresponds to the spacing between data points (about 500μm).

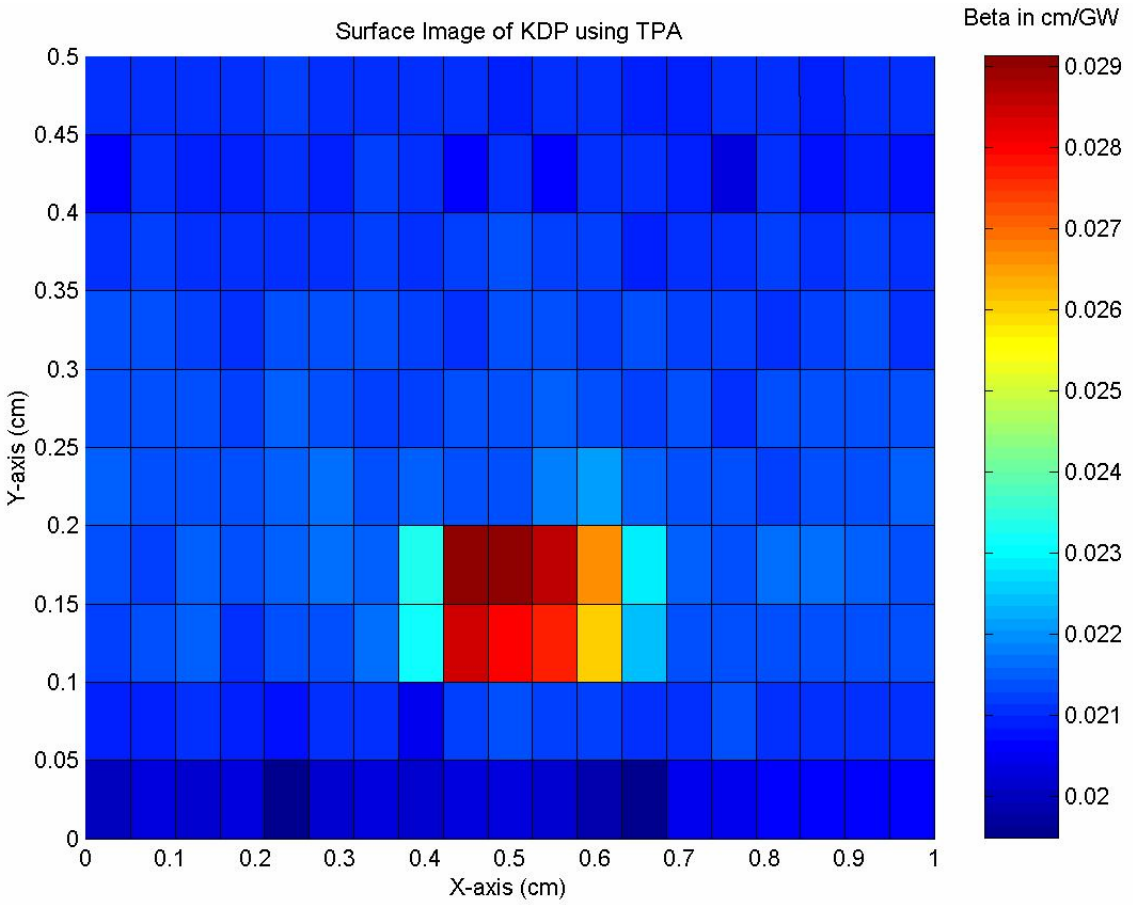

Figure 4.6. TPA image of damage spot #1

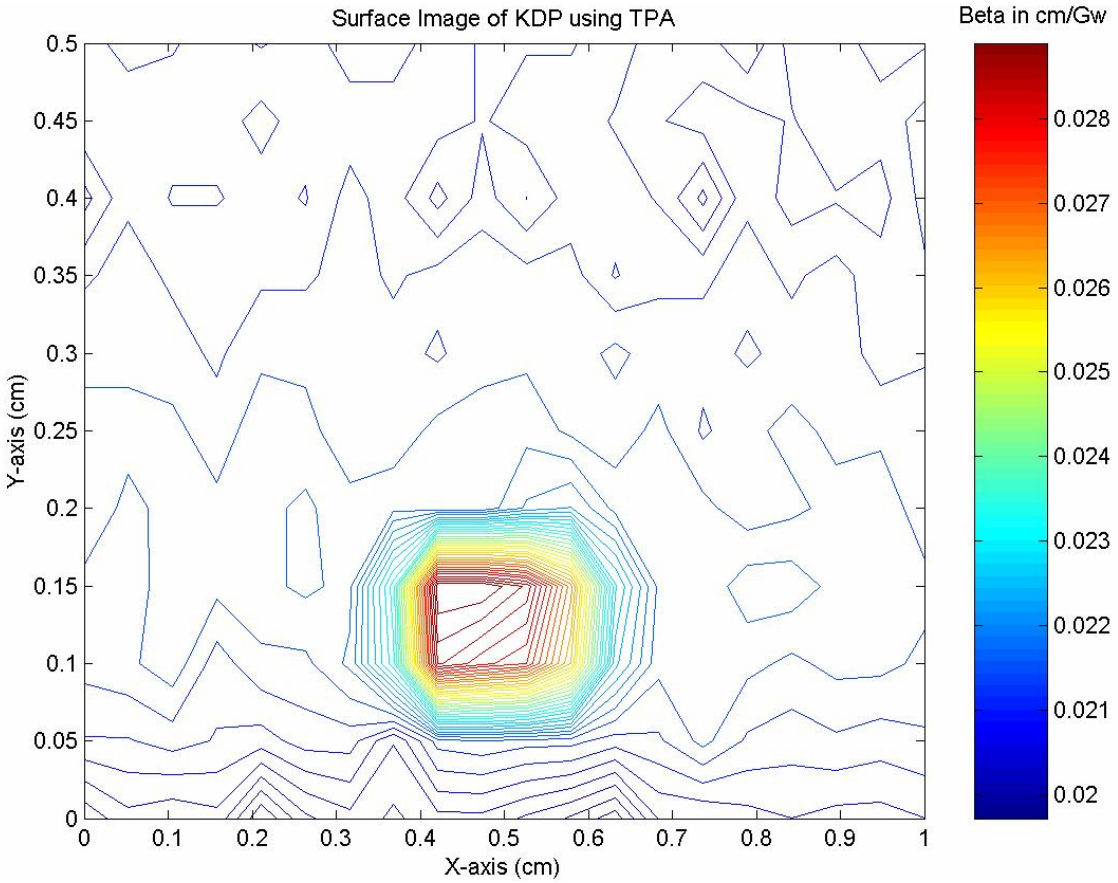

Figure 4.7. TPA image of damage spot #1 (Contour lines version).

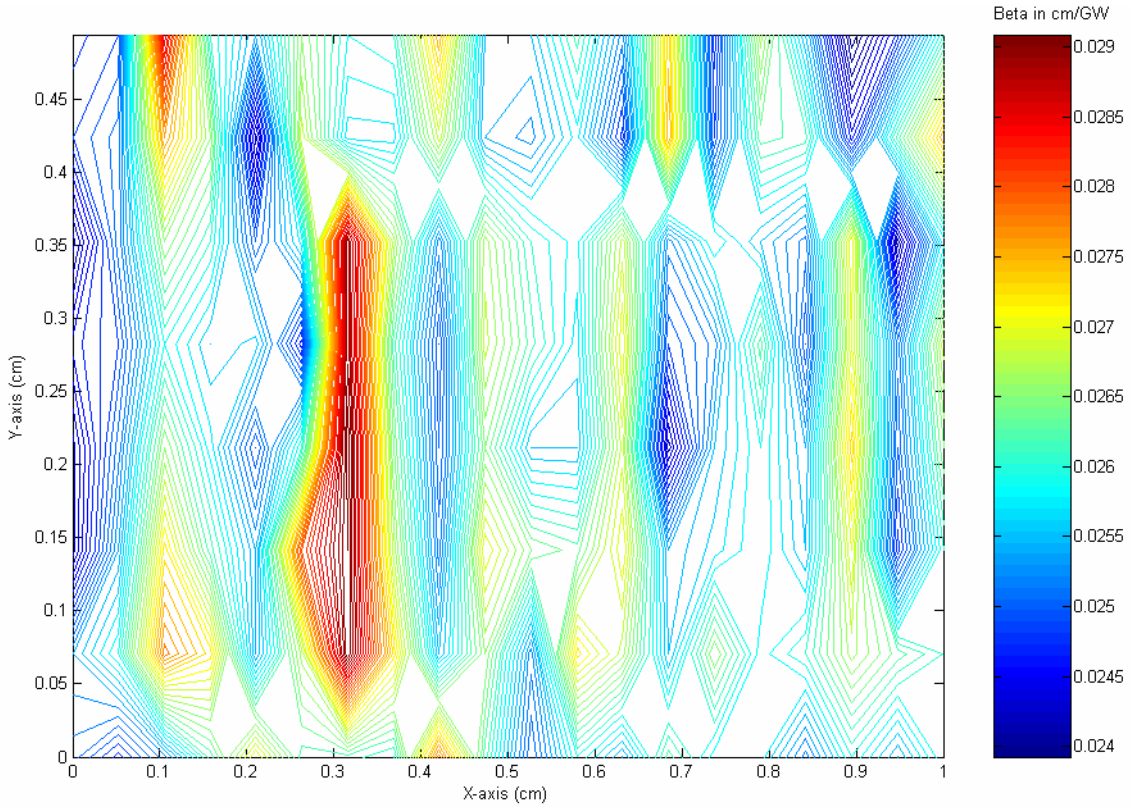

Figure 4.8 TPA image of damage sites #2 (center) and #3 (upper left corner)

Figure 4.7 shows the same data using a contour plot. Lines of the same colors have basically the same TPA value. *Figure 4.8* shows a different section of the sample with two strong damage spots in the center and the upper left corner of the scanned surface. These data clearly show the potential of this two photon imaging technique for high resolution mapping of defects in KDP crystals and their analogs.

We now illustrate, in *figure 4.9*, a high resolution TPA-based image of the surface of a pristine KDP sample. In this particular case, no damage spots were visible on the surface of the crystal. However both prismatic and pyramidal sectors were grown on the crystal. Since these two sectors obviously contain different density of microscopic impurities, our investigation aimed at detecting these sectors via the contrast due to the local variation of their TPA coefficient. In order to study the linear absorption properties of the sample, the crystal (a 5*5 cm^2 slab) was divided into twelve regions of equal size. A set of linear absorption spectra were performed on each region of the sample revealing *a priori* the variation in densities of energy traps. The recorded values of optical densities at 266nm were then plotted, constituting the bottom area of figure 4.10. In order to fully differentiate between prismatic and pyramidal sectors, a full scale image of a large portion of the sample had to be taken. Leaving a top and bottom margin of 1cm on the Y-axis as well as a left and right margin of 0.5 cm on the X-axis, a 4 by 3cm section of the 5 by 5cm sample was then imaged using the same picosecond optical system described earlier. Taking into account self-focusing behavior inside the crystal, the free-space diameter of the beam was corrected to yield a true on-axis intensity of ~10GW/cm^2.

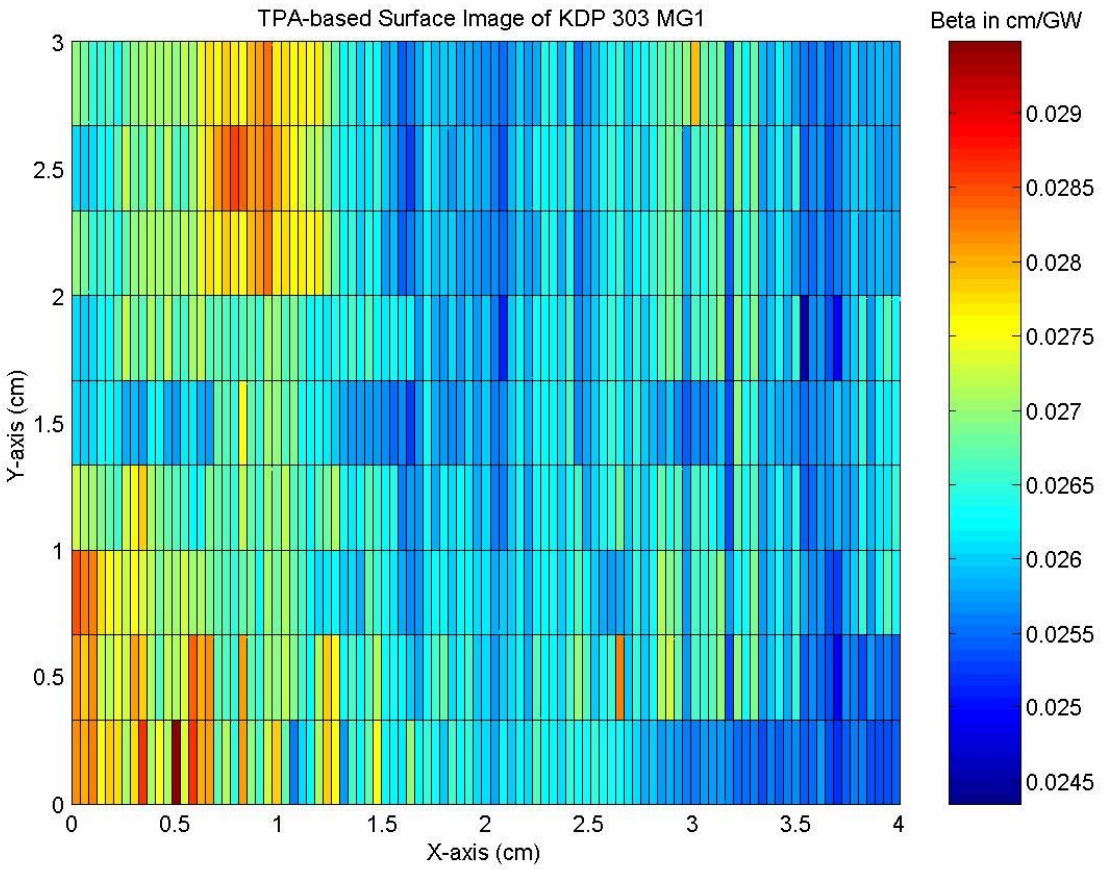

Figure 4.9 High resolution image of a 4*3cm section of sample KDP 303 MG-1

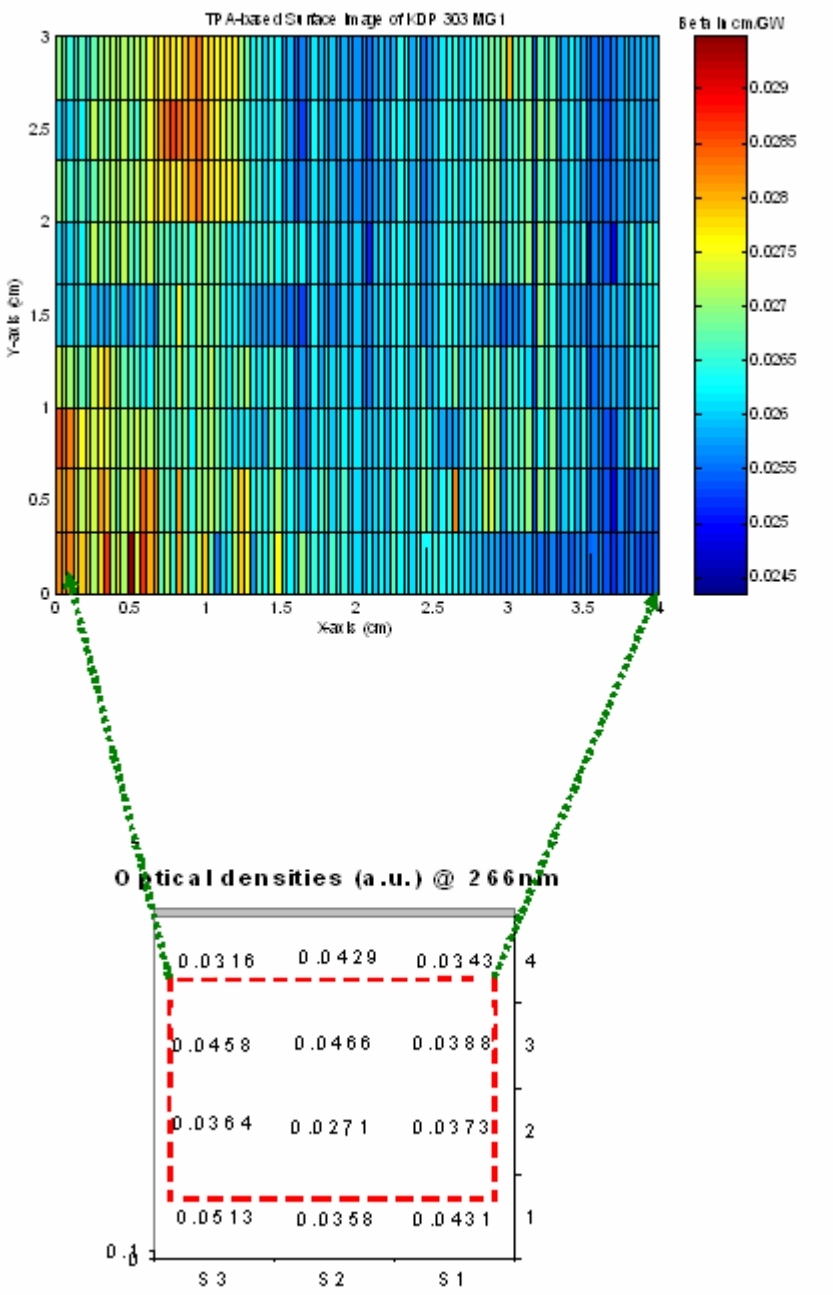

Figure 4.10 Correlation between local variation of TPA and variation in optical densities at 266nm in sample 303 MG-1. Dashed area shows actual region studied.

Even though a much higher resolution image could have been obtained, because of time constraint and frequent system crashes, a compromise was reached where the scan was performed with a resolution of only 2.5 points per mm.

Figure 4.10 shows an excellent degree of correlation between the linear absorption in the crystal and the losses due to nonlinear absorption. The image reveals a contrasting difference between the left side and the right sides of the crystal in terms of their impurity distribution. Our results have shown that the high impurity density prismatic and the less defective pyramidal sectors can thus be resolved very accurately with this TPA based imaging technique. It has been determined[36] that the laser damage threshold (LDT) while independent of sectorality or impurities in the material, is reduced by half at the boundary of the prismatic and the pyramidal sectors. This technique allows identifying such boundary and provides the freedom to either correct or avoid what would become the weakest link in the crystal. This procedure however does not provide a discrete identification of the various defects present in the crystal. A more complete study of the UV-absorption and two-photon absorption due to each impurity requires more experiments where the presence of impurities would be individually controlled. In order to achieve this goal, we propose to combine TPA measurements with state of the art imaging techniques to obtain high-resolution TPA images of the bulk and/or surface of the crystals.

4.6 Conclusion

We have performed extensive study of the prismatic and the pyramidal sectors of KDP crystals. Their respective characteristics were probed in terms of their impurity content, their linear and nonlinear optical properties. Open aperture Zscan experiments were carried on a variety of doped KPDs in order to establish correlation between defect-assisted linear absorption and two-photon absorption. The local variation of the two-photon absorption coefficient was used to design a TPA-based imaging technique allowing to generate a two-dimensional mapping of the defects in the crystal lattice. This TPA-based imaging technique however does not provide any information about the type of impurity present in the crystal. For example, since KDP always presents some degree of two-photon absorption, detection of single nanometer sized absorbing defect would require a substantial enhancement of the signal to noise ratio of the system in order to detect any contribution above the noise background. The overall resolution and scan time of the system can be further improved, most likely by reducing even more the beam waist at the focus, by using faster stepping motors and motor-controllers, by optimizing the software, by increasing the scanning speed and/or by using multi-point excitation with micro-lens arrays. On the other hand, enhanced TPA-based mapping can be obtained by combining TPA measurements with other state of the art imaging techniques to obtain high-resolution TPA images of the bulk and/or surface of the crystals.

References

1. L. N. Rashkovich, *KDP-family Single Crystals* (A. Hilger, Bristol, 1991)
2. W. L. Smith, Appl. Opt. **16**, 1798 (1977).
3. D. Eimerl, Ferroelectrics **72**, 95 (1987).
4. Ming Yan, Rich Torres, Mike Runkel, Bruce Woods, Ian Hutcheon, Natalia Zaitseva and Jim DeYoreo, SPIE **2966**, 11 (1997).
5. S. G. Demos, M. Staggs, M. Yan, H. B. Radousky, and J. J. De Yoreo, Optics Lett. **24**, 268 (1999).
6. J. M. Vail, J. Phys. Chem. Solids **51**, 589 (1990).
7. N.Y. Garces, K.T. Stevens, L.E. Halliburton, M. Yan, N.P. Zaitseva, J.J. DeYoreo, Journal of Crystal Growth **225** 435–439 (2001)
8. M.A. Paesler, P.J. Moyer, Near-field Optics, Wiley/Marcel Dekker, New York, (1994)
9. P.A. Temple, Appl. Opt. **20**, 2656 (1981).
10. L.M. Sheehan, M.R. Kozlowski, D.W. Camp, in: G.J.
11. S. G. Demos, M. Yan, M. Staggs, H. B. Radousky and J. J. De Yoreo, Microscopic Spectral Imaging of Defect Centers in KDP, Lawrence Livermore National Laboratory
12. R. Dorsinville, A. Walser, and R. Pino, Two-Photon Absorption Imaging of KDP crystals. LLNL Report # (1999)
13. G. A. SmolenskiĬ, V. A. Bokov, and V. A. Isupova, *Ferroelectrics and Antiferroelectrics* (Nauka, Leningrad, 1971).
14. E. Dieguez, A. Cintas, P. Hernandez, J.M. Cabrera, J. Crystal Growth **73**, 193 (1985).
15. I.M. Pritula, Yu.N. Velikhov, Some aspects of UV-absorption of NLO KDP crystals, in: R.B. Lal, D.O. Frazier (Ed.), Operational Characteristics and

Crystal Growth of Nonlinear Optical Materials, Proceedings of SPIE, Vol. **3793**, 1999 pp. 202–208.

16. Microscopic Spectral Imaging of Defect Centers in KDP, S. G. Demos, M. Yan, M. Staggs, H. B. Radousky and J. J. De Yoreo, Lawrence Livermore National Laboratory
17. W. E. Hughes and W. G. Moulton, J. Chem. Phys. **39**, 1359 (1963).
18. K. Tsuchida, R. Abe, and M. Naito, J. Phys. Soc. Jpn. **35**, 806 (1973).
19. K. Tsuchida and R. Abe, J. Phys. Soc. Jpn. **38**, 1687 (1975).
20. J. A. McMillan and J. M. Clemens, J. Chem. Phys. **68**, 3627 (1978).
21. J. W. Wells, E. Budzinski, and H. C. Box, J. Chem. Phys. **85**, 6340, (1986).
22. S. D. Setzler, K. T. Stevens, L. E. Halliburton, M. Yan, N. P. Zaitseva, and J. J. DeYoreo, Phys. Rev. B **57**, 2643 (1998).
23. K. T. Stevens, N. Y. Garces, L. E. Halliburton, M. Yan, N. P. Zaitseva, J. J. DeYoreo, G. C. Catella, and J. R. Luken, Appl. Phys. Lett. **75**, 1503 (1999).
24. J. E. Davis, R. S. Hughes, and H. W. H. Lee, Chem. Phys. Lett. **207**, 540 (1993).
25. C. D. Marshall, S. A. Payne, M. A. Henesian, J. A. Speth, and H. T. Powell, J. Opt. Soc. Am. B **11**, 774 (1994). // S. G. Demos, M. Yan, M. Staggs, J. J. De Yoreo, and H. B. Radousky, Appl. Phys. Lett. **72**, 2367 (1998).
26. R.J. Davey, J.W. Mullin, J. Crystal Growth **23**, 89 (1974).
27. R.J. Davey, J. Crystal Growth **34**, 109 (1976).
28. K. Sangwal, Prog. Cryst. Growth Character **32** (1996).
29. N. Cabrera, D.A. Vermilea, Growth and Perfection of Crystals, in: R.H. Doremus, B.W. Roberts, D. Turnbull (Eds.), Wiley Inc., New York, 1958, p. 393.
30. M. Ohara, R.C. Reid,ModelingCrystal Growth Rates from Solution, Prentice Hall Inc., Englewood Cliffs, NJ, 1973.
31. A.A. Chernov, Modern Crystallography III: Crystal Growth, Springer, Berlin, 1984.
32. N. Kubota, J.W. Mullin, J. Crystal Growth **152,** 203 (1995).

33. W.J.P. van Enckevort, Science and Technology of Crystal Growth, in: J.P. van der Eerden, O.S.L. Bruinsma (Eds.), Kluwer Academic Publishers, Dordrecht, 1995, p. 355.
34. R.J. Davey, Industrial Crystallization 78, in: E.J. de Jong, S.J. Jancˇ ic´ (Eds.), North-Holland Publ., Amsterdam, 1979, p. 169.
35. N. P. Zaitseva, I. L. Smol'skii, and L. N. Rashkovich, Sov. Phys. Crystallogr. **36**, 113 (1991).
36. Ming Yan, Rich Torres, Mike Runkel, Bruce Woods, Ian Hutcheon, Natalia Zaitseva and Jim DeYoreo, SPIE **2966**, 11 (1997).
37. Michael Etienne, Ardie Walser, Roger Dorsinville, "*Nonlinear Optical Absorption in laser induced modified regions of fused silica substrates"*, *Optics Communications* **240**, No. 4-6, P 417- 421 , 2004

Chapter 5

Third-order nonlinear optical properties of Cadmiun Sulfide-Dendrimer Nanocomposites

5.1 Introduction

Semiconductor nanocrystals embedded in various organic materials have received some recent theoretical and experimental attention as interesting nonlinear materials, fueled in part be the potential for controlling their resulting physical and chemical properties along with their nonlinear optical and fluorescent characteristics[1]. Their usage is expected to span an ever growing area ranging from drug delivery system to optical switching devices, optical limiting devices, and quantum dots LEDs and lasers. Semiconductor nanocrystals represent a class of quasi-zero-dimensional objects where bulk crystalline structure is preserved but due to quantum confinement they present molecularlike discrete energy spectra, exhibiting very strong size dependence[2-5]. Although there exists a variety of methods to fabricate nanostructures, one effective and simple way is to use a polymer (dendrimer) as a nanoreactor to synthesize and stabilize the quantum dots (Qdots) [6]. These inorganic-organic hybrid materials are of particular interest since the resonant coupling between the Frenkel excitons of the organic molecules and the Wannier-Mott excitons of the inorganic semiconductor Qdots in these hybrid nanostructures leads to novel and interesting effects including higher oscillator strength, enhanced optical nonlinearity, and efficient Forster energy transfer (ET) making the nanostructures highly versatile for laser and light emitting applications, and nonlinear optical (NLO) devices[7,8]. Thaong and Birman[7,9] have proposed a hybrid exciton model

for a quantum dot-organic system. According to this model a hybrid exciton appears in the system owing to strong dipole-dipole interaction of the Frenkel exciton of the organic molecules with the Wannier-Mott transfer exciton of the quantum dot array. At resonance between these two types of excitons, the optical nonlinearity is expected to be very large. Other researchers have shown that in these systems saturation and phase-space filling effects may result in strong intensity dependent nonlinearities. Phase-state filling effects are a direct consequence of the Pauli Exclusion Principle and state that *states* in phase space that are already occupied are no longer accessible in optical transitions or available for exciton formation. In other words, one can not optically create two e-h pairs (bound or free) if they require the same k-states. Since the excited electrons must obey the Pauli principle, and are restrained to occupy a specific range of energies within the conduction band, there is a decrease of the refractive index for frequencies below the band edge and an increase in the refractive index for frequencies above the band edge. The strong intensity dependent nonlinearities are therefore a result of the strong saturation of the exciton absorption, producing a large change in the refractive index.

Schwerzel et al. [10] have measured the third-order nonlinear optical response of 3.3 nm cadmium sulfide nanocrystals in solution and in Langmuir-Blodgett multilayers of a polydiacetylene polymer at 530 nm and have shown an increase in the NLO response compared to the undoped polymer film. Wang et al. [11] have reported large resonant third order nonlinearity in a perfluoroethylenesulfonic acid polymer with 5.5 nm CdS particles. They attribute most of the large NLO response to the bleaching of the exciton absorption. More recently, He et al. [12] used the Z-scan technique to study the irradiance dependence

of the excitonic nonlinear absorption of CdS nanocrystals capped with dodecanethiol in chloroform solutions. They demonstrated evidence of third-order and fifth order nonlinear response for 3.0 and 2.3 nm sized nanocrystals resonantly excited between 430 and 450 nm. Du et al. [13] have investigated the NLO of hybridized 3-6 nm CdS-polystyrene nanocomposites and have shown that the nonlinear response at 532 nm was irradiance dependent indicating the possibility of higher order nonlinearity.

The main focus of NLO research in organic/semiconductor nanocomposites has been directed toward the synthesis and characterization of organic/semiconductor nanocomposites with large two-photon absorption (TPA) in the visible and near infrared for potential application in optical limiting[9-13,14]. Large TPA values require large values of the imaginary part of the third order nonlinear susceptibility. This, however, usually requires, as in the case of CdS nanoparticles, relatively large particle sizes (>3 nm) within the limits of confinement requirements[15]. As will be seen subsequently, for smaller particles the exciton bands are shifted toward the blue and the nonlinear response in the visible and near infrared, away from resonance, is expected to be mostly real. There have been few, if any, reported measurements of the real part of the NLO response outside resonance in semiconductor-organic nanocomposites. In this chapter, we report on the observation of the magnitude and sign of the third-order nonlinear susceptibilities of Cadmium Sulfide (CdS) quantum dots embedded in matrices of dendritic molecules having different core, generation, and functionalities. The observed enhanced nonlinear responses are a direct result of quantum confinement effects in the dots and the exciton-exciton interaction in the hybrid structures.

5.2. Theoretical background

5.2.1. Quantum dots, quantum confinement and Wannier-Mott excitons

Quantum dots are quasi-zero dimensional system where electrons and photons are confined in their movement in all directions. The consequences of quantum confinement can be understood by recalling two basic and fundamental principles of quantum mechanics; namely the electronic structure must obey the Schrodinger equation and follow the de Broglie momentum-wavelength relationship[16]. The following analysis is adapted from Nanostructured Materials and Nanotechnology[17].

In bulk crystalline lattices, the electron states are guided by the Schrodinger equation

$$H\Psi(r) = [-(h/8\pi m)^2 \Delta + V(r)]\Psi(r) = E\Psi(r) \qquad (5.1)$$

where H is the Hamilton operator, Δ the kinetic energy operator ($\frac{\partial^2}{\partial p^2} + \frac{\partial^2}{\partial q^2} + \frac{\partial^2}{\partial r^2}$) and $V(r)$ is the periodic potential representative of the inter-atomic lattice spacing a; i.e. $V(r+a) = V(r)$, h is Plank's constant and m is the mass of the electron. The eigenfunctions, or solutions to the above equation are the well-known Bloch functions[17] with periodicity a equals to the lattice spacing

$$\Psi(r) = e^{ikr}u(r) \qquad (5.2)$$

here *u(r)* represents the interatomic potential well and is also periodic; i.e. *u(r+a)=u(r), k* is the wave vector determined by the symmetry and spacing of the lattice. The solution to the above wave equation for a periodic potential predicts energy bands with discontinuities. The simplest approximation, which yields sensible results and provide insight into more complicated solutions, is the so called parabolic band approximation. The eigenvalues for this approximation are

$$E(k) = (hk)^2 /(8\pi m_{e,h}) \tag{5.3}$$

where $m_{e,h}$ is the effective mass of the electron or hole (missing electron in an allowed energy state).

Fig. 5.1 shows the electron and hole quantized levels in the model of parabolic band. The arrows indicate allowed optical transitions which couples electron and hole states of the same symmetry. It can be seen that in nanocrystals, the first allowed transition corresponding to the first exciton peak (or absorption onset) involves a transition between the *1S(h) – 1S(e)* levels, which also identifies the energy gap of the nanostructure. The envelope function of the ground sate (n = 1, l = 0, m = 0) shows quantized carrier energies that are degenerate with respect to the quantum number m. The energy of the states increases in the order 1*S*, 1*P*, 1*D*, 2*S*. Since the Coulomb interaction scales with the NC radius a as a^{-1}, while confinement energies are proportional to a^{-2}, in the strong confinement regime, the states are classified with respect to the orbital angular momentum l (l=0, 1, 2, …, corresponding to states with *S, P, D,* …, symmetries), its

projection m (m = 0, ±1, ±2, …, ± l) and the quantum number n (n = 1, 2, 3,…) which counts the states of the same symmetry. The envelope functions with different n and/or l numbers are orthogonal, and the optical transitions are only allowed between the states of the same symmetry ($l = l'$, $n = n'$). Because in semiconductors the hole mass is typically greater than that of the electron, the electron levels are much more sparse than the hole levels.

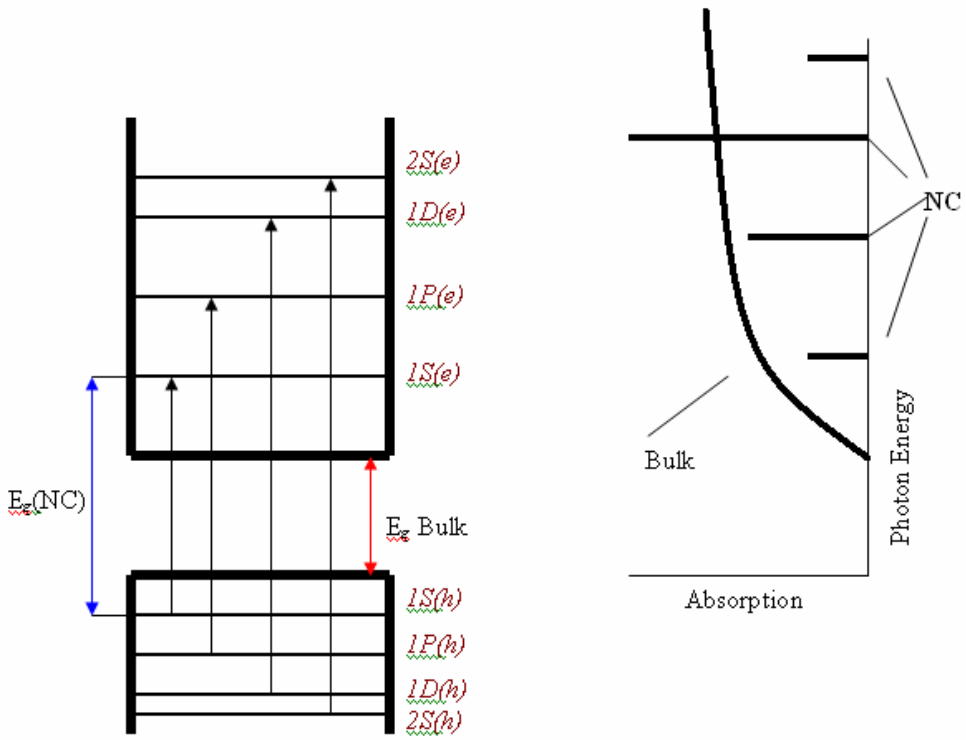

Fig 5.1. Electron and holes quantized levels in the model of parabolic band. The plot on the right is an illustration of the discrete structure in nanocrystals compared to the continuous absorption spectrum of a bulk material.

In general a nanostructure can be approximated to a spherical crystal with a diameter *D(=2r)*. In order to be called a quantum structure, this diameter must be smaller that the de Broglie wavelength, λ

$$\lambda = h / p \tag{5.4}$$

where $p=hk/2\pi$ is the momentum of the electron in the sample at temperature *T*. Using $E = (3/2)kT = p^2/2m$, where *E* is the kinetic energy, we find a λ at room temperature (~300° K) to be ~ 6 nm. This means that for a spherical crystal of diameter $D \leq 6$nm, the electrons or holes wave packets are squeezed somewhat unnaturally into a space smaller than usual. This new configuration results in the electron taking a higher energy than it would normally have in the host structure, therefore the natural exciton Bohr radius is larger than the host crystal structure. Such small host crystals are called *quantum dots* and the resulting physical state is called *quantum confinement*.

In order to simplify our quantum mechanical study of the quantum dot, let's consider an infinite spherical well. Neglecting the Coulomb interaction for simplification, we can take the Hamilton operator as:

$$H = -(h^2/8\pi m_e)\Delta_e - (h^2/8\pi m_h)\Delta_h + V_e(r_e) + V_h(r_h) \tag{5.5}$$

and the potential $$V_i(r_i) = \begin{cases} 0 & \text{for } r_i < R \\ \infty & \text{for } r_i > R \end{cases} \qquad i = e,\ h \tag{5.6}$$

The normalized solutions to equation (5.5) are given through spherical harmonics and Bessel functions[18]. With the condition that the Bessel functions must vanish at the surface of the quantum dot sphere, we can find the photon energy required to produce an electron-hole (exciton) pair:

$$h\upsilon = E_g + (h^2 / 8\pi m_{e,h})(\chi_{n,l} / R)^2 \qquad (5.7)$$

Equation 5.7 shows evidence that an additional term has been added to the band-gap energy E_g as a consequence of quantum confinement. This will translate into an effective band-gap shift that is proportional to $1/R^2$ in the quantum regime. In other words, since R is the length (radius) of the confining box (sphere), the gap decreases as R increases.

For two successive energy levels E_n and E_{n+1} , the energy difference becomes

$$\Delta E = (2n+1)\frac{h^2}{(8ml^2)} \qquad (5.8)$$

This is evidence that in nanostructures, although the crystalline structure is preserved, a fundamental consequence of the three-dimensional confinement is the apparition of molecularlike discrete energy spectra (fig. 5.1). In fact, the absorption spectrum of a NC consists of narrow peaks of spacing ΔE, and the distance between absorption peaks decreases with increasing NC radius (smaller ΔE) until they merge into the continuous spectrum of the bulk material.

Another aspect of figure 5.1 is the region between the top of the valence band and the bottom of the conduction band. This region is the so-called energy gap of the material. An electron can be excited to the conduction band by a photon, for example, leaving a hole in the valence band. If an electron-hole pair is bound together by their attractive Coulomb interaction, it is referred to as an exciton. An exciton can be considered as an exotic atom with its own atomic or Bohr radius, able to move through the crystal, transporting energy. Depending on the material, the exciton radius and the excitonic interaction, excitons are classified in different categories.

5.2.2 Dendrimers and Frenkel excitons

Since the first "cascade synthesis" procedure was reported by Vo¨gtle[19] and improved and patented by Denkewalter[20-21], there has been an increased interest in dentritic structures due to their versatility and functionality. Dendrimers form an exciting new group of macromolecular materials in between the monomolecular and polymeric regimes. They are essentially nanometer size macromolecules with repeating units arranged in a hierarchical self-similar fashion around a core to give highly branched treelike structure. The generation of the dendrimer is defined as the number of focal points (cascade points) when going from the core to the surface, a generation 5 (G5) dendrimer thus has 5 cascade points between the core and the surface. In general, a dendritic structure is a result of a number of chemical reactions involving Michael addition, cyanoethylation and Raney nickel reduction. For example, the poly(propylene Imine) dendrimer is a result of a total of 256 individual reactions.

a)

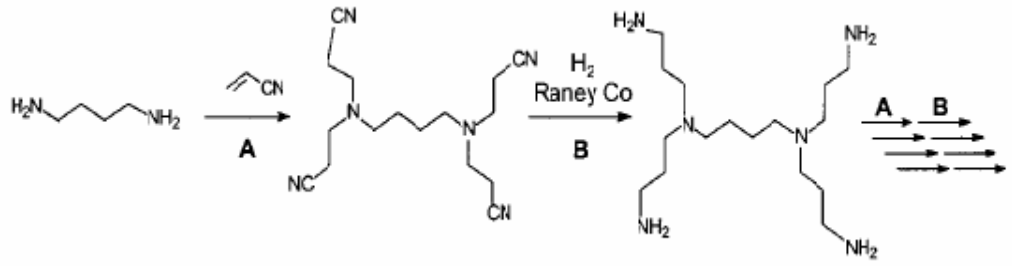

b)

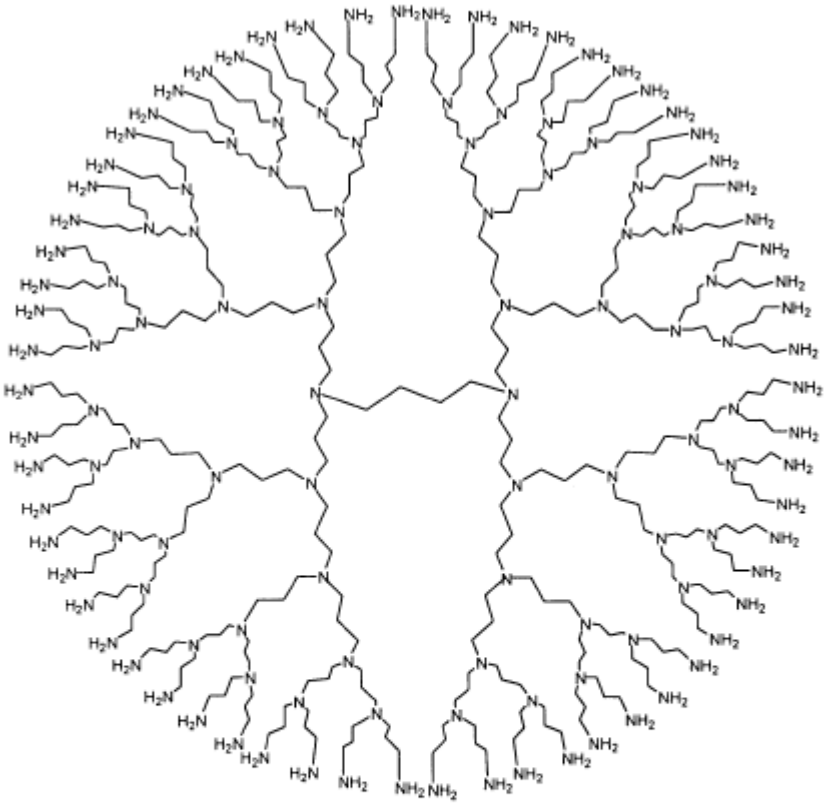

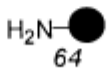

or

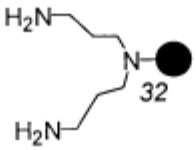

Fig 5.2 **a)** Basic synthesis pathway of a branching unit in a dendrimer **b)** A poly (propylene Imine) dendrimer with 1,4 diaminobutane core and its molecular symbols

From a nanotechnologic point of view, dendrimers are very attractive as building blocks in nano-devices because the locations of the core, branches, and surface functionalities can be controlled and tuned with high accuracy[22]. Furthermore, the cavities between subsequent ramifications form ideal trapping regions and hence the dendrimer becomes a very versatile host for a number of photoactive nanoguests. Recently, several dendrimers functionalized with various nonlinear optical (NLO) chromophores have been developed[23] and potential applications as electro-optic[24], two photon absorbing or second harmonic generating[25] materials have been investigated. Similar investigations have been carried out in various transition metal dendrimer nanocomposites and have demonstrated optical-limiting effects at a variety of wavelengths as well as laser pulse durations[26] in these systems.

The main focus for NLO research in these hybrid systems has been the quest for an enhancement of the optical nonlinearities via a conjugated optical response from the different constituents of the new system[27]. Typically, in a semiconductor QD quantum size effects produce a large separation in energy states. Because of the increased distance between the two allowed energy levels, the most common excitonic entities found in semiconductors are the so called Wannier-Mott excitons or large radius excitons. Those excitons are essentially a weakly bound electron-hole pair characterized by a weak oscillator strength and a large electron-hole distance (~30-100 Å). The internal structure of Wannier–Mott excitons can be represented by hydrogen-like wavefunctions. Such a representation results from the two-particle,

Coulombic electron–hole states in a crystalline periodic potential. In the Wannier-Mott excitons, the wave functions overlap each other to produce exciton resonance.

On the other hand, in molecular crystals, the covalent binding within a molecule is strong compared to the van der Waals binding between molecules. The most common type of exciton found in a molecular or strongly ionic system is therefore the Frenkel exciton. A Frenkel exciton is represented as an electronic state of a crystal in which electrons and holes are placed on the same molecule. Customarily Frenkel excitons in organic crystals have radii a_F, comparable to the lattice constant: $a_F \sim a \sim 5$ A° . The oscillator strength of a Frenkel exciton is thus very strong, comparable to a molecular oscillator strength.

Fig. 5.3[17]. Illustration of a Wannier-Mott exciton in a QD and of a Frenkel exciton in an polymer

It has already been shown[28] that when many quantum dots are arranged together in an array, an exciton inside a quantum dot can be considered as not localized in that dot,

but it can propagate through the lattice via the mechanism of exciton transfer processes. This energy transfer process is similar to electronic mobility in metals and is due to multipole interaction of excitons in different dots. In the event that the semiconductor quantum dots are surrounded by an organic medium, it is expected that there will be energy interchange between the excitons of the dots and those of the organic molecules. The interaction of those two different types of exciton is expected to generate a hybrid exciton having on one side the very strong oscillator strength of the Frenkel exciton and on the other side the very large exciton radius of the semiconductor[29-31].

In fact, there are in general two pathways for energy transfer between the semiconductor and the dendrimer. Depending on the conditions, energy can be transferred from the quantum dot to the dendrimer or vice versa. In the first case, when the distance between the quantum dots and the dendrimer is large, the coupling between the two excitons is weak. Therefore the level widths are much greater than the resonance interaction energy. In this situation dephasing (*transverse relaxation*) processes destroy the coherent superposition of excitonic states and incoherent energy transfer occurs from the subsystem where dissipative processes are slow (*semiconductor donor*) to the subsystem where dissipation is rapid (*organic molecule acceptor*). This corresponds to the Fo¨rster energy transfer. In the strong confinement regime, the Forster energy transfer mechanism can be quite rapid (~ 20 to 100ps) and makes possible the transfer of a substantial part of the energy from a semiconductor quantum dot to the organic molecules surrounding the dot, with possible subsequent deexcitation of the dot. A study[32] has been performed on such system where

semiconductor quantum dots were electrically pumped, the Forster energy transfer was used to couple energy to surrounding dendritic entities. In such conditions, the Wannier-Mott exciton luminescence is quenched and the organic luminescence is efficiently turned on. In the second case (strong coupling) the characteristic dipole–dipole resonance interaction energies of Wannier–Mott excitons and Frenkel excitons are greater than the widths of the corresponding levels. This leads to the appearance of elementary excitations of a new type, which are a coherent superposition of two types of excitons. In this way, the desirable properties of both the inorganic and organic material unite and overcome the basic limitations for the figure of merit of the exciton resonance nonlinearities. The latter theoretical results constitute the basis of our investigation. There have also been some studies performed on metal-dendrimer nanocomposites[33] and nanosecond Z-scan and picosecond DFWM of CdS nanocrystals[24] alone, but no optical characterization of CdS quantum dots in dendrimer matrix is readily available. In this thesis, picosecond and femtosecond single beam Z-scan technique is used to investigate both the nonlinear refractive index and the TPA coefficient of hybrid systems made of Cadmium Sulfide (CdS) quantum dots embedded in dendrimers of different generations. The samples studied were made of either a G4 or G5 poly(propylene Imine) dendrimer matrix having diaminobutane (DAB) core or a G6 *PAMOH* dendrimer having Ammonia core. The investigations were performed both in the active region near or below the energy gap where the nonlinearities are resonant due to single photon resonance enhancement as well as in the transparent region where anharmonic motion of bound electrons give rise to a much weaker but ultrafast nonlinearity that is essentially real.

5.3. Material preparation

Small (~2 to 4nm) CdS Qdots were synthesized using different dendritic templates. The synthesis of CdS Qdots was carried out under carefully controlled reaction conditions (concentrations, temperature, pH, solvent, and the rate and number of sequential additions). In order to investigate their nonlinearities, thin films were deposited by spin casting in Nitrogen atmosphere from methanol solutions. The resulting samples consisted of a 1mm thick quartz substrate with a 100-500 nm nonlinear optical film on one side. The stability of the samples has been a major drawback in the investigation. Among the samples studied, only the G5-dendrimer-stabilized CdS Qdots were stable at room temperature, both in solution and in solid state for several weeks. The other samples decayed rapidly after a day or two, even in a Nitrogen environment. *Figure 5.4* illustrates the configuration of the different samples studied. It is believed that the CdS quantum dots are retained inside the voids of the dendritic nanocontainers. In this geometry, two important parameters should dominate the overall nonlinearity of the system: the dot to dot spacing and the size of the nanoparticles. The dot to dot spacing refers to the average distance between Qdots and has an immediate impact on the concentration of the Qdots. Since the overall nonlinear response is a conjugate response resulting from the interaction between Qdots, the dot to dot spacing is expected to be the dominant factor influencing the nonlinear response. In general, the smaller the generation of the dendrimer, the smaller the distance between dot, which will consequently generate a higher dot to dot interaction. This argument is in good harmony with hydrodynamic diameters[34] data obtained for the dendrimers and illustrated in *Table 5.1*. The hydrodynamic diameters

also known as *equivalent dendritic sphere diameters* increase typically as a function of the generation number, and predicts that a smaller dendritic molecule will foster a smaller dot to dot distance. The second most important parameter to consider is the size of the

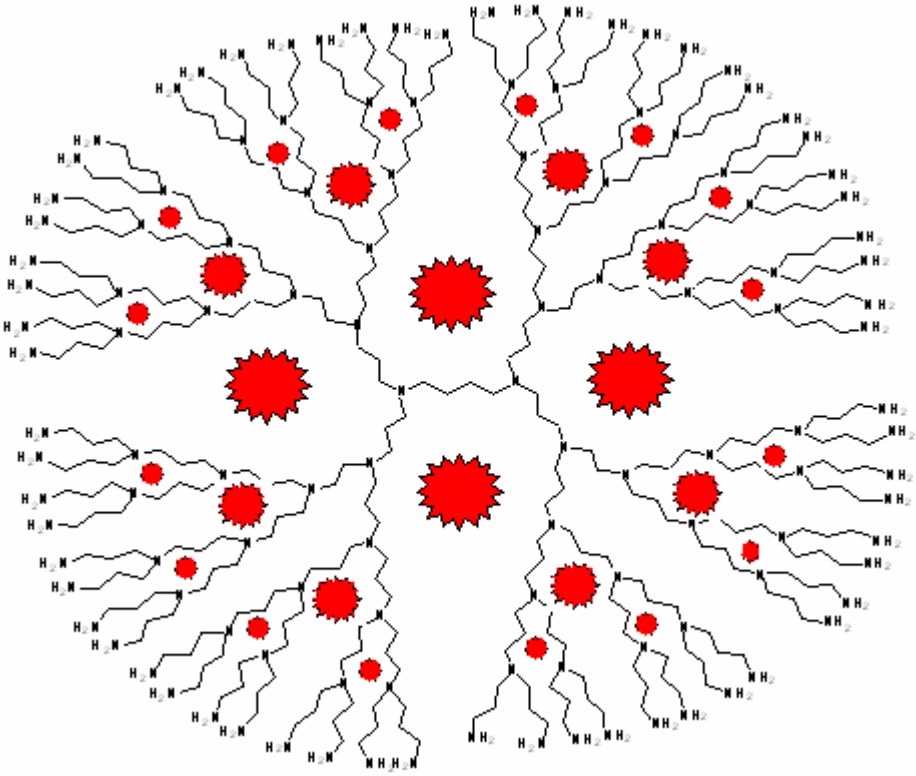

Fig 5.4 Representation of a G5 dendrimer matrix, showing the nanocavities and the size distribution of the trapped Qdots

nanoparticles. As mentioned in *Section 5.2.1*, depending on the size of the Qdot radius, different confinement regimes can be achieved. However because of their comparable size (2~4 nm), all three samples studied are confined to the laws of the strong confinement regime, therefore the immediate consequences of a stronger confinement

will be a blue shift in the linear absorption spectra, along with a change in the energy gap and the relative position of the first excitonic state. Although these parameters will ultimately have an impact on the nonlinearity of the system, their effects will not overwhelm the nonlinear response. Another key issue that will tend to lessen the impact of the size of the Qdots is that in the dendrimers, the nanovoid volume is generation dependent. In other words, the spacing between the branching units varies with the generation number *(Figure 5.4)*. As a result, the size of the trapped Qdots will follow the same size distribution of the nanovoids. This dependency will translate into a broadening of the size distribution of the trapped Qdots, blurring the nonlinear enhancement due to size contribution. Based on these arguments, we can therefore predict that the size of the dots will not be the definite factor in the nonlinear response of such hybrid systems.

Several features characteristic of the hybrid systems investigated are summarized in *Table 5.1* as a function of the generation of the dendrimers. Sizes were obtained both through high-resolution TEM pictures as shown in figure 5.5 (*G4 and G6 samples*) and theoretically using the Brus Model[35] (*G5 sample*). In evaluating the Qdots size using the Brus model, the dots were assumed to be spherical nanoparticles. In this case, the size dependence of the absorption edge and therefore the radius of the dots can be evaluated using:

$$E(R) = E_g + \frac{h^2\pi^2}{2R^2}[\frac{1}{m_e} + \frac{1}{m_h}] - \frac{1.8e^2}{\varepsilon R} \qquad (5.9)$$

where E_g is the Energy gap, m_e and m_h the electron and hole effective masses and R, the nanoparticle radius.

Figure 5.6 shows the linear absorption spectra of the different semiconductor-dendrimer nanocomposites studied. The blue shift of about 150nm in the G5-CdS samples compared with bulk CdS (~520nm) is expected in CdS Qdots of ~2 to 4nm in diameter[36]. It is clear

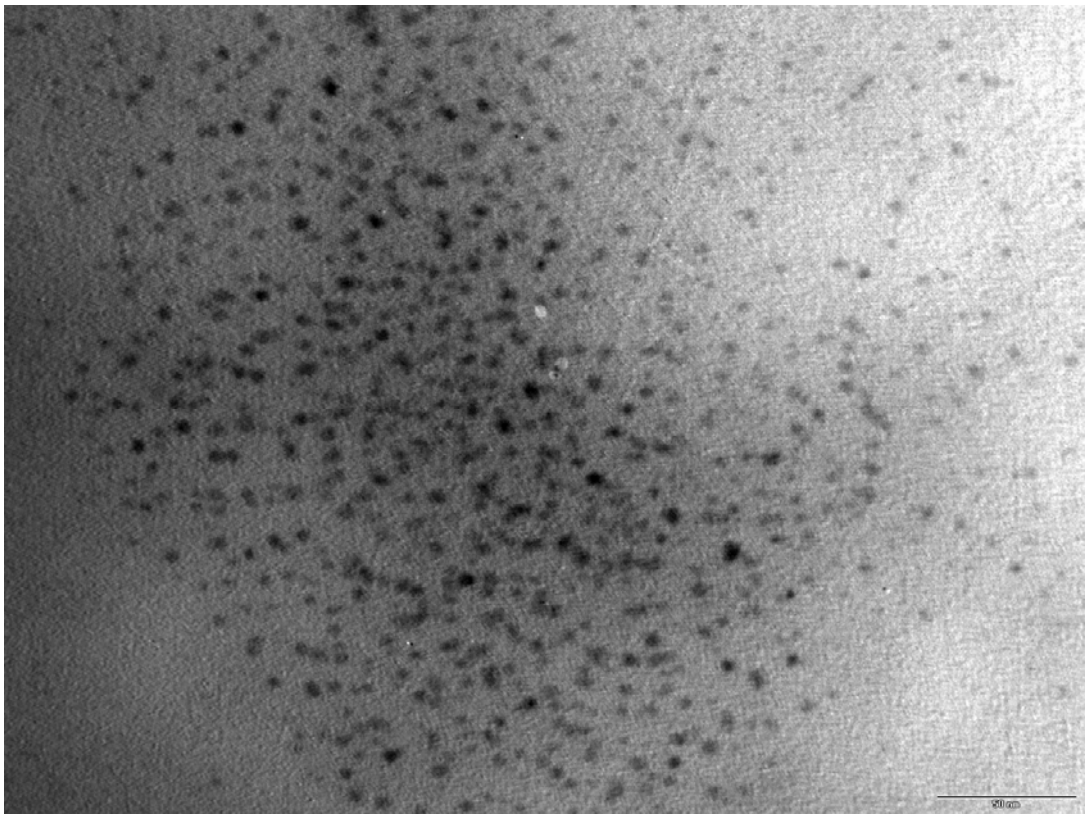

Fig. 5.5 TEM image of the G6 PamOH-CdS Qdots viewed with a 50 nm scale. The average dot size is ~3 to 4nm.

from the absorption curves that the position of the lowest excitonic peak varies from 380 to 330nm depending on the generation of the dendrimer and the size of the trapped Qdots. Although energy spectra in nanoparticles are expected to be discrete, size distribution of

the Qdots along with the response from the dendrimer tends to smear out the absorption spectra. However, the position of discrete absorption peaks can be revealed by taking the first derivative of the absorption spectrum with respect to energy ($\Delta\alpha/\Delta E$). Figure 5.7 illustrates the absorption spectrum of the G5-CdS Qdot sample alone. Taking $\Delta\alpha/\Delta E$ leads to the inset figure which shows the presence of three absorption peaks. The peaks labeled *P1, P2* and *P3* are situated at 3.33eV (372nm), 4.12eV and 4.6eV respectively.

	First exciton onset	Emission Peak	Hydrodynamic diameters[34]	Average Qdot size
G4 CdS-DAB		482 nm	5 nm	> 2.3 nm [a]
G5 CdS DAB	372 nm	478 nm	6 nm	~ 2.3 nm [b]
G6 CdS PamOH	342 nm	465 nm	7 nm	< 2.3 nm [a]

Table 5.1.Variation of nanostructure properties as a function of the generation of the dendrimers a) High resolution TEM measurements b) Brus theoretical model

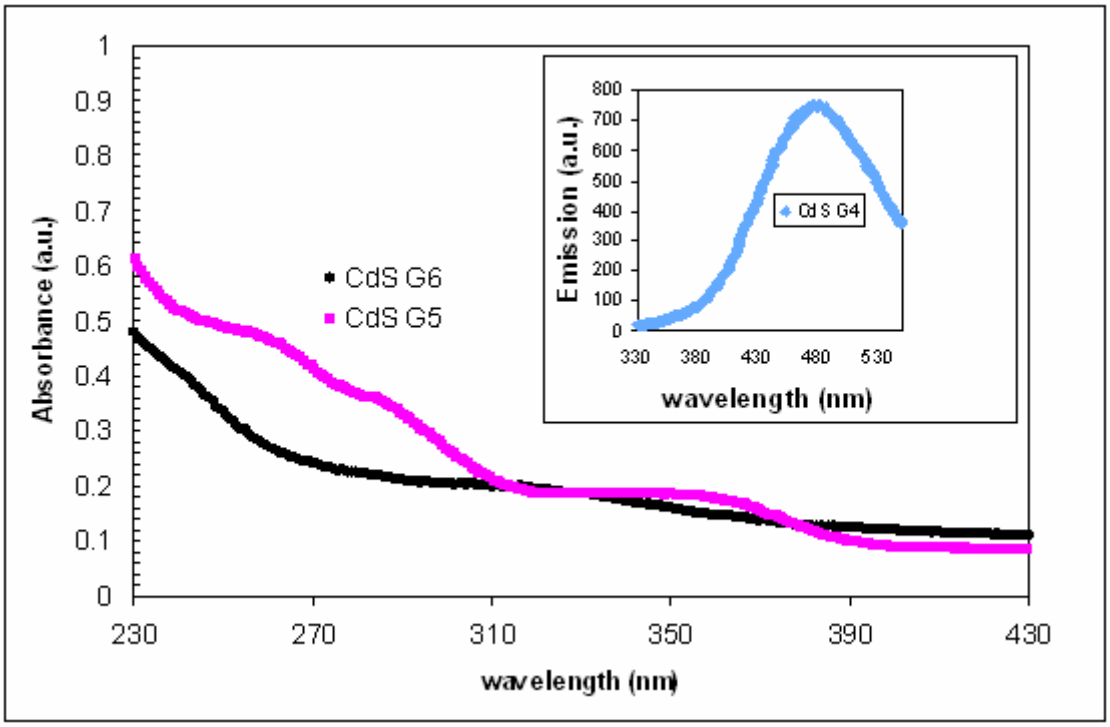

Fig. 5.6 Absorption spectra of the G5 and G6-CdS Qdots samples studied. Inset is emission spectra of the G4-CdS Qdots sample.

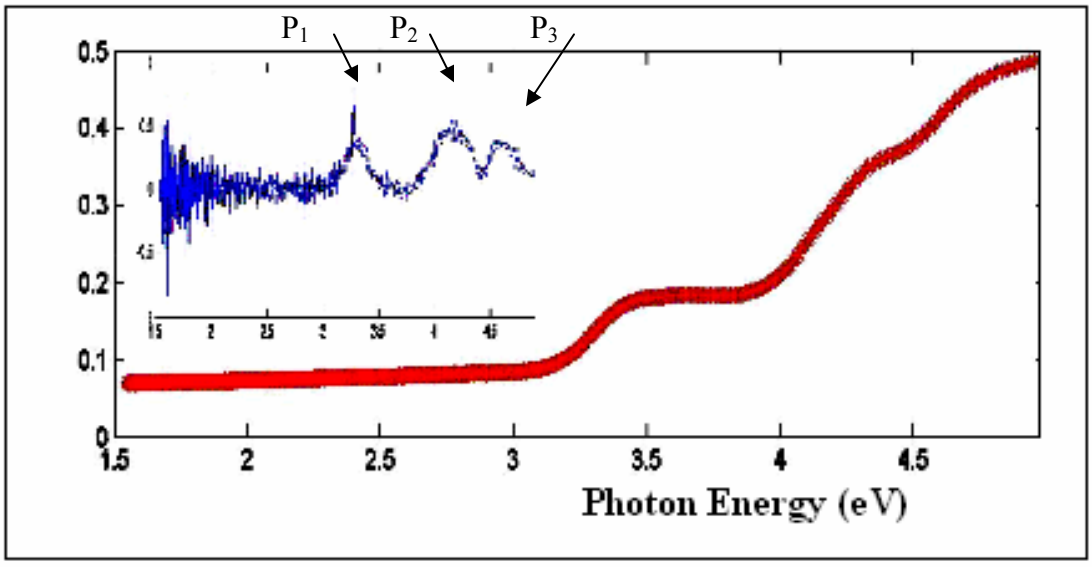

Fig. 5.7. Room-temperature absorption spectrum of G5-CdS nanocrystal film. The first derivative *(inset)* shows the discrete-like features of the absorption spectra.

The inset in *Figure 5.6* shows the fluorescence spectra of the G4-CdS sample with broadband emission extending from 380 to 650 nm, the emission peaking at 482 nm. In general, fluorescence spectra show a red shifted emission peak as the dot size increase. Table 5.1 summarizes both the position of the onset of the first exciton peak and the relative position of the emission peak as a function of the generation of the samples.

5.4. Experimental setup

Single beam Z-scan technique[37] was used to characterize the NLO response at both femtosecond and picosecond optical pulse durations. In the picosecond case, the mode-locked YAG laser described in *Section 2.1.2* provided the laser pulses with 30-ps duration at 355 nm, 532 nm and 1064 nm at a 20-Hz repetition rate with energies per pulse ranging from few microjoules to several mJ[38]. In the femtosecond study, the Ti-Sapphire regenerative amplifier generated 800nm pulses of 120-fs duration with an average pulse energy close to 1mJ. Other wavelengths were obtained either by harmonics generation (400nm and 267nm) or by using the output of an optical parametric amplifier *(OPA800).* In either case, the intensity of the incident beam was adjusted by an attenuation setup consisting of a half wave plate and two crossed Glan-Thomson polarizers. In the picosecond experiment, the laser beam was tightly focused to a $1/e^2$ beam radius ω_o of about 200 μm. The incoming pulses were split into two by a beam splitter. The reflected beam was taken as a reference to account for laser fluctuations while the transmitted pulse was focused onto the sample. For the closed aperture measurements the aperture was placed at a distance of more than 1 m away from the

focus point. The light transmission through the aperture was detected and recorded, using a fast detector and a boxcar averager interfaced with a computer.

Picosecond results in the CdS-G5 sample

Picosecond Zscan experiments were carried out in the CdS-G5 samples alone. Short picosecond pulses were used at all three wavelengths with 1064nm in the transparent region, 532nm well below the lowest absorption band, and 355nm in quasi-resonance with the lowest excitonic band at 372nm in the CdS-G5 samples. Figure 5.8 shows the z-scan responses of a G5-DAB- dendrimer with CdS quantum dots and of a pristine G5-DAB film at 532 nm. The nonlinear coefficient is clearly negative for the G5-DAB-QD sample while the response of a pristine G5-DAB film is positive. At the excitation level used in these measurements (~600 MW/cm^2) the contribution to the nonlinear response of the quartz substrate alone was negligible. The Z-scan response of the quartz plate at higher excitation levels was used as a reference to calibrate the experimental set-up. The third order nonlinear coefficient values $\chi^{(3)}$ and the nonlinear refraction indexes n_2 were calculated from the difference between the normalized peak and valley transmittances following the standard Z-scan method. We found that $\chi^{(3)}$= (5.8 ±1) x 10^{-10} esu for the G5-DAB dendrimer and $\chi^{(3)}$= (-2.2 ±1) x 10^{-9} esu for the CdS-G5 Qdots sample. Recalling that the spectrum of the CdS-G5 exhibits a broad absorption peak between 320 nm and 350 nm with an absorption onset at about 400nm, and that the pristine G5-DAB (not shown) has an absorption onset at about 300nm, therefore, the absorption between 300 nm and 400 nm can be attributed to the CdS nanoparticles. It is clear from the

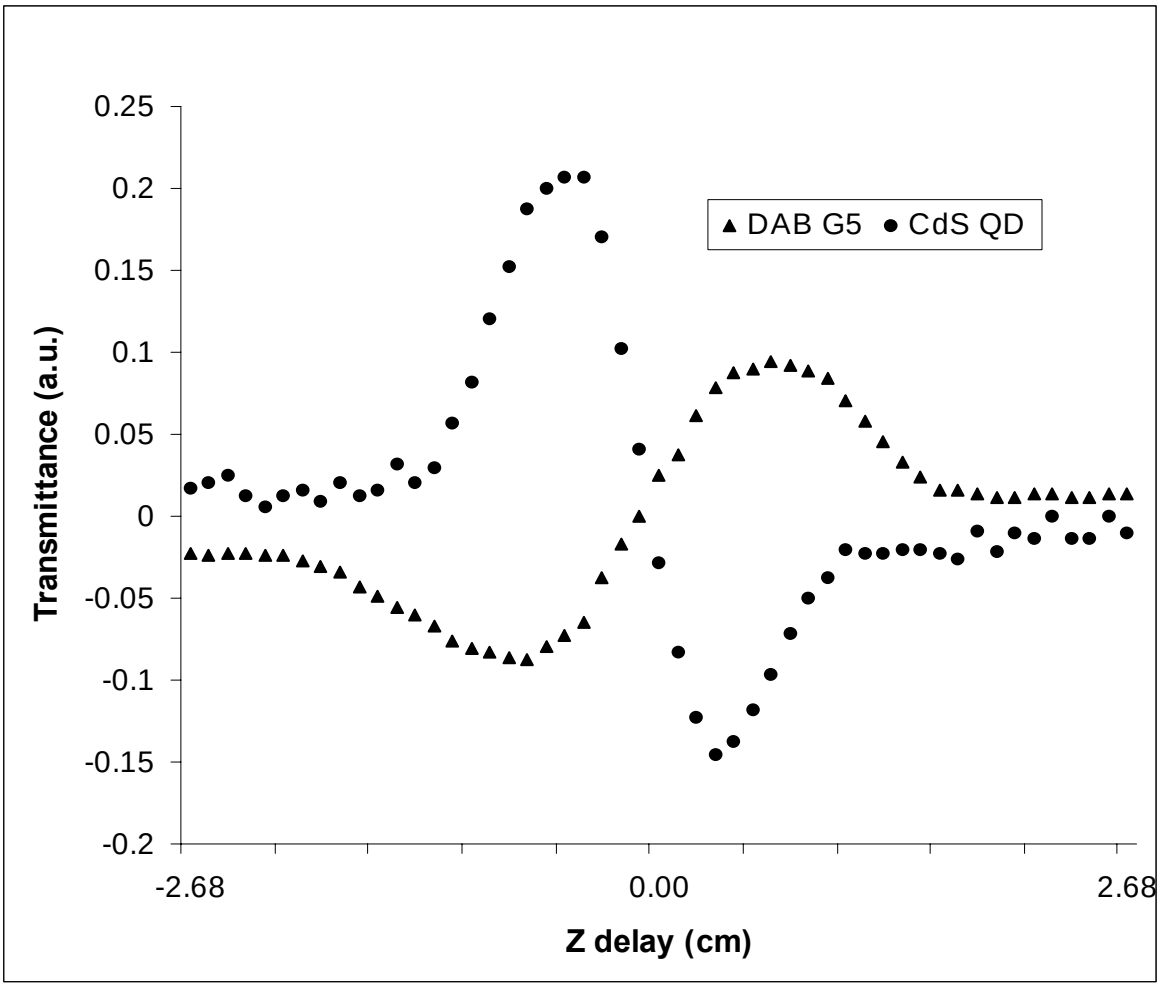

Fig 5.8 Picosecond Z-scan response of a CdS-G5 DAB film (● negative response) and a pristine G5-DAB film (▲ positive response)

absorption curve that the 532nm excitation wavelength is well below transmittance without the far field aperture. In this case, the transmittance is only a function of the nonlinear absorption. The normalized transmittance without an aperture is given by[14]:

$$T(z) = \sum_{m=0}^{\infty} \frac{\left(\frac{-\beta I_o L_{eff}}{1 + z^2 / z_o^2} \right)^m}{(m+1)^{3/2}}, \qquad (5.10)$$

where I_o is the incident laser intensity at the focus point and β is the TPA coefficient. The open aperture transmittance with Io = 250 MW/cm^2 at 532 nm from a G5-DAB-QD sample and a pristine G5-DAB film are shown in Fig. 5.9. At this intensity level the transmittance from the substrate does not show any TPA behavior. A curve fit to the experimental data using Eq. (5.9) yielded β = 32.4 cm/GW, the pristine G5-DAB-dendrimer and β = 43.6 cm/GW for the G5-DAB-QD film. If we recall the characteristics of a good optical switch as described in Chapter I, we realize that the G5-DAB-QD shows the two basic fundamental properties of a good switching device. It presents a substantially high value of n_2 along with a relatively small value of β the TPA coefficient. A common figure of merit for all optical waveguide devices with TPA losses is $T = \beta\lambda/n_2$, where λ is the wavelength. Lower values of T are better for applications such as optical switching. We found T ~ 10^{-3} at 532 nm for the G5-DAB-QD film. This value of T is smaller when compared to available data for organic polymers or organometallic systems[15].

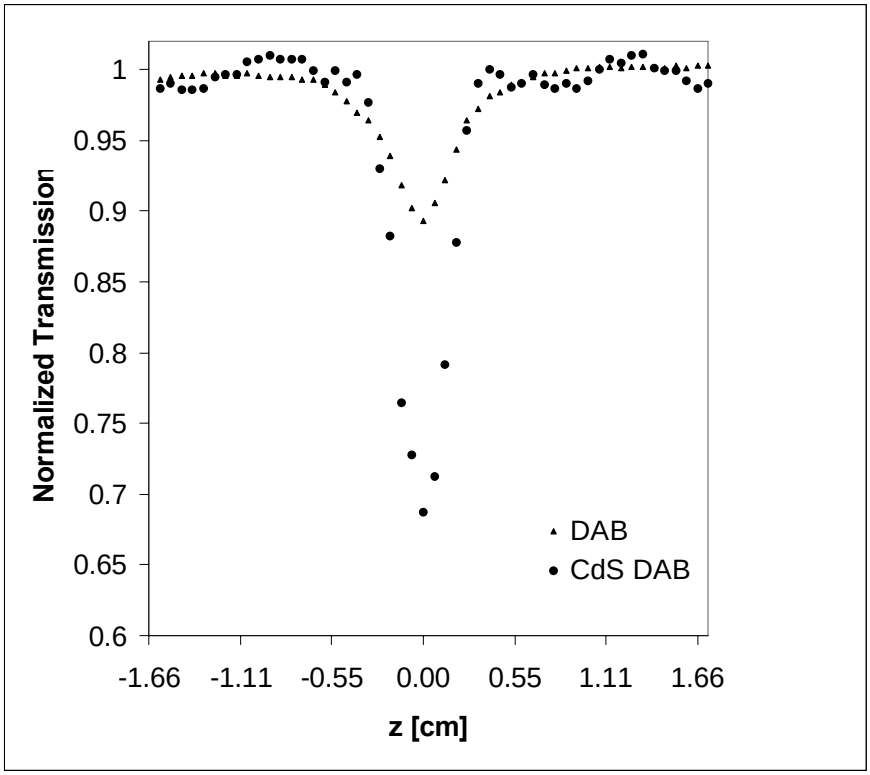

Fig. 5.9 The open aperture transmittance at 532 nm from a G5-DAB-QD sample and a pristine G5-DAB film

Z-scan measurements were also carried out at 355nm, in quasi-resonance with the lowest excitonic band at 330 nm, and at another nonresonant wavelength 1064nm. Open aperture measurements were also carried out at 1064 nm and gave values even smaller than at 532 nm (β ~20 cm/GW). The results of the picosecond Z-scan measurements are shown in Table 5.2. The first and second columns in Table II show the third order nonlinear susceptibility $\chi^{(3)}$ and the nonlinear refraction index n_2 of the pristine G5-DAB dendrimer for the three excitation wavelengths. The third and fourth column show $\chi^{(3)}$ and n_2 for the CdS-G5 DAB QD sample.

Wavelength (nm)	*χ (3) G5-DAB (esu)*	*n_2 G5-DAB (cm^2/GW)*	*χ (3) G5-DAB-QD (esu)*	*N_2 G5-DAB-QD (cm^2/GW)*
1064	3.9×10^{-10}	9.1×10^{-3}	-7.5×10^{-10}	-1.7×10^{-2}
532	5.8×10^{-10}	13×10^{-3}	-22×10^{-10}	-5.1×10^{-2}
355	-2.8×10^{-10}	-6.5×10^{-3}	-53×10^{-10}	-12.4×10^{-2}

Table 5.2. Summary of picosecond nonlinear susceptibility results

These results indicate relatively large values for the magnitude of the nonlinear coefficient ($|\chi^{(3)}| > 10^{-10}$ esu) for the pristine dendrimer and the composite at all investigated wavelengths. The pristine dendrimer nonlinear response coefficient is positive at 1064nm and 532 nm and negative at 355 nm. This sign reversal and the fact that the values are very close, strongly suggests that the 532nm and 355 nm excitations are in opposite sides of a two photon absorption band[39]. The G5-DAB-QD response is negative at all three wavelengths. The sign difference at 532 nm and 1064 nm suggests that the NLO response of the G5-DAB-QD is dominated by the QD exciton contribution to the nonlinear response through two photon resonance enhancement. The G5-DAB-QD shows a smaller response at 1064 nm compared to 532 nm and a significantly larger response at 355 nm. The enhanced response at 532 nm is expected since two-photon absorption is significantly stronger at that wavelength compared to 1064 nm. The 355 nm

wavelength is close to the QD exciton band and shows significant linear absorption and therefore resonance enhancement of the nonlinear response related to exciton bleaching effects. This was confirmed by open aperture Z-scan measurements, which at 355 nm exhibit the characteristic bleaching peak in lieu of the TPA dip displayed at the other wavelengths and shown in Fig.5.9. Furthermore, the good overlap in figure 5.10, between the linear absorption coefficient and the nonlinear susceptibility, confirms the hypothesis that the observed nonlinearity is strongly enhanced via single-photon resonance at 355 nm.

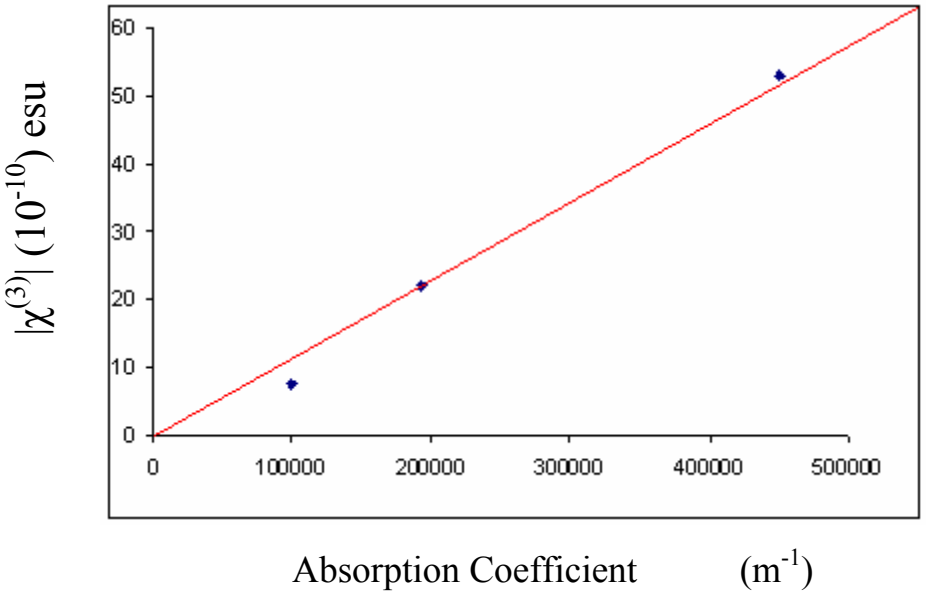

Fig. 5.10 Variation of the 3rd order nonlinear susceptibility $\chi^{(3)}$ versus the absorption coefficient α. Solid line shows the theoretical fit $\chi^{(3)} \sim \alpha$

Femtosecond results

Based on the same general principle, open and close aperture Zscans were performed on various Cadmium Sulfide quantum dots embedded in either G4 and G5 poly(propylene Imine) dendrimer or a G6 PAMOH dendrimer films using optical pulses of femtosecond duration. The films had an average thickness of ~ 400nm. The femtosecond system used has been described in *Section 2.1.1*. Throughout the experiments, the pulse duration was kept constant at about 130fs as illustrated by the autocorrelation trace in figure 5.11. The incident energy per pulse ranged from 0.2 μJ to about 2 μJ corresponding to a low end on-axis intensity of 150 GW/cm^2. The third-order nonlinear response of the samples was

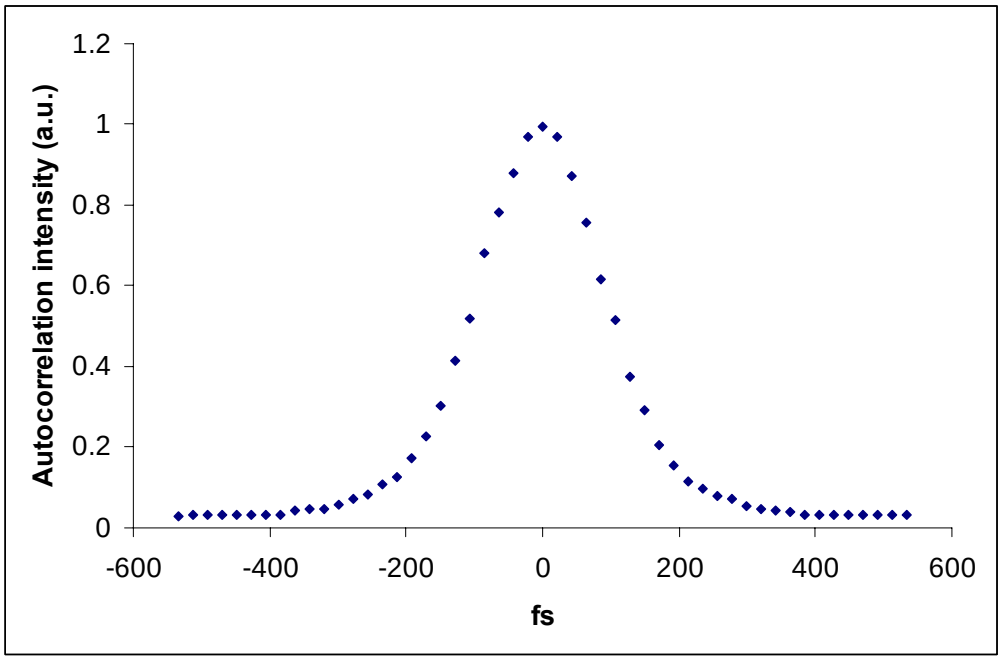

Fig. 5.11 Normalized autocorrelation trace of a 130 fs optical pulse

investigated at wavelengths both above and below the band gap. Absolute values of the magnitude of $\chi^{(3)}$ for the hybrid systems were obtained from the transmission measurements using:

$$\chi^{(3)}_{Sample} = \chi^{(3)}_{Quartz} * \left(\frac{\Delta T_{p-v} * n_0^2}{L_{Eff}}\right)_{Sample} * \left(\frac{L_{Eff}}{\Delta T_{p-v} * n_0^2}\right)_{Quartz} \qquad (5.11)$$

where ΔT_{p-v} represents the peak to valley difference in the transmission curve, and $\chi^{(3)}$ for silica glass was taken to be (2.0±0.5)*10^{-14} esu, at 800nm from reference[40].

The computed nonlinearities are illustrated in *Table 5.3* for both pristine and hybrid systems. Once again, the response of the reference films *(containing only the dendrimer)* showed positive nonlinearities in the transparent region, with a change in sign at wavelengths close to or above the band gap, while the response of the corresponding hybrid systems showed negative nonlinearity at almost all the wavelengths. In particular, the nonlinear response of the hybrid CdS-G4 and G5 DAB systems showed consistent self-defocusing *(negative)* behavior, while the response of the CdS-G6 PamOH system showed self-focusing *(positive)* nonlinearity at wavelengths in the transparent region with a change in sign for wavelengths close to the bandgap. Keeping in mind that the thicknesses of the films were very close in values, the discrepancy in the overall result has two probable explanations. First, it may mean that the concentration of the CdS-G6 film was considerably less than that of the other samples, resulting in a reduced response from the dots. Second, since the dot to dot spacing is expected to increase for a higher generation dendrimer *(Table 5.1)*, the overall nonlinear response of the dots due to dot to dot interaction should accordingly decrease, which seems to be the case for the G6-CdS sample.

Different other features characteristics of nanometer-size entities can be retrieved in *Table 5.3*. One very important observable feature is the consistent negative response of the dots for the G4 and the G5 samples, even in the transparent region at frequency ω smaller than any resonant frequencies. This trend is in accord with reported observation[41] of the behavior of $\chi^{(3)}$ in nanostructured materials of comparable sizes where the optical Stark effect is predominant. The optical or ac Stark effect is a third-order process which leads to an intensity dependent increase in the separation of the lower and upper levels and consequently to a diminished optical response in a material due to the resulting increase in the energy separation between the ground and excited states. This effect is

Wavelength (nm)	χ (3)**G4**-QD (esu)	χ (3)**G5**-QD (esu)	χ (3)**G6**-QD (esu)
	$*10^{-10}$	$*10^{-10}$	$*10^{-10}$
800	- (5 ± 1)	- (1.8 ± 1)	5.3 ± 1
660			8 ± 1
400	- (9.2 ± 1)	- (4.9 ± 1)	- (2.2 ± 1)
266	-(13 ± 1)	- (8.4± 1)	

Table 5.3. Summary of femtosecond nonlinear susceptibility results

favorable to single photon absorption *(SPA)* which contributes negatively to the overall nonlinearity of the system.

Investigation of the two-photon absorption *(TPA)* processes in the materials led to the conclusion that TPA processes were negligible in the transparent region with some appreciable enhancement at wavelengths closer to the absorption band edge as can be observed in figure 5.12. Although single photon absorption *(bleaching)* is expected at or near resonance, the excitation at 400nm is still below bandgap which explains the preponderance of TPA processes. Open aperture transmittance at wavelengths above the bandgap showed considerable single photon enhanced absorption. However, in order to

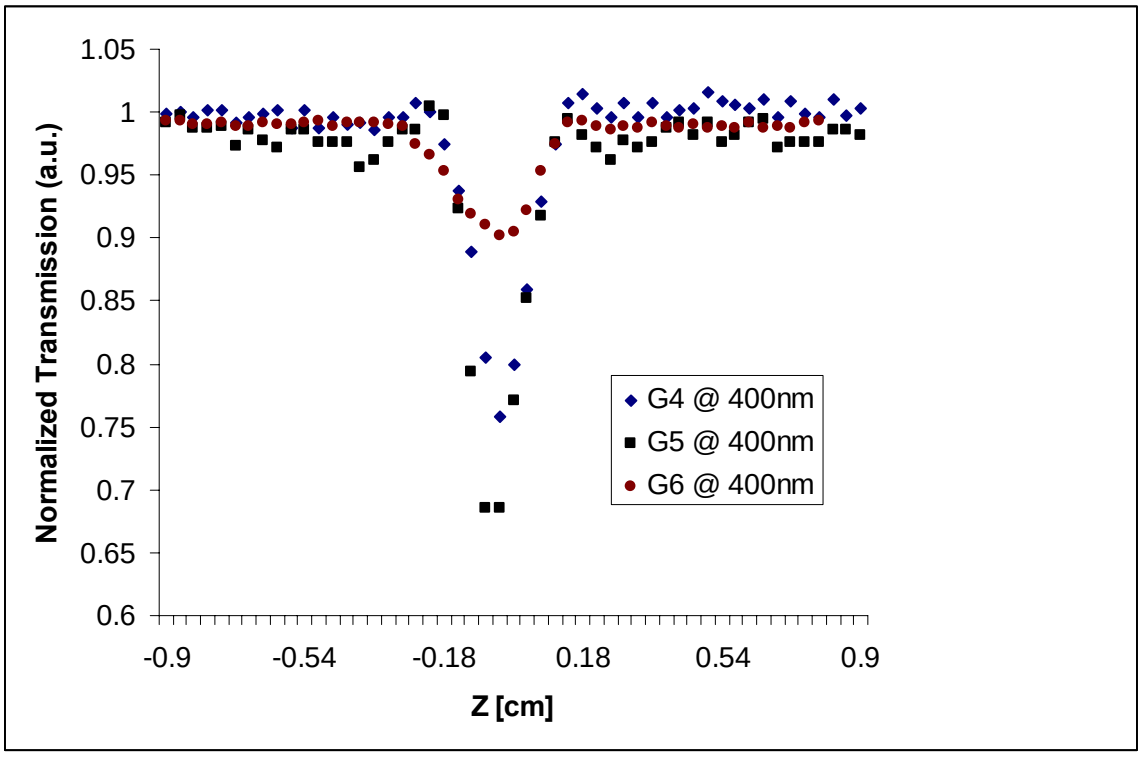

Fig. 5.12 Open aperture transmittance of the CdS-dendrimer hybrid systems at 400nm

compare with the picosecond data, we investigate once again the complex nature of the nonlinear susceptibilities by evaluating the TPA coefficients β at 400nm for all samples. Using *Equations 5.9, 2.12, 2.13 and 2.14* describing respectively the normalized transmittance without an aperture, the real and imaginary parts of the nonlinear

$$T(z) = \sum_{m=0}^{\infty} \frac{\left(\frac{-\beta I_o L_{eff}}{1 + z^2 / z_o^2} \right)^m}{(m+1)^{3/2}}, \tag{5.19}$$

$$\chi_R^{(3)} = 2n_0^2 \varepsilon_0 c n_2 (mks) \tag{2.12}$$

$$\chi_{\mathrm{Im}}^{(3)} = \frac{n_0^2 \varepsilon_0 c^2}{\omega} \beta \tag{2.13}$$

with

$$\beta = \frac{\Delta T \; 2\sqrt{2}}{I \frac{(1 - e^{-\alpha L})}{\alpha} (1 - r)} \tag{2.14}$$

	$\chi^{(3)}$ esu	β in cm/GW	Re[$\chi^{(3)}$]	Im($\chi^{(3)}$)
G4-CdS	- (9.2 ± 1) * 10^{-10}	107.1 * 10^{-2}	(-)6.9 * 10^{-10}	4.8 * 10^{-11}
G5-CdS	- (4.9 ± 1) * 10^{-10}	131.4 * 10^{-2}	(-)3.7* 10^{-10}	5 * 10^{-11}
G6-CdS	- (2.2 ± 1) * 10^{-10}	34.5 * 10^{-2}	(-)1.6* 10^{-10}	1.3 * 10^{-11}

Table 5.4 Nonlinear absorption and refraction properties as a function of sample Generation at 400nm

susceptibility and the two-photon absorption coefficient, a curve fit to the experimental data yielded two-photon absorption coefficient values of $\beta_{G5} = 131.4 * 10^{-2}$, $\beta_{G4} = 107.1 * 10^{-2}$ and $\beta_{G6} = 34.5 * 10^{-2}$ cm/GW. While we can affirm that the TPA coefficient of the G5-CdS sample is greater than that of the G4-CdS, we can not comment however on the β value of the G6-CdS sample since their dendritic constituent is different. Comparing the femtosecond and the picosecond β values of the G5-CdS sample, we notice that β_{G5} (fs) > β_{G5} (ps). Since TPA is an intensity dependent phenomenon, the TPA coefficient is expected to increase with the peak on-axis intensity, which is higher for femtosecond than for picosecond optical pulses.

It is worth noting here that a comparison of the nonlinearities obtained from both femtosecond (*fs*) and picosecond (*ps*) pulses shows yet another interesting phenomenon. As can be seen from Table 5.3 and 5.4, the femtosecond data for the pristine dendrimer are quite close to the picosecond data when the experimental error is taken into account, while there is a substantial difference between femtosecond and picosecond results for the G5-DAB-QD samples. Figure 5.13 shows a plot comparing the value of nonlinear susceptibilities in the same G5 DAB QD sample for femtosecond and picosecond excitations. The response to picosecond pulses at 1.06μm is about 4 times larger than the response to 120 fs pulses at 800nm while at 350-400 nm the long pulse response is more than one order of magnitude larger.

Resonance enhancement is an important factor in the nonlinear optical response of a material. In the transparent region, away from resonance, the nonlinearity is a result of bound carriers in the valence band and is generally expected to be independent of pulse

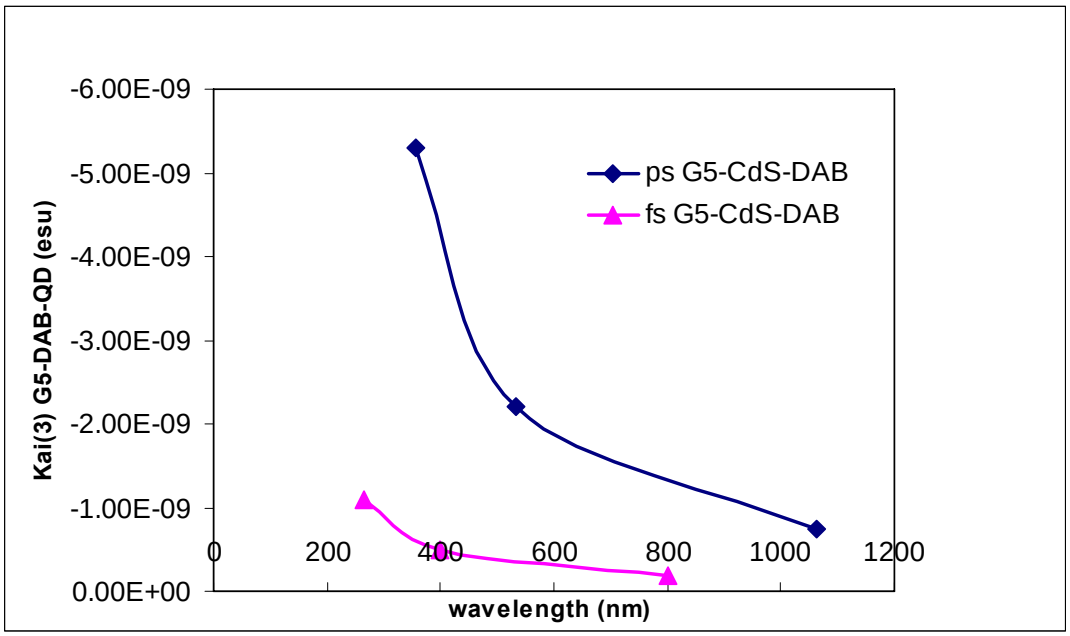

Fig 5.13 Picosecond and femtosecond response of the CdS-G5 sample

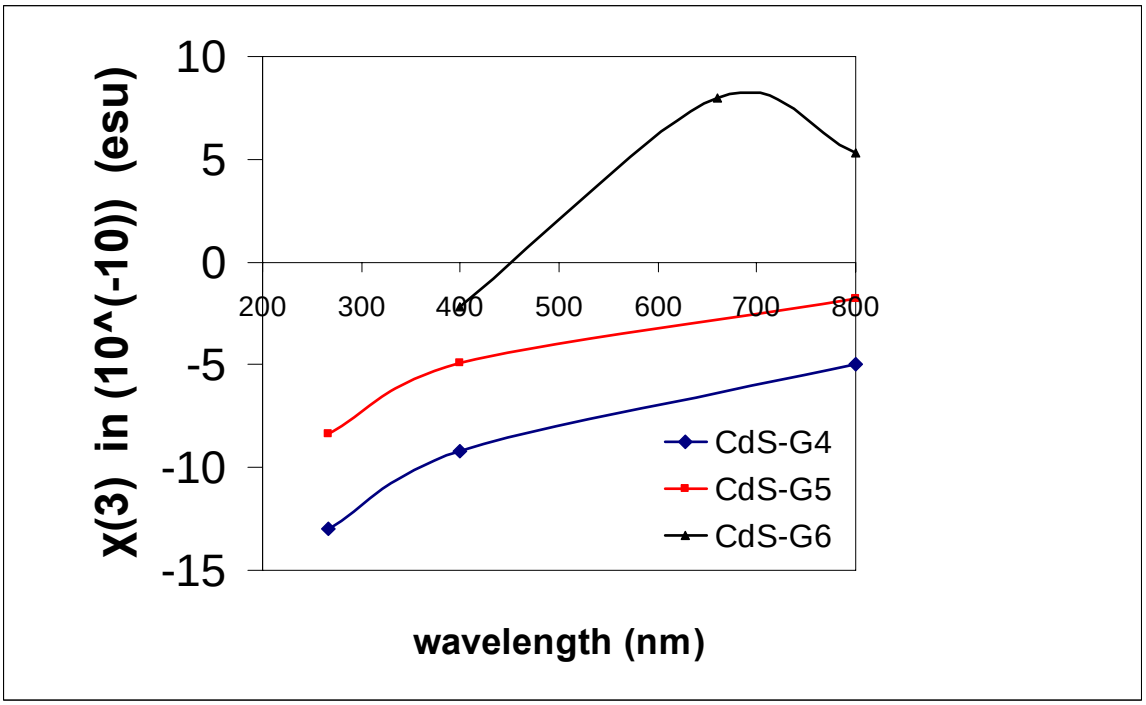

Fig. 5.14 Variation of the nonlinear response in the femtosecond regime

duration. At and near resonance, the nonlinearity is due to contributions of both bound carriers and free-carriers in the conduction band, whose density depends on pulse duration and carrier lifetimes in the excited states. For the common situation in which the laser pulse duration is shorter than the material response time τ_R, the conduction band carrier density is a function of the excitation pulse duration. The free carrier contribution to the nonlinear response is then also a function of pulse duration. When the excitation wavelength is long enough that we are away from resonance, the contribution from free carriers is expected to weaken and the difference in nonlinear optical responses between *ps* and *fs* pulses should shrink. This proposition seems to be supported by the measurements shown in figure 5.13, where clearly the gap between susceptibility values for picosecond and femtosecond pulses increases with shorter excitation wavelength. The resonance (imaginary) contribution to the nonlinear response is inversely proportional to the saturation intensity[42] (I_s) : $\chi^{(3)} \sim 1/I_s$. If the excitation pulse is shorter than the lifetime of the excited state then the single photon absorption saturation is determined by the saturation fluence E_{sat}, given by $E_{sat} = \frac{h\nu}{\sigma}$, where σ is the absorption cross section [43]. As expected, reasonable estimates of E_{sat} for the current sample yield values above the femtosecond fluence ($E_{fs} \approx 10^{-3}$ J/ cm^2) and below the picosecond fluence ($E_{ps} \approx 10^{-2}$ J/cm^2). This seems to confirm that the difference in the nonlinear response is related to the difference in the contribution of free carriers to the nonlinear response.

5.5. Conclusion

We have measured the third-order nonlinear susceptibility $\chi^{(3)}$ and the nonlinear optical absorption coefficient β of a number of small CdS quantum dots inside different dendritic matrices, using picosecond and femtosecond optical pulses. Results in the picosecond study showed that the pristine dendrimer had $\chi^{(3)}$nonlinearities in the 10^{-10} esu range as the nonlinearity changed in sign with wavelength while the dendrimer-semiconductor composites had negative nonlinearities up to -5 x 10^{-9} esu. In the femtosecond regime, the nonlinearities were found to depend on the *dot-to-dot* spacing and the excitation frequency, with nonlinearities ranging from (+8 to -13) x 10^{-10} esu. These values are among the highest off-resonance nonlinearities reported for organic and/or hybrid composites materials. Variation of the nonlinear response as a function of laser pulse duration suggests that the first excited state has a lifetime smaller than 30 ps. However, those results showed no evidence of NLO enhancement that can be attributed to dendrimer-QD interactions. In addition, in all the samples, the two-photon absorption was low (< 150 cm/GW) compared to similar materials. For the CdS-G5 sample, the high nonlinearity and low two-photon absorption gives a figure of merit of less than 10^{-3} at 532 and 1064 nm. The measured nonlinearities are probably still too low for practical applications. It is however possible to further enhance the nonlinear response of these systems. The nonlinear response of hybrid semiconductor-dendrimer nanocomposites is a function of the interacting materials, the dot size and the dot-to-dot spacing [2]. Further investigations need to be performed with nanocontainers that will allow a smaller dot to dot spacing and a better coupling or excitonic interaction.

References:

1. V. Klimov; P. Haring Bolivar; H. Kurz, *Phys. Rev*. B **53**, 1463 (**1996**).
2. A. L. Efros and A. Efros, *Sov. Phys. Semicond*. 16 772 (**1982**).
3. L. Brus*, J. Chem. Phys*. 79, 5566 (**1983**).
4. L. Brus, *Appl. Phys*. A 53, 465 (**1991**).
5. A. Alivisatos, *Science* 271, 933 (**1996**).
6. L. Balogh; D.R. Swanson; R. Spindler; D.A. Tomalia, *Proc. ACS PMSE* **1997**, 77, 118.
7. Gao, Y., Huong, N. Q., Birman, J. L.,Potasek, M. J., Large nonlinear optical properties of semiconductor quantum dot arrays embedded in an organic medium. *Journal of Applied Physics*, 96, 4839 (**2004**).
8. R.G. Ispasoiu; L. Balogh; O.P. Varnavski; D.A. Tomalia; T. Goodson III, *J. Amer. Chem. Soc.* **2000**, 122, 44.
9. Nguyen Que Huong and Joseph Birman, "Quantum dot lattice embedded in an organic medium: Hybrid exciton state and optical response," *Physical review B*, 61,13131, (**2000**)
10. Robert E. Schwerzel, Kevin B. Spahr, John P. Kurmer, Van E. Wood, Jerry A. Jenkins, *J. Phys. Chem.,* 102, 5622 (1998)
11. Edwin F. Hilinski, Patricia A. Lucas, Ying Wang, "A picosecond bleaching study of quantum confined cadmium sulfide microcrystallites in a polymer film," *J. Chem. Phys*., 89, 3435 (**1988**)

12. J. He, W. Ji, G. H. Ma, S. H. Tang, H. I. Elim, W. X. Sun, Z. H. Zhang, W. S. Chin, "Excitonic nonlinear absorption in CdS nanocrystals studied using Z-scan technique," *Journal of Applied Physics*, 95, 6381 (**2004**).
13. H. Du, G. Q. Xu, W. S. Chin, L. Huang, W. Ji, " Synthesis, characterization, and nonlinear optical properties of hybridized CdS-polystyrene nanocomposites," *Chem. Mater*., 14, 4473 (2002)
14. Alex Adronov, Jean M. J. Frechet, Guang S. He, Kyoung-Soo Kim, Sung-Jae Chung, Jacek Swiatkiewicz, Paras N. Prasad, " Novel two-photon absorbing dendritic structures," *Chem. Mater*., 12, 2838 (2000)
15. Y. Gaoa, N. Q. Huong, J.L. Birman, M. J. Potasek, "Highly effective thin film optical filter constructed of semiconductor quantum dot 3D arrays in an organic host," *Nanofabrication: Technologies, Devices, and Applications*, W. Y. Lai and S. Pau, eds, Proc. SPIE, vol. 5592, in press.
16. C. L. Tang, *Fundamentals of Quantum mechanics*, (2005)
17. Hari Singh Nalwa, *Nanostructured Materials and Nanotechnology*, Academic Press (2002). Charles Kittel, *Introduction to Solid States Physics*, John Wiley & Sons (2005)
18. Abramowitz and Stegun, *Handbook of Mathematical Functions*, (1965)
19. Buhleier, E. W.; Wehner, W.; Vo¨gtle, F. *Synthesis* **1978**, 155- 158.
20. Denkewalter, R. G.; Kolc, J.; Lukasavage, W. J. U.S. Pat. 4,- 289,872, Sept. 15, 1981.
21. (4) Denkewalter, R. G.; Kolc, J.; Lukasavage, W. J. U.S. Pat. 4,- 410,688, Oct. 18, 1983

22. A.W. Bosman, H. M. Janssen, and E. W. Meijer, "About dendrimers: Structure, Physical Properties, and applications," *Chem. Rev*., 99, 1665 (1999)

23. Hong Ma and Alex K.-Y. Jen, "Functional dendrimers for nonlinear optics," *Adv. Mater.,* 13, 1201 (2001)

24. Bai Jaeil, Ducharme Stephen, Leonov Alexei G., Lu Liu, Takacs James M., "New organic photorefractive material composed of a charge-transporting dendrimer and a stilbene chromophore," *Proc. SPIE* Vol. 3799, 22 (1999)

25. Shiyoshi Yokoyama, Tatsuo Nakahama, Akira Otomo, and Shinro Mashiko, "Intermolecular Coupling Enhancement of the Molecular Hyperpolarizability in Multichromophoric Dipolar Dendrons," *J. Am. Chem. Soc*., 122, 3174 (2000)

26. T. Goodson III, O. Varnavski and Y . Wang, "Optical properties and applications of dendrimer-metal nanocomposites," *Int. Reviews in Physical Chemistry*, 23, 109 (2004)

27. V. I. Yudson, P. Reineker, and V. M. Agranovich, *Phys. Rev. B* **52**, R5543 ~1995

28. T. Takagahara, Solid State Commun. **78**, 279 ~1991; Surf. Sci. **267**, 310 ~1992; T. Takagahara and E. Hanamura, *Phys. Rev. Lett.* **56**, 2533 ~1986.

29. A. Engelmann, V. I. Yudson, and P. Reineker, *Phys. Rev. B* **57**, 1784 ~1998

30. V. M. Agranovich, D. M. Basko, G. C. La Rocca, and F. Bassani, *J. Phys.: Condens. Matter.* **10**, 9369 (1998)

31. V M Agranovich, G C La Rocca and F Bassani, *Pure Appl. Opt.* **7** (1998) 119–127

32. 11) L. V. Asryan and R. A. Suris, *IEEE J. Quantum Electron*. **34**, 841 ~1998

33. Y. Gao, N. Q. Huong, J.L. Birman, M. J. Potasek, *Proc. SPIE*, **5592**, 272, (2005).

34. Information obtained from Dendritic Nanotechnologies

35. L.E. Brus, *J. of Chem Phys.* **80**, 4423 (1984)

36. Hong Ma and Alex K.-Y. Jen, *Adv. Mater*., **13**, 1201 (2001)

37. M. Sheik-bahae, A.A. Said, E. W. Van Stryland, *Opt. Letters*, **14**, 955 (1989)

38. Ardie Walser, Stavros G. Demos, Michael Etienne, Roger Dorsinville, *Optics Communications*, **240**, 417 (2004)

39. Lina Yang, R. Dorsinville, R. R. Alfano, W. K. Zou, N. L. Yang, *Optics Letters*, **16**, 758 (1991)

40. R. H. Stolen and C. Lin, *Phys. Rev. A* **17**, 1448 (1978)

41. D. Cotter, M.G. Burt, and J. Manning, *Phys. Rev. Let.*, **68**, 8 (1992)

42. Lina Yang, R. Dorsinville, Q. Z. Yang, P.X. Ye, R. R. Alfano, R. Zamboni, C. Taliani. Optics Letters, 17, 323 (1992).

43. Ursula Keller, K. J. Weingarten, Franz X. Kartner, D. Kopf, B. Braun, I. D. Jung, R. Fluck, H. Honninger, N. Matuschek, J. Aus der Au. IEEE J. of Selected Topics in QE, 2, 435 (1996)

Chapter 6

Nonlinear optical characterization of nanostructures with carbon nanotubes

6.1. Introduction

During the past decades, the scientific community has been racing to provide an alternative to microelectronics and its inherent limitations. Since 1948, when the first transistor was fabricated[1], the size of lithographic features has been constantly decreasing, as predicted by Moore's law. However, semiconductor based microelectronics are well on the way of reaching the limit of electronic miniaturization. In order to reach smaller dimensions, either new technologies for structuring materials must be developed or molecules with a diameter from 0.1-1 nm (atoms, atomic clusters) to a few nm (clusters, organic molecules, proteins, polymers, carbon nanotubes, DNA) must be used. Common scientific effort has been focused on developing new alternative technologies including nanoelectronics and molecular electronics. However, contingent to the development of nanoelectronics is the discovery of new suitable materials with the right physical, electrical and transport properties.

While a number of nanostructured materials are been considered as *the* representative for nanoelectronics, the perfect candidate is yet to be found. The aim of this chapter is to investigate the optical properties of a number of potentially useful nanosize materials that may become suitable for nanoelectronics or molecular electronics implementation.

6.2. Background

Among the materials being considered, single wall carbon nanotubes (SWCNT) have generated a lot of expectations, owing to their characteristic properties. Ever since the discovery of multi-walled nanotubes in 1991[2] and single walled in 1993[3], carbon nanotubes (CNT) have attracted enormous attention worldwide. Resembling tubes of rolled-up graphite about a nanometer in diameter and several micrometers or more long, these structures present all the characteristics mentioned above and additionally are mechanically exceptionally strong, with a unique one-dimensional *p*-electron conjugation, and high thermal and chemical stability. Furthermore, the CNT molecules come in two varieties, semiconducting and metallic, depending on the exact details of their structure. The classical construction of CNT is illustrated in Figure 6.1[4]. In this figure, the vector **OA** connects two equivalent points on a graphene sheet. Similarly, parallel vectors **OB** and **AB'** can be obtained and the resulting strip of graphene can be rolled into a tube. The unit cell of the tube is then specified by **OA** called the chiral vector $\mathbf{C_h}$, while **T** is the lattice vector, defined by the first intersection along **OB** with a point of the graphene lattice. Figure 6.2 illustrates a physical representation of the three possible configurations of single wall carbon nanotube. An armchair (metallic) nanotube with a chirality angle of 0˚ degree is illustrated in a), in b) a zig-zag (metallic) nanotube with a chirality angle of 30˚ degrees is represented. c) shows a semiconductor nanotube with chirality between 0˚ and 30˚ degrees.

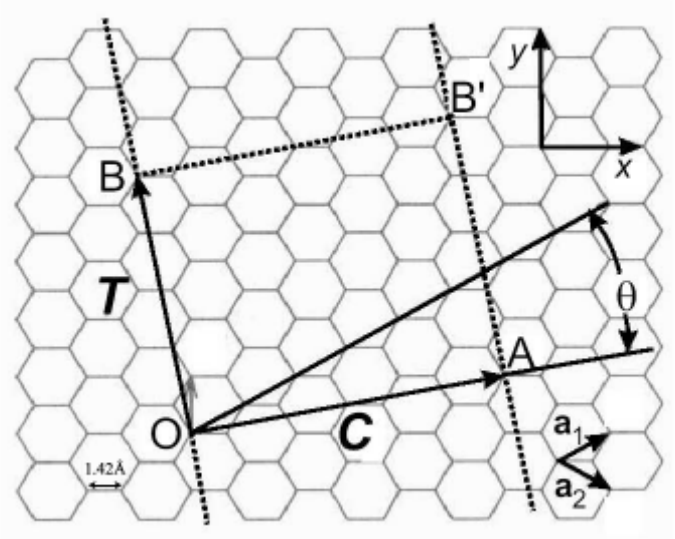

Fig. 6.1[4] Classical construction of a nanotube structure.

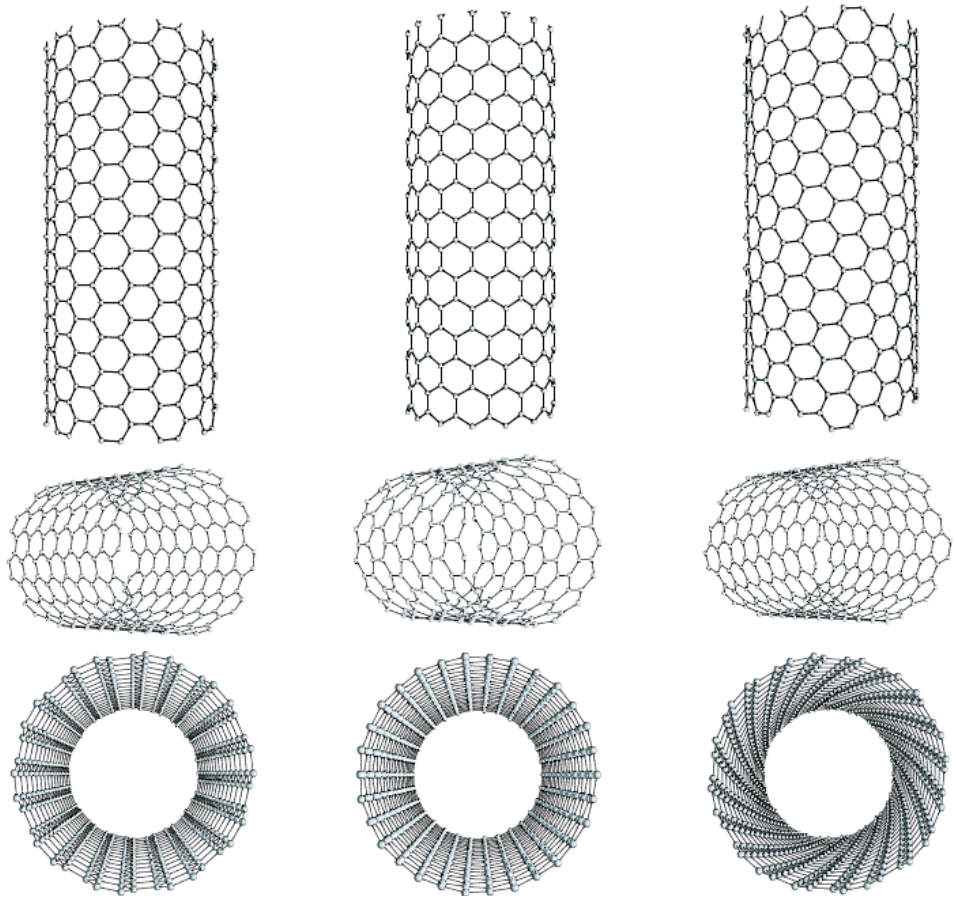

a) **b)** **c)**

Fig. 6.2. [5] a) armchair (metallic) b) zig-zag (metallic) and c) a semiconductor nanotube.

6.2.1 *1-D* Transport in SWNT

In general, the bandstructure of SWNT can be derived from that of graphene[5]. In its simplest state, the carbon atom has four electrons occupying the valence orbitals and is in the state $2s^2 2p^2$, but as the energies of these states lie close compared to energy of chemical bonds, it is possible to mix these states to form bonds to other atoms. In the case of graphene, the bonds formed between the carbon atoms are sp^2 bonds, i.e. the bonding orbitals are constructed from a mixing (hybridization) of one *2s* and two *2p* orbitals. This leaves one electron in a $2p_z$ orbital, which is often referred to as the π-orbital. The unit cell of graphene has two carbon atoms, each with three nearest neighbors. Each unit cell has therefore two electrons in π-orbitals. By imposing strictly periodic boundary conditions for translations of the roll-up vector that defines the nanotube, the bandstructure of a simple tube can be obtained. The allowed $\boldsymbol{k}$ values are then quantized in the direction perpendicular to the roll-up vector $\boldsymbol{R}$: $k \bullet R = 2n$, where n is an integer. Therefore, the band structure of nanotubes consists of 1-D subbands. In general, a nanotube will have a bandgap unless the lines of allowed $\boldsymbol{k}$ pass through two gapless point; for example, an (n,m) nanotube will have a bandgap unless $n-m = 3p$, where p is an integer[6]. In all other cases there will be an energy gap, which has been shown to be inversely proportional to the diameter of the nanotube. The possibility for nanotubes to act either as perfect conductors or semiconductors makes them a very special component in the development and subsequent application of molecular electronics. However repeated experiment[7-8] have confirmed that in spite of the good theoretical properties of nanotubes, their actual experimental performance lags and therefore it has been suggested that the use of nanotubes in any real application would require some form of matrix to disperse the tubes and allow the fabrication of films, coatings, suspensions, or solutions

of the matrix and nanotube composite material. Previously it has been shown that nanotubes can be held in suspension with the polymer poly(metaphenylenevinyleneco-2, 5-dioctyloxy-para-phenylenevinylene)[9] (PmPV). This has the added advantage of purifying the nanotube soot,[10] embedding the nanotubes in a polymer matrix that forms a stable dispersion over time, and that is easily fabricated into films, fibers, coatings, and other material forms commonly fabricated from polymers. Furthermore, the polymeric host can be chosen to be electrically conductive, a property that would enhance the overall transport properties on the actual tubes. It is towards this goal that a group of researchers at NJIT led by Prof. Haim Grebel embarked on the project of embedding nanotubes into a series of electrically conductive polymer (ECP) hosts, namely poly(-vinylcarbazole) (PVK), and PMMA. It is well known that these polymers' ability to conduct electricity comes from their conjugated π-bond system, which is formed by the overlapping of carbon *p* orbital and alternating carbon-carbon bond lengths. This conjugated double bonding permits easy electron mobility throughout the whole molecule due to delocalization of the electrons. In spite of these well known characteristics, practical uses of free-standing conducting polymers are not very likely because of their poor mechanical properties (such as strength and processability) that rarely meet industrial requirements. It is expected that the newly engineered material resulting from the hybridization of these two systems will overcome the weakness of the constituents. This part of the thesis will concern with the nonlinear transmission properties of a SWNT-PCz sample. For the electrical properties of this material, we refer the reader to [11].

6.2.2. Quantum effects and Optical Properties of SWNT

Due to their low-dimension, nanotubes are essentially quantum structures, governed by the laws of quantum mechanics. Two important quantum effects take place in SWNT that will dominate all transport measurements. The first effect is due to the wave nature of the electron and thus phase coherence ($l_\Phi > L$), while the second effect is a consequence of the finite size of the electronic charge e. Both effects require small systems to be observed and scale as $1/L$, where L is the length of the tube. Phase coherence in SWNT gives rise to another quantum effect known as *size quantization*. Instead of having a continuum of states inside the SWCNT, the continuum becomes quantized in discrete levels separated by ΔE[12]. The underlying assumption for size quantization to happen is that the electron can travel phase coherently in the region[13]. The importance of phase coherence is clearly revealed considering that part of an electron wave in the SWCNT is reflected at the interfaces and will interfere with itself. This sets up resonances (also called bound states or levels). The immediate effects of these discrete levels in the density of states can be seen in the absorption peaks shifting to higher energy side with decreasing tubes diameters[14]. Nanotubes have been shown to have fast nonlinear optical properties and it has been suggested that the combination of strong optical confinement with large dispersion of the structure can be useful for nonlinear, ultrashort pulse control[15].

In the past few years, there has been a mounting interest in periodic structures embedded with nonlinear materials such as Si or Ge nanoclusters. For example, Vijayalakshmi et al[16] have studied the nonlinear dispersion properties of opaline structures doped with Si

nanoclusters. In this study, pulse compression and pulse broadening were rendered possible through *transverse Bragg confinement*[17]. An opaline structure is essentially a three-dimensional (3D) periodic structure (photonic crystal) made of ordered array of silica spheres (see Fig. 6.3 below). Such structures are particularly attractive since they offer strong confinement of optical beams. Confinement of a photon within 3-D periodic structures provides an environment for photon localization. The propagating wave-vector is at resonance with the periodicity of the structure in all directions. Large Mie scattering from every element of the array, the spheres of Fig. 6.3, causes a broadening effect and the periodic structure acts as a grating. Unlike a simple phase grating, a large pulse shaping effect occurs when the Mie scattering effect is in coherence with the Bragg reflection condition.

There have been reports of optical limiting[18], optical switching, and angle-dependent transmission[15] behaviors in Opal-nanotubes composites. In this thesis, we use open and close aperture Zscan and nonlinear transmission spectroscopy techniques to investigate the nonlinear optical properties of a hybrid system made of SWNT embedded inside a silica matrix as illustrated in *Figure 6.4*.

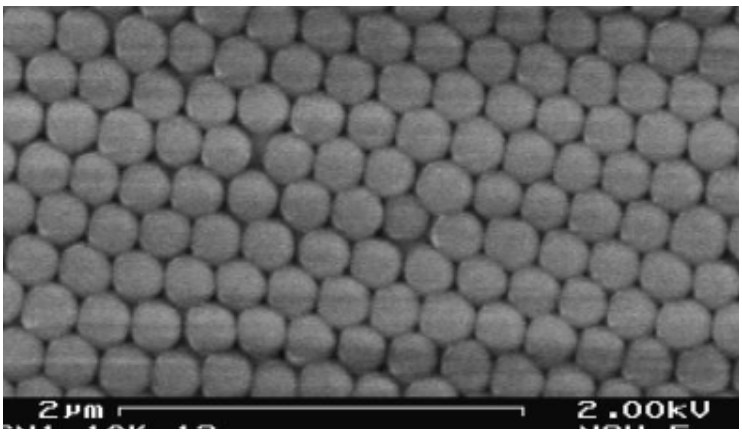

Fig.6.3. SEM picture of an opaline structure. Opal size: 250nm

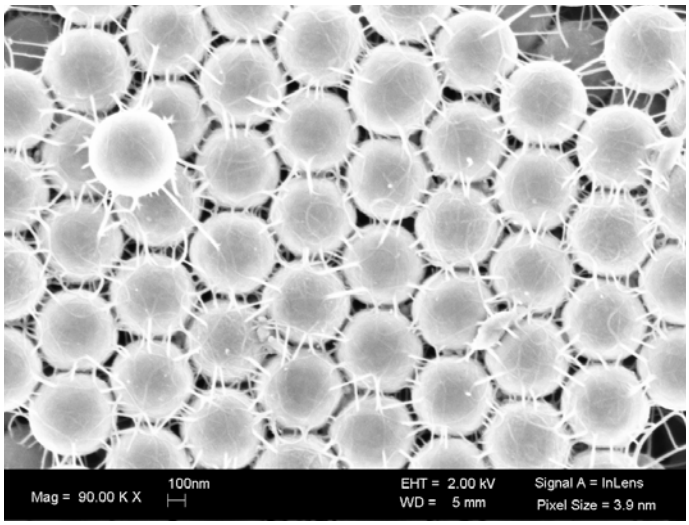

Fig. 6.4 SEM picture of SWCNTs within the opaline structure

6.3. Material preparation

The different samples studied in this chapter were prepared by Prof. H. Grebel's group at NJIT[11]. In the past, composites films were obtained by spin-casting a mixture of carbon nanotubes (CNT) with conductive polymer in solution[19-24]. However it was shown that this approach leads to a partial contact between ECP and some of the tubes, leaving dangling tubes and incomplete junctions. In order to ensure total contact and maximum interaction between the opaline structure, the tubes and the ECP, the conductive polymer (polycarbazole or, PCz) was deposited using electrochemical methods thereby, achieving an intimate contact between the SWCNT and polymer[25]. The steps involved in this process are illustrated in figure 6.5. The structures are based on either opaline or inverse opaline matrices. First, the opaline structure, Fig. 6.5 (a), was obtained by self-assembly of silica spheres. Then, SWCNT was grown within opaline structure, Fig. 6.5 (b), by the well-known Chemical Vapor deposition (CVD) procedure. The synthesized individual and small bundled SWCNT formed continuous contact from the bottom to the top of the film and laterally, through tube-tube interaction. This continuity created a macro-electrode for the electrochemical deposition of PCz polymer. At this point, a polymeric solution fills the voids of the structure. The silica template is either removed by etching with an acid to create the inverse structures, or the polymerization process ensures. The electrochemical experiments using three and two electrodes configurations were performed for polymerizing carbazole monomer[11]. A 273 EG&G Princeton Applied Research potentiosat-galvanostat was used to conduct the electrochemical polymerization in this three-electrode cell. The two-electrode experiment was conducted using an Oriel power source (model 70705). The SWCNT within opaline structure was used as the

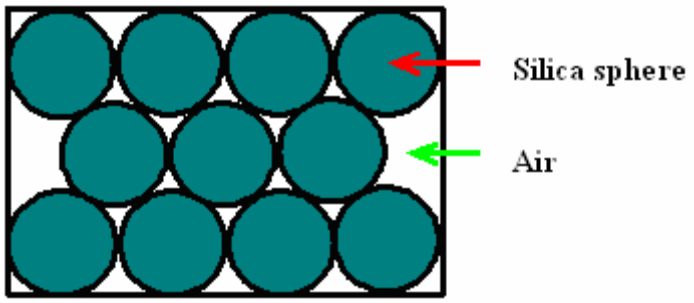

(a)

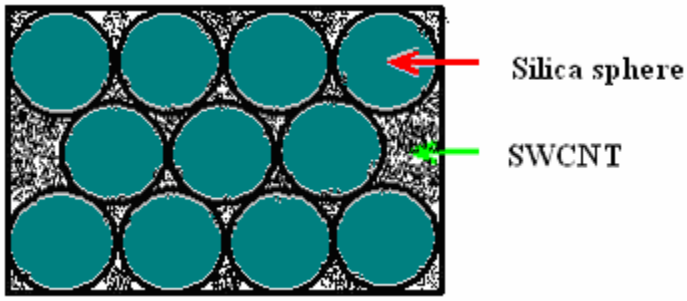

(b)

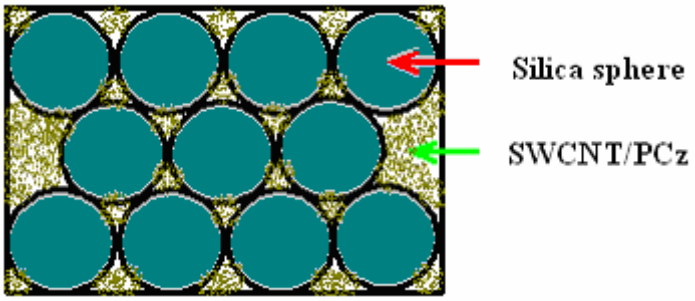

(c)

Fig. 6.5 Schematic illustration of the fabrication process of SWCNT/PCz nanostructure. (a) Opaline structure; (b) SWCNT within the opaline structure; (c) SWCNT/PCz within the opaline silica structure. The colors are for illustration purposes only and do not correspond to the real space distribution.

anode electrode while stainless steel foil served as the cathode electrode. The polymerization solution consisted of 0.02 M carbazole monomer and 0.2 M tetrabutylammonium tetrafluoroborate ($TBABF_4$) in acetonitrile. All chemicals were purchased from Aldrich chemicals and used without further purification. The potential applied for the polymerization of carbazole in this setup was around 30V. PCz electrochemically polymerized by three electrodes configuration on conducting glass was only used to compare and characterize the PCz prepared by two electrodes method by using SWCNT as electrode, Fig. 6.5 (c). The end products obtained through this process were: inverse structure composed of SWNT embedded in poly-(methyl methacrylate) (PMMA), SWNT within opaline silica structure, PCz/SWNT within opaline matrix, and a distributed three-dimensional p-n junction composed of p- and n-doped SWNT.

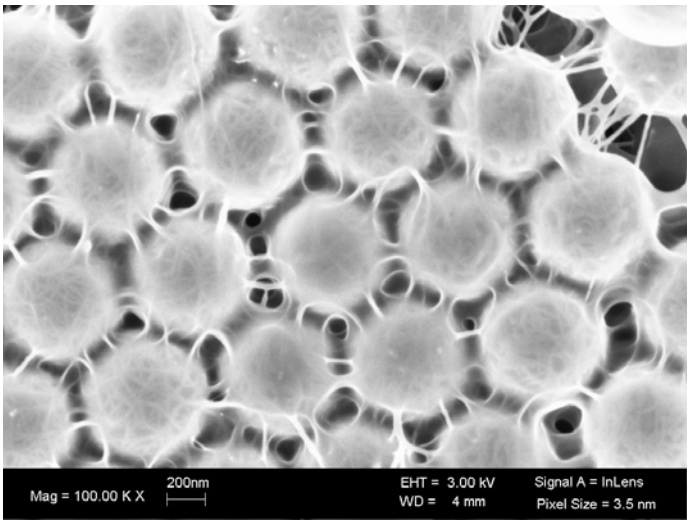

Fig. 6.6 Illustration of the electrochemical polymerization of carbazole. SWCNT/PCz within the opaline structure.

6.4 Experimental techniques and Results

The nonlinear optical properties of the samples were investigated based on their nonlinear transmission characteristics and their third-order nonlinear susceptibilities. The experimental setup used for transmission measurements is similar to the one described in *Chapter 3*, while the Zscan setup is similar to the one described in *Chapter 5*. Three different regimes were used to probe the nonlinearities of the samples: the inverse PMMA photonic crystal and a SWCNT/PVK+DEH were probed using nanosecond optical pulses at 532nm; picosecond transmission measurement was applied to the Opal, Opal/ SWCNT and PCz/SWCNT at both 532nm and 1.064μm; and finally 800nm femtosecond Zscan measurement was used in order to determine the third order nonlinear susceptibility of the Opal/CNT sample.

6.4.1 Nanosecond results

The nonlinear transmission of SWCNT in regular opaline structures has been demonstrated before[15]. It portrays angle dependent, nonlinear transmission. At peak transmission the nonlinear curve exhibits a step-like function. Unlike silica-based structures, the inverse ones were made of polymers and therefore, the nonlinear behavior, if any, of the polymeric matrix alone needs to be addressed. The nonlinear response of inverse structures, taken with 10 ns Nd:YAG laser at λ=532 nm, is shown in *Fig. 6.7*. Shown are the transmission curves of the inverse structure with and without the embedded SWCNT. The inset shows the nonlinear transmission of SWCNT which is the ratio of the corresponding best-fit curves. The SWCNT based inverse structures; thus, portray significant nonlinear absorption at low intensity values. Reference curves taken without the sample were linear within the range of the experiment, excluding any possible effects related to detector response.

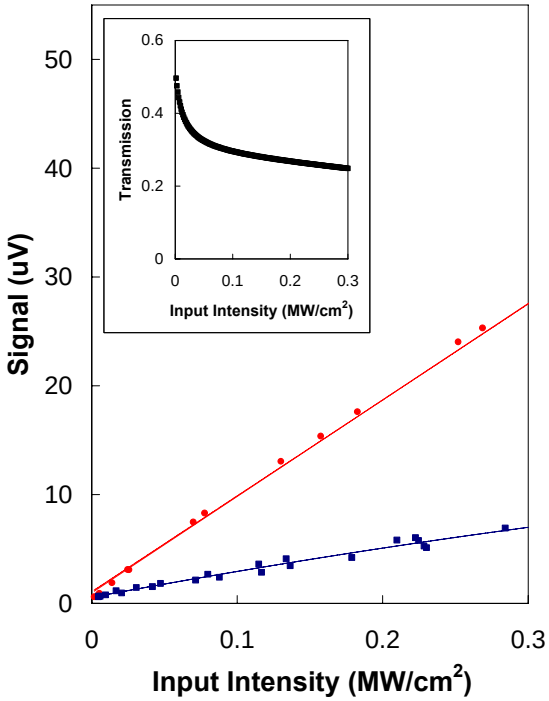

Fig. 6.7 Output (in μV – the detector reading) as a function of input peak intensity for inverse PMMA photonic crystal without (upper curve) and with SWCNT (lower curve). The inset shows the transmission of the latter (the ratio between the corresponding best-fit curves). The laser was 10 ns Nd:YAG at λ=532 nm.

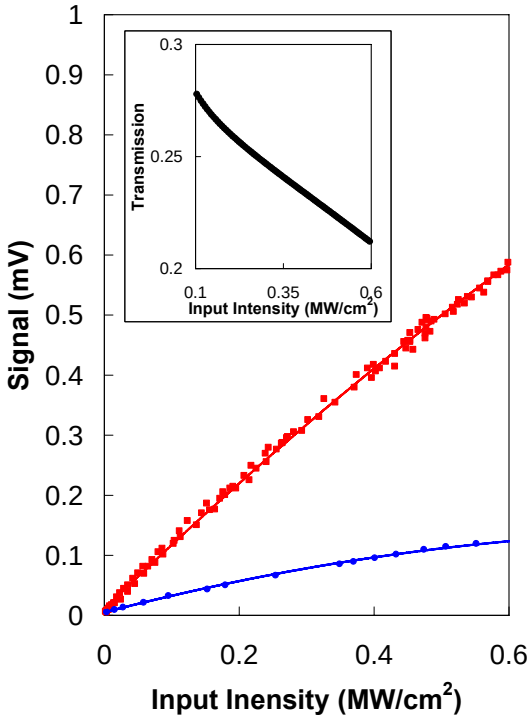

Fig. 6.8 Output (in mV – the detector reading) as a function of input peak intensity for regular silica based photonic crystal without (upper curve) and with PVK+DEH, SWCNT (lower curve). The inset shows the transmission of the latter (the ratio between the corresponding best-fit curves). The laser was 10 ns Nd:YAG at λ=532 nm.

Nonlinear transmission characteristics of another opaline structure made of SWCNT in its voids coated with poly(N-vinyl carbazole) (PVK) and an absorption additive, 4-(diethylamino)benzaldehyde diphenylhydrazone (DEH) in order to increase its absorption range, is shown in Fig. 6.8.

The polymer was introduced into the SWCNT grown voids as a solution. We used the 10 ns Nd:YAG laser at λ=532 nm to characterize the film. The PVK-DEH composition is well known for its photorefractive effect[26] at msec time scales. In the past, we used quantum dots of Si inside the silica opaline structure to induce nonlinear refraction effect at femtosecond time scale[27]. Here, we assess the nonlinear absorption of such composites to find a noticeable nonlinear absorption. This nonlinear absorption may be attributed to charge transfer between the SWCNT and the PVK at visible spectral range.

6.4.2 Picosecond results

Transmission data, taken with the 25 ps Nd:YAG laser at λ=532 nm, are shown in Fig. 6.9. The SWCNT exhibited a small bleaching effect. Such bleaching effects were also corroborated by open aperture z-scan measurements (although using much larger intensity levels) and points to saturation of the transition via band-filling or, depletion of the ground state. The composite of PCz coated SWCNT also exhibited an overall bleaching with a step-like saturation around peak power of 800 MW/cm^2. The step-like behavior is explained here by charge-transfer mechanism across the SWCNT/PCz interface. These measurements indirectly rule out possible thermal effects, which might have existed in our measurements with the 10 ns Nd:YAG laser. The response of only PCz films at this wavelength was linear.

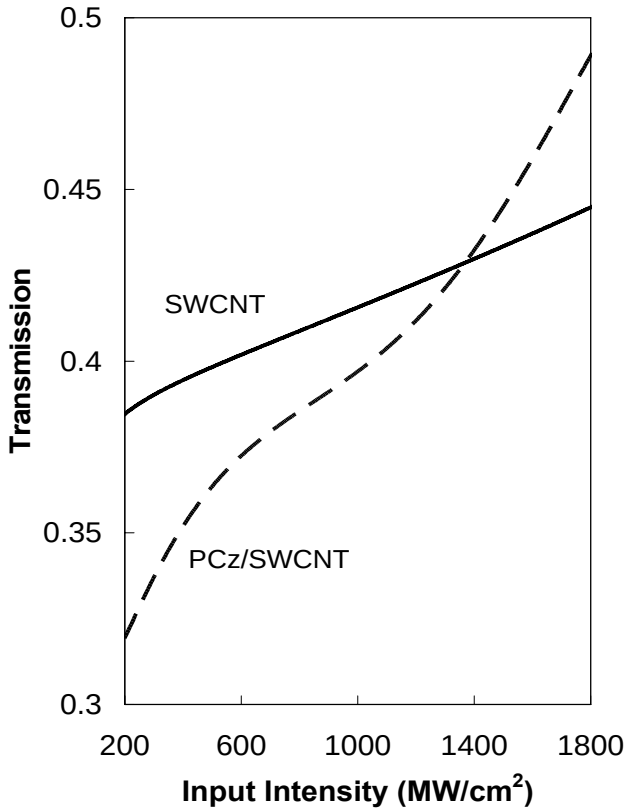

Fig. 6.9 Nonlinear transmission of SWCNT within the voids of synthetic opal (photonic crystal) taken with 25 ps Nd:YAG laser at λ=532 nm. The curves were normalized to transmission data for only opaline structure.

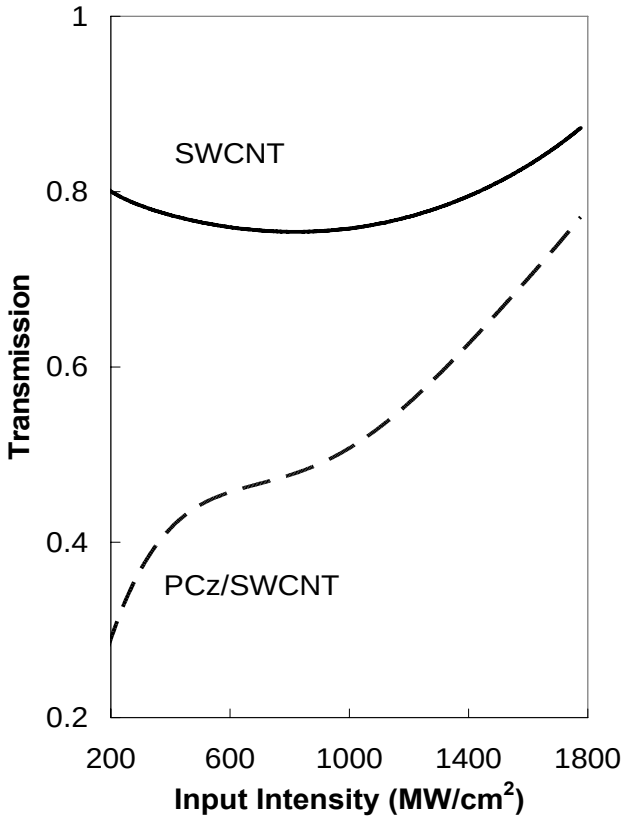

Fig. 6.10 Nonlinear transmission of SWCNT within the voids of synthetic opal (photonic crystal) taken with 25 ps Nd:YAG laser at λ=1064nm. The curves were normalized to transmission data for only opaline structure.

Transmission data taken at λ=1064 nm indicated a small nonlinear absorption for only SWCNT and a step like behavior, as shown in *Fig. 6.10*. The step-like characteristic is more pronounced here than the corresponding one at λ=532 nm and is exhibited at lower intensity values (around 600 MW/cm^2). The overall transmission values are almost double the corresponding values of the 532 nm experiments. Again, this effect may be attributed to charge-transfer across the PCz/SWCNT interface.

6.4.3 Femtosecond results

Single beam Zscan technique was used to investigate the nonlinear refractive index n_2 and the nonlinear absorption coefficient β of the Opal-SWCNT sample. The femtosecond laser system has been described in *Section 2.1.1*. The 800nm Gaussian laser beam was kept at constant pulse duration of 130 fs and used in a tight focus limiting geometry. The energy per pulse ranged between 0.3 and 0.8 μJ, and the beam waist at the focus was typically 55μm.

Figure 6.11 illustrates the linear absorption spectrum of the Opal-SWCNT sample. The curve reveals a small absorption onset at 800nm, however no absorption was observed in the infrared region. By subtracting the contribution from the opaline structure, the response of the SWCNT alone could be obtained as illustrated in fig 6.12. It is obvious that the small absorption onset observed at 800nm is due to the presence of the SWCNT structure, and therefore any observed nonlinearity at 800nm should be attributed to the SWCNT.

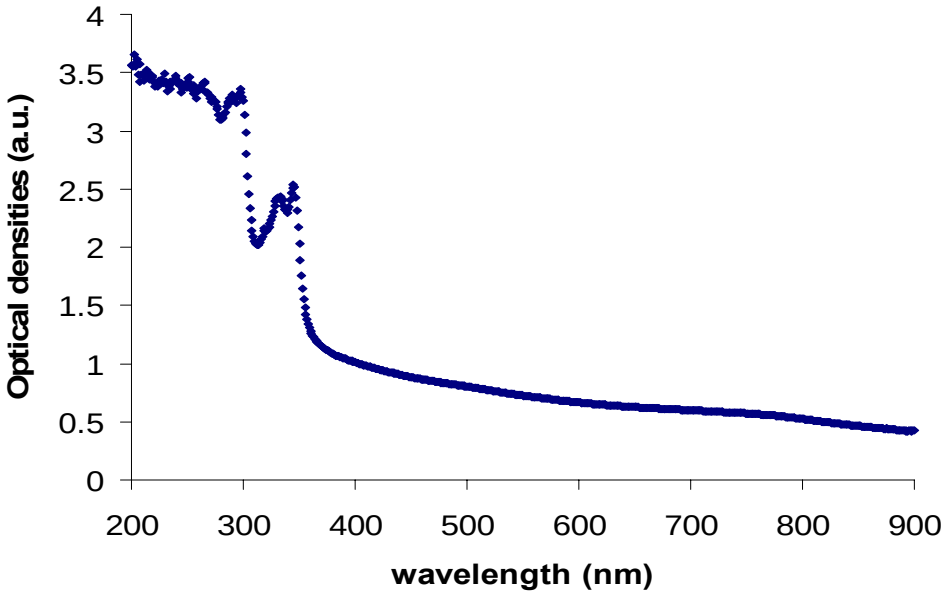

Fig 6.11 Linear absorption spectra of the Opal-SWCNT composite sample

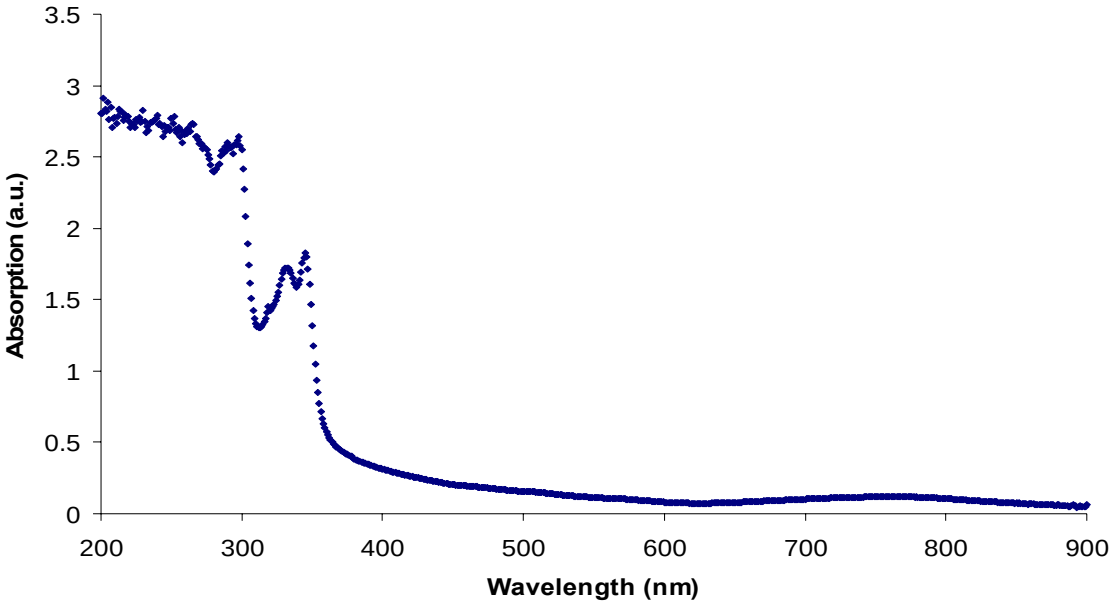

Fig 6.12 Linear absorption spectra due to the response from the SWCNT alone (OpalCNT - Opal)

The close aperture Zscan data obtained for the Opal-SWCNT sample is illustrated in figure 6.13. It presents a distinct peak-valley configuration typical of a negative (self-defocusing) nonlinearity. Using the sample thickness of 1μm, and a linear refractive index of 1.7[28], we obtained $|\chi^{(3)}_{Opal/SWCNT} / \chi^{(3)}_{Quartz}| = 4.88 * 10^3$ yielding a susceptibility of the hybrid system of $\chi^{(3)}_{Opal/SWCNT} = - 9.76 * 10^{-11}$ (esu). Figure 6.14 illustrates the two-photon absorption behavior of the sample. Using the normalized transmittance without an aperture (*Equation 5.9*),

$$T(z) = \sum_{m=0}^{\infty} \frac{\left(\frac{-\beta I_o L_{eff}}{1 + z^2 / z_o^2} \right)^m}{(m+1)^{3/2}},$$

we obtain $\beta = 2.47 * 10^{-2}$ cm/GW. Evaluation of the index change on the axis yields $\Delta n = -0.1317$, for a $\Delta\Phi = - 0.8050$, where $\Delta\Phi$ represents the phase shift at the focus.

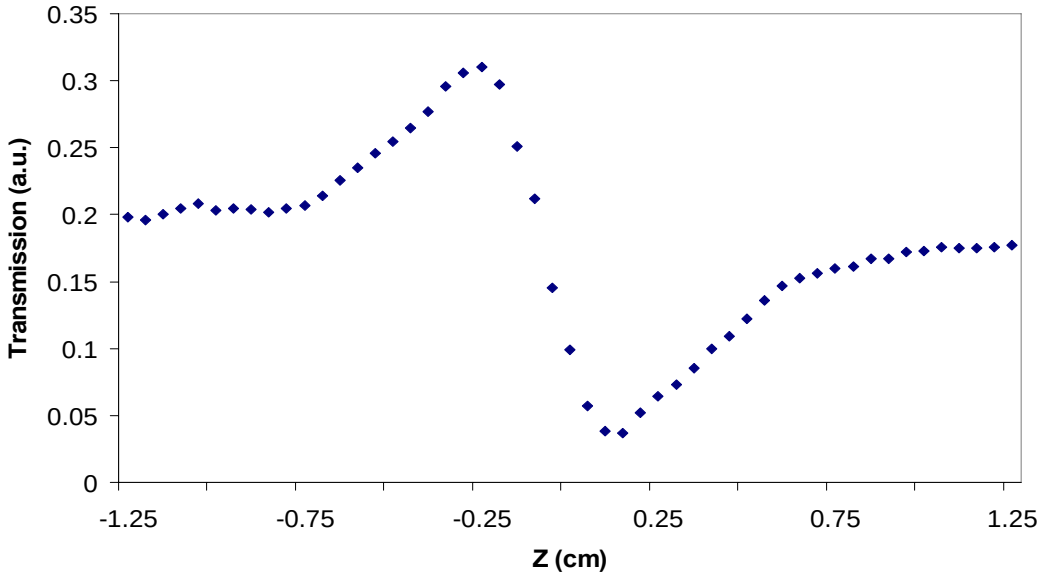

Fig. 6.13 CA Zscan of Opal-SWCNT sample at 800nm and 130fs pulse duration, input power 0.3mW

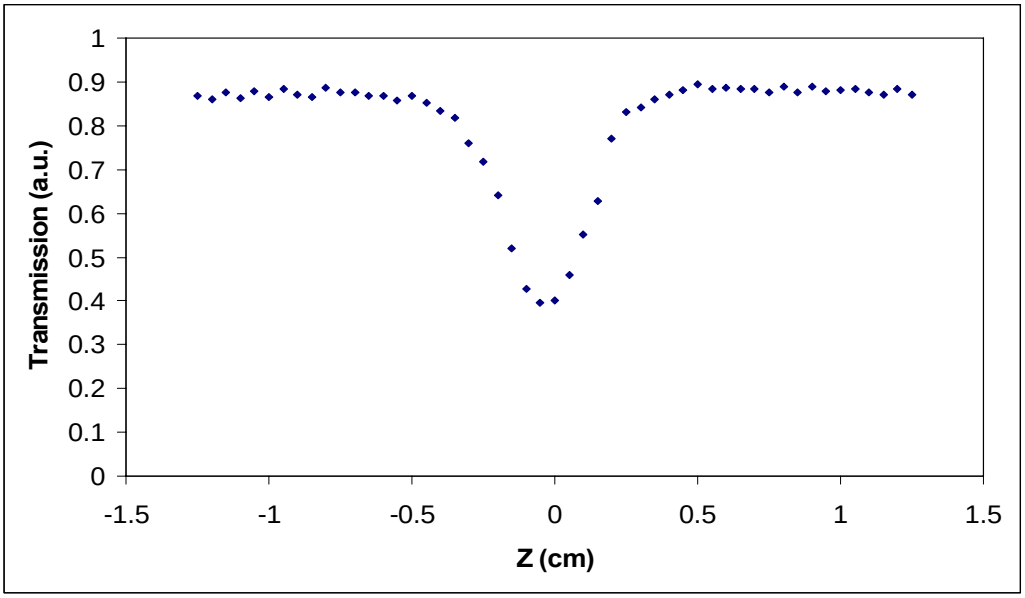

Fig 6.14 OA Zscan of Opal-SWCNT at 800nm 130 fs pulses, 0.4 mW incident power

6.5 Conclusion

In summary, by employing the concept of self-assembly we constructed orderly-structured composites based on SWCNT and conductive polymers. We demonstrated nonlinear optical transmission effects with these structured materials, which stemmed from the interface between its components. The nonlinearity of the hybrid systems was shown to be greatly enhanced by the presence of the single-wall carbon nanotubes. Transmission measurements performed at ns, ps and fs pulse durations showed an overall decrease in the transmission for the SWCNT-based samples owing to an increase in the absorption of the systems. The nonlinear optical susceptibility of the Opal-SWCNT sample was investigated and once again, the results can be attributed mostly to the SWCNT structure. We believe that charge transfer between interfaces of the hybrid structures is responsible for the enhanced nonlinearity. Such nano-tailored materials may find use in novel optoelectronic applications.

References

1. W. H. Brattain, J. Bardeen Phys. Rev. 74, 230 (1948)
2. S. Iijima, Nature 354, **56** (1991)
3. S. Iijima and T. Ichihashi, "*Single-shell carbon nanotubes of 1-nm diameter"*, Nature **363**, 603-605 (1993)
4. R. Saito, *Physical Properties of Carbon nanotubes*, Imperial College Press (1998)
5. M. Brandbyge. "*Atomic and Electronic Structure of Carbon Nanotubes*", (1999)
6. J. W. Mintmire, D. H. Robertson, and C. T. White, *Journal of the Physics and*
1. *Chemistry of Solids* **54**, 1835 (1993).
7. Z. Yao, H.W.Ch. Postma, L. Balents, and C. Dekker, *Nature* **402**, 273 (1999).
8. H.W.Ch. Postma, T.F. Teepen, Z. Yao, M. Grifoni, and C. Dekker, *Science*
2. **293**, 76 (2001).
9. J. N. Coleman, D. F. O'Brien, A. B. Dalton, B. McCarthy, B.Lahr, A. Drury, R. C. Barklie, and W. J. Blau, ''*Measurement of nanotube content in pyrotically generated carbon soot*,'' *Chem. Commun*. **20**, 2001–2002 (2000).
10. R. Murphy, J. N. Coleman, M. Cadek, B. McCarthy, M. Bent, A. Drury, R. C. Barklie, and W. J. Blau, ''*High yield, nondestructive purification and quantification method for multiwalled carbon nanotubes*,'' *J. Phys. Chem. B* **106**, 3087–3091 (2002).
11. Paul's Thesis at NJIT (2006)
12. R. L. Libo®, *Introductory Quantum Mechanics* (Addison-Wesley Publishing Company, Inc., ISBN, 0-201-54715-5, 1993), 2nd edn.
13. C. Harmans, *Mesoscopic Physics an introduction* (TUDelft, 1997)

14. N. Hamada et al, *Phys. Rev. Lett*. **68** (1992) 1579. Ref2: R. Saito et al., *Appl. Phys. Lett*. **60** (1992) 2204.

15. H. Han, S, Vijayalakshmi, A. Lan, Z. Iqbak, H. Grebel, E. Lalanne and A. M. Johnson, *Appl. Phys. Letts*, **82**, 1458-1460 (2003)

16. S. Vijayalakshmi, H. Grebel, G. Yaglioglu, R. Dorsinville and C. W. White, *Appl. Phys. Letts*, **78**, 1754 (2001). S. Vijayalakshmi, H. Grebel, G. Yaglioglu, R. Pino, R. Dorsinville, and C. W. White, *Jour. Appl. Phys*. **88**, No 11 pp 6418-6422 (2000)

17. H. Grebel and W. Zhong, *Opt. Lett.* **18**, 1123 (1993)

18. L. Vivien, D. Riehl, J.F. Delouis, J. A. Delaire, and F. Hache, *Jour. Opti. Soci. of Amer.* **19**, No 2 (2002)

19. H. S. Woo, R. Czerw, S. Webster, D. L. Carroll, J. Ballato, A. E. Strevens, D. O'Brien, W. J. Blau, *Appl. Phys. Lett*. **77** 1393 (2000).

20. H. S. Woo, R. Czerw, S. Webster, D. L. Carroll, J. W. Park, J. H. Lee, *Synth. Met*. **116,** 369 (2001).

21. T. Liu, T. V. Sreekumar, S. Kumar, R. H. Hauge, R. E. Smalley, *Carbon* **41** 2427 (2003).

22. G. B. Blanchet, C.R. Fincher, F. Gao, *Appl. Phys. Lett.* **82** 1290 (2003).

23. E. Kymakis, G. A. J. Amaratunga, *Appl. Phys. Lett.* **80** 112 (2002) .

24. E. Kymakis, I. Alexandrou, G. A. J. Amaratunga, *J. Appl. Phys*. **93** 1764 (2003).

25. Y. Diamant, J. Chen, H. Han, B. Kamenev, L. Tsybeskov and H. Grebel, "Electrochemical polymerization and characterizations, of polycarbazole on Single Wall Carbon Nanotubes", submitted to *Chem. Phys. Lett.*, August 2004.

26. G. G. Malliaras, V. V. Krasnikov, H. J. Bolink, and G. Hadziioannou, *Appl. Phys. Lett*. **67** 455 (1995).

27. S. Vijayalakshmi, H. Grebel, G. Yaglioglu, R. Dorsinville and C. W. White, *Appl. Phys. Lett*, **78**, 1754 (2001).

28. G. V. Prakash, M. Cazzanelli, Z. Gaburro, L. Pavesi, F. Iacona, G. Franzo, amd F. Priolo, Jour. Of. Appl. Phys. 91, 4607 (2002).

Chapter 7

Conclusion and future work

In this dissertation, we have presented detailed studies of a number of highly performing materials, based on their nonlinear optical properties. In the area of bulk material characterization, we have shown that there is a strong correlation between the existence of damage sites in fused silica and the increase in the nonlinear absorption of the material. We have also shown that such damage sites can be annealed in order to curb the overall loss registered in the system. Further investigation of this study could involve using more powerful lasers in order to determine damage threshold and nonlinear absorption at 532 and 1064nm.

We have also performed extensive study of different growth regions in KDP crystals. Based on the nonlinear optical responses registered through open aperture Zscan in these samples, we have proposed a TPA-based imaging technique allowing to generate a two-dimensional mapping of the defects in the crystal lattice. Since this mapping does not allow identification of the different impurities present in the crystal lattice, there is plenty of room for improvement of the technique. Other issues such as scanning time, system resolution and background TPA subtraction to improve the signal to noise ratio are all concerns that need to be addressed in the future.

Our study of Cadmium Sulfide Qdots inside the dendrimer matrices yielded very interesting and promising results. The nonlinearities of these systems were found to depend on the *dot-to-dot* spacing, the excitation frequency and the optical pulse duration. While we have registered very high nonlinear susceptibilities, there is no evidence of enhancement

that can be attributed to dendrimer-QD interactions. We therefore suggest the design of better performing Qdot materials with response strong enough for device implementation. With the established knowledge that the nonlinear response of hybrid semiconductor-dendrimer nanocomposites is a function of the interacting materials, the dot size, the dot-to-dot spacing [2] and the pulse duration, further investigations need to be performed with nanocontainers that will allow a smaller dot to dot spacing and a better coupling or excitonic interaction.

Finally our investigation of nanostructured materials led us to study the nonlinear optical transmission behavior of hybrid systems based on Single wall carbon nanotubes. The nonlinearity of the hybrid systems was shown to be greatly enhanced by the presence of the single-wall carbon nanotubes. Transmission measurements performed at ns, ps and fs pulse durations showed an overall decrease in the transmission for the SWCNT-based samples owing to an increase in the absorption of the systems. However, both the scattering properties and the overall transmission of these hybrid systems need to be addressed in order to be used as optical limiters.

Summary of References

Chapter 1

1. Stavros G. Demos, Mike Staggs, Kaoru Minoshima and James Fujimoto, *Characterization of laser induced damage sites in optical components*, Optics Express 1444, Vol 10, No 25
2. L. Martin-Samos, Y. Limoge, N. Richard, J. P. Crocombette, G. Roma, E. Anglada and E. Artacho, *Europhys. Lett.*, **66**, pp. 680–686 (2004)
3. T. Mohanty, N. C. Mishra, S. V. Bhat, P. K. Basu and D. Kanjilal, *J. Phys. D: Appl. Phys.* **36,** 3151–3155 (2003)
4. N. F. Borrelli, Charlene Smith, Douglas C. Allan, and T. P. Seward III, *J. Opt. Soc. Am. B* Vol. **14**, No. 7, 1606 (1997)
5. M. A. Stevens-Kalceff, A. Stesmans, Joe Wong, *App. Phys. Lett.* **80**, No 54, (2002)
6. R.A. Ganeev, I.A. Kulagin, A.I. Ryasnyansky, R.I. Tugushev, T. Usmanov, Optics Communications **229**, 403–412 (2004)
7. N. L. Boling, M. D. Crisp, and G. Dube, Applied Optics 12, No 4 (1973)
8. Richard L. Sutherland, *Handbook of Nonlinear Optics*, 2nd Edition (2003)
9. Guang S. He, Song H. Liu, *The physics of Nonlinear Optics*, World Scientific (1999)
10. Nguyen Que Huong and Joseph L. Birman, *Phys. Rev. B* **61**, No 19 (1999)
11. M. Sheik-Bahae, A.A. Said, and E.W. Van Stryland, *High-sensitivity, single-beam n_2 measurements*, Opt. Lett., **14**, 955-957 (1989)
12. Paras N. Prasad and David J. Williams, *Nonlinear Optical Properties of Organic molecules and polymers* (1991)

13. Govin P. Agrawal, Robert W. Boyd, *Contemporary Nonlinear Optics*, Academic Press, (1992)

14. Bahaa E. A. Saleh and Malvin Carl Teich, *Fundamentals of Photonics*, John Wiley & Sons (1991)

15. Govind P. Agrawal, *Fiber-Optic Communications Systems*, John Wiley & Sons (2002)

16. Carlo G. Someda, *Electromagnetic Waves*, Chapman & Hall (1998)

17. Robert W. Boyd, *Nonlinear Optics*, Academic Press (2003)

18. Govind Agrawal, *Applications of Nonlinear Fiber Optics*, Academic Press(2001)

19. G. L. Wood, A. A. Said, D. J. Hagan, M. J. Soileau, and E. W. Van Stryland, *Proc. Soc. Photo-Opt. Eng.* 1105:154 (1989)

20. L. W. Tutt and T. F. Boggess, *Prog. Quant. Electr.* **17**. 299 (1993)

21. J. A. Hermann and J. Staromlynska, *Int. J. Nonlin. Opt. Phys.* **2**. 271 (1993)

22. R. L. Sutherland, Handbook of Nonlinear Optics, Series Optical Engineering **52**. (1996).

23. R. Grane, K. Lewis, E. V. Stryland, and M. Khoshnevisan, Mater. Res. Soc. Proc. 374 (1995)

24. Types of Optical limiting materials (Physics of nonlinear optics Ref 9)

25. Guang S. He, Lixiang Yuan, Jayant D. Bhawalkar, and Paras N. Prasad, Applied Optics **36**, No. 15 pp3387-3392, (1997)

26. A. A. Said, T. Xia, A. Dogariu, D. J. Hagan, M. J. Soileau, E. W. Van Stryland and M. Mohebi, *Applied Optics* **34**, No. 18 (1995)

27. M.D. Feit, A.M. Rubenchik, *Mechanisms of CO_2 Laser Mitigation of Laser Damage Growth in Fused Silica*, Lawrence Livermore National Laboratory (2002)

28. Mitsuru Watanabe, Saulius Juodkazis, Hong-Bo Sun, Shigeki Matsuo, Hiroaki Misawa, Masafumi Miwa and Reizo Kaneko, *Appl. Phys. Lett.* **74**, No 26 (1999)

29. N. Bloembergen, *MRS Symp*, vol 51, (1985)

30. S. C. Jones, P. Braulich, R. T. Casper, X. Shen, and P. Kelly, Opt. Engr., vol 28, P-1039, (1989)

Chapter 2

1. Claude Rulliere, Femtosecond Laser Pulses : Principles and Experiments, Springer (2005)
2. Rick Trebino, Kenneth W. DeLong, David N. Fittinghoff, John N. Sweetser, Marco A. Krumbugel, Bruce A. Richman, and Daniel J. Kane, "Measuring ultrashort laser pulse in the time-frequency domain using frequency-resolved optical gating," Rev. Sci. Instrum., vol. 68, 3277-3295 (1997)
3. M. Sheik-Bahae, A.A. Said, and E.W. Van Stryland, *High-sensitivity, single-beam n_2 measurements*, Opt. Lett., **14**, 955-957 (1989)
4. J. Michael Hollas, **Modern Spectroscopy**, John Wiley and Sons (2004)
5. Donald L. Wise, Gary E. Wnek, Debra J. Trantolo, *Electrical and Optical Polymer Systems*, (1998)
6. D. Weaire, B. S. Wherrett, D. A. B. Miller, and S. D. Smith, Opt Lett. **4**, 331 (1979)
7. Mansoor Sheik-Bahae, Ali A Said, Tai-Huei Wei, David J. Hagan and E. W. Van Stryland, Sensitive *Measurements of Optical Nonlinearities Using a Single Beam*, IEEE J. of Quantum Electronics **26**, No. 4, 760-769 (1990)

8. D.A. Partenopoulos and P.M.Rentzepis, *3-Dimensional Optical Storage Memory*, Science **245**, 843-845 (1989).
9. J.H. Strickler and W.W.Webb, *Three-dimensional optical data storage in refractive media by two-photon point excitation*, Opt. Lett. **16**, 1780-1782 (1991).
10. W. Denk, J.H.Strickler, and W.W. Webb, *Two-photon laser scanning fluorescence microscopy*, Science **248**, 73-76 (1990).
11. G.S.He, et al. Appl. Phys. Lett. **67**, 2433-2435 (1995).
12. C.W. Spangler, *Recent developments in the design of organic materials for optical power limiting*, J. Mater. Chem. **9**, 2013 (1999)

Chapter 3

1. Jianrong Qiu, K. Miura, K. Hirao, "Three dimensional optical memory using glasses as a recording medium through a multi-photon absorption process," Jpn. J. Appl. Phys., 37, 2263 (1998)
2. M. Runkel, A. K. Burnham, D. Milam, W. Sell, M. Feit, and A. Rubenchik, "The results of pulse-scaling experiments on rapid-growth DKDP triplers using the Optical Sciences Laser at 351 nm" Proc. SPIE 4347, 359 (2001).
3. N. Bloembergen, "Laser induced electric breakdown in solids" IEEE J. Quantum Electron., 10, 375 (1974).
4. X. A. Shen, S. C. Jones, and P. Braunlich, "Intrinsic optical damage in KBr at 532 nm", Phys. Rev. Lett. 62, 2711 (1989).
5. A. K. Burnham, M. Runkel, M. D. Feit, A.M. Rubenchik, R. L. Floyd, T. A. Land, W. J. Siekhaus, and R. A. Hawley-Fedder, "Laser-Induced Damage in Deuterated

Potassium Dihydrogen Phosphate" Applied Optics, 42, 5483, 2003.

6. Stavros G. Demos, Mike Staggs, Mark Kozlowski, "Investigation of processes leading to damage growth in optical materials for large-aperture lasers," Applied Optics 41, 3628 (2002)
7. C.W. Carr, H. B. Radousky, A. M. Rubenchik, M.D. Feit, S. G. Demos, "Localized dynamics during laser-induced damage in optical materials", Phys. Rev. Lett., In Press. (2004)
8. S. Juodkazis, M. Wantanabe, H. Sun, S. Matsuo, J. Nishii, H. Misawa, M. Miwa, " Optically induced defects in vitreous silica," Optics Letters 21, 1729 (1996)
9. S. O. Kucheyev, S. G. Demos, "Optical defect s produced in fused silica during laser-induced breakdown", Applied Physics Letters, **82**, 3230, 2003
10. C.W. Carr, H.B. Radousky, S.G. Demos, "Wavelength Dependence of Laser Induced Damage: Determining the Damage Initiation Mechanisms", Physical Review Letters, 91, 127402, 2003
11. Alexander J. Glass and Arthur H. Guenther, *Laser induced damage of optical elements: a status report*, *Appl. Optics*, **12**, No 4, 637 (1973)
12. Compilation of status reports available from the Lawrence Livermore National Laboratory (LLNL) library
13. L.W. Hrubesh, R.M. Brusasco, W. Grundler, M.A. Norton, E.E. Donohue, W.A. Molander, S.L. Thompson, S.R. Strodtbeck, P.K. Whitman, M.D. Shirk, P.J. Wegner, M.C. Nostrand, A.K. Burnham. "Methods for mitigating growth of laser-initiated surface damage on DKDP optics at 351 nm", Proc. SPIE vol.**4932**, 180, 2003.

14. B. C. Stuart, M. D. Feit, S. Herman, A. M. Rubenchik, B. W. Shore, and M. D. Perry, "Nanosecond-to-femtosecond laser-induced breakdown in dielectrics", ***Phys. Rev.*** **B** 53, 1749 (1996).

15. N. L. Boling, M. D. Crisp, and G. Dubé, *Laser induce surface damage*, *Appl. Optics*, **12**, No 4, pp650, (1973)

16. R. DeSalvo, Ali A. Said, David J. Hagan, Eric W. Van Stryland, Mansoor Sheik-Bahae, "Infrared to ultraviolet measurements of two photon-absorption and n_2 in wide band solid," IEEE J. of Quantum Electronics **32**, 1324 (1996)

17. Stavros G. Demos, Mike Staggs, " Application of fluorescence microscopy for noninvasive detection of surface contamination and precursors to laser-induced damage." Applied Optics **41**, 1977 (2002)

18. J. Wong, D. Haupt, J. H. Kinney, M. Stevens-Kalceff, A. Stesmans, J. Ferreira, E. Lindsey, I. Hutcheon, " Morphology microstructure and defects in fused silica induced by high 3w (355nm) laser pulses," LLNL report UCRL-ID-142167, January 2001; A summary can be found at Proceedings of SPIE 4347, 466 (2001)

19. L. Skuja, J. Non-Cryst. Solids **179**, 51 (1994) Skuja L, Guttler B, Schiel D and Silin A R 1998 *Phys. Rev.* B **58** 14296

20. Jeff Latkowski, Joel Speth, and Steve Payne, *Laser Inertial Fusion meeting*, LLNL contract No. W-7405-Eng-48, (2001)

21. M. Wantanabe, S. Juodkazis, H. Sun, S. Matsuo, H. Misawa, M. Miwa, R. Kaneko, "Transmission and photoluminescence images of three-dimensional memory in vitreous silica," Appl. Phys. Lett. **74**, 3957 (1999)

22. Temple, P.A.; Lowdermilk, W.H.; Milam, D.; "Carbon dioxide laser polishing of fused silica surfaces for increased laser-damage resistance at 1064 nm", *Appl. Opt.* 21, 3249-55 (1982).

Chapter 4

1. L. N. Rashkovich, *KDP-family Single Crystals* (A. Hilger, Bristol, 1991)

2. W. L. Smith, Appl. Opt. **16**, 1798 (1977).

3. D. Eimerl, Ferroelectrics **72**, 95 (1987).

4. Ming Yan, Rich Torres, Mike Runkel, Bruce Woods, Ian Hutcheon, Natalia Zaitseva and Jim DeYoreo, SPIE **2966**, 11 (1997).

5. S. G. Demos, M. Staggs, M. Yan, H. B. Radousky, and J. J. De Yoreo, Optics Lett. **24**, 268 (1999).

6. J. M. Vail, J. Phys. Chem. Solids **51**, 589 (1990).

7. N.Y. Garces, K.T. Stevens, L.E. Halliburton, M. Yan, N.P. Zaitseva, J.J. DeYoreo, Journal of Crystal Growth **225** 435–439 (2001)

8. M.A. Paesler, P.J. Moyer, Near-field Optics, Wiley/Marcel Dekker, New York, (1994)

9. P.A. Temple, Appl. Opt. **20**, 2656 (1981).

10. L.M. Sheehan, M.R. Kozlowski, D.W. Camp, in: G.J.

11. S. G. Demos, M. Yan, M. Staggs, H. B. Radousky and J. J. De Yoreo, Microscopic Spectral Imaging of Defect Centers in KDP, Lawrence Livermore National Laboratory

12. R. Dorsinville, A. Walser, and R. Pino, Two-Photon Absorption Imaging of KDP crystals. LLNL Report # (1999)

13. G. A. SmolenskiĬ, V. A. Bokov, and V. A. Isupova, *Ferroelectrics and Antiferroelectrics* (Nauka, Leningrad, 1971).

14. E. Dieguez, A. Cintas, P. Hernandez, J.M. Cabrera, J. Crystal Growth **73**, 193 (1985).
15. I.M. Pritula, Yu.N. Velikhov, Some aspects of UV-absorption of NLO KDP crystals, in: R.B. Lal, D.O. Frazier (Ed.), Operational Characteristics and Crystal Growth of Nonlinear Optical Materials, Proceedings of SPIE, Vol. **3793**, 1999 pp. 202–208.
16. Microscopic Spectral Imaging of Defect Centers in KDP, S. G. Demos, M. Yan, M. Staggs, H. B. Radousky and J. J. De Yoreo, Lawrence Livermore National Laboratory
17. W. E. Hughes and W. G. Moulton, J. Chem. Phys. **39**, 1359 (1963).
18. K. Tsuchida, R. Abe, and M. Naito, J. Phys. Soc. Jpn. **35**, 806 (1973).
19. K. Tsuchida and R. Abe, J. Phys. Soc. Jpn. **38**, 1687 (1975).
20. J. A. McMillan and J. M. Clemens, J. Chem. Phys. **68**, 3627 (1978).
21. J. W. Wells, E. Budzinski, and H. C. Box, J. Chem. Phys. **85**, 6340, (1986).
22. S. D. Setzler, K. T. Stevens, L. E. Halliburton, M. Yan, N. P. Zaitseva, and J. J. DeYoreo, Phys. Rev. B **57**, 2643 (1998).
23. K. T. Stevens, N. Y. Garces, L. E. Halliburton, M. Yan, N. P. Zaitseva, J. J. DeYoreo, G. C. Catella, and J. R. Luken, Appl. Phys. Lett. **75**, 1503 (1999).
24. J. E. Davis, R. S. Hughes, and H. W. H. Lee, Chem. Phys. Lett. **207**, 540 (1993).
25. C. D. Marshall, S. A. Payne, M. A. Henesian, J. A. Speth, and H. T. Powell, J. Opt. Soc. Am. B **11**, 774 (1994). // S. G. Demos, M. Yan, M. Staggs, J. J. De Yoreo, and H. B. Radousky, Appl. Phys. Lett. **72**, 2367 (1998).
26. R.J. Davey, J.W. Mullin, J. Crystal Growth **23**, 89 (1974).
27. R.J. Davey, J. Crystal Growth **34**, 109 (1976).
28. K. Sangwal, Prog. Cryst. Growth Character **32** (1996).
29. N. Cabrera, D.A. Vermilea, Growth and Perfection of Crystals, in: R.H. Doremus, B.W. Roberts, D. Turnbull (Eds.), Wiley Inc., New York, 1958, p. 393.
30. M. Ohara, R.C. Reid,ModelingCrystal Growth Rates from Solution, Prentice Hall Inc., Englewood Cliffs, NJ, 1973.
31. A.A. Chernov, Modern Crystallography III: Crystal Growth, Springer, Berlin, 1984.
32. N. Kubota, J.W. Mullin, J. Crystal Growth **152,** 203 (1995).

33. W.J.P. van Enckevort, Science and Technology of Crystal Growth, in: J.P. van der Eerden, O.S.L. Bruinsma (Eds.), Kluwer Academic Publishers, Dordrecht, 1995, p. 355.
34. R.J. Davey, Industrial Crystallization 78, in: E.J. de Jong, S.J. Jancˇ ic´ (Eds.), North-Holland Publ., Amsterdam, 1979, p. 169.
35. N. P. Zaitseva, I. L. Smol'skii, and L. N. Rashkovich, Sov. Phys. Crystallogr. **36**, 113 (1991).
36. Ming Yan, Rich Torres, Mike Runkel, Bruce Woods, Ian Hutcheon, Natalia Zaitseva and Jim DeYoreo, SPIE **2966**, 11 (1997).
37. Michael Etienne, Ardie Walser, Roger Dorsinville, "*Nonlinear Optical Absorption in laser induced modified regions of fused silica substrates"*, *Optics Communications* **240**, No. 4-6, P 417- 421 , 2004

Chapter 5

1. V. Klimov; P. Haring Bolivar; H. Kurz, *Phys. Rev*. B **53**, 1463 (**1996**).
2. A. L. Efros and A. Efros, *Sov. Phys. Semicond*. 16 772 (**1982**).
3. L. Brus*, J. Chem. Phys*. 79, 5566 (**1983**).
4. L. Brus, *Appl. Phys*. A 53, 465 (**1991**).
5. A. Alivisatos, *Science* 271, 933 (**1996**).
6. L. Balogh; D.R. Swanson; R. Spindler; D.A. Tomalia, *Proc. ACS PMSE* **1997**, 77, 118.
7. Gao, Y., Huong, N. Q., Birman, J. L.,Potasek, M. J., Large nonlinear optical properties of semiconductor quantum dot arrays embedded in an organic medium. *Journal of Applied Physics*, 96, 4839 (**2004**).
8. R.G. Ispasoiu; L. Balogh; O.P. Varnavski; D.A. Tomalia; T. Goodson III, *J. Amer. Chem. Soc.* **2000**, 122, 44.

9. Nguyen Que Huong and Joseph Birman, "Quantum dot lattice embedded in an organic medium: Hybrid exciton state and optical response," *Physical review B*, 61,13131, (**2000**)
10. Robert E. Schwerzel, Kevin B. Spahr, John P. Kurmer, Van E. Wood, Jerry A. Jenkins, *J. Phys. Chem.,* 102, 5622 (1998)
11. Edwin F. Hilinski, Patricia A. Lucas, Ying Wang, "A picosecond bleaching study of quantum confined cadmium sulfide microcrystallites in a polymer film," *J. Chem. Phys*., 89, 3435 (**1988**)
12. J. He, W. Ji, G. H. Ma, S. H. Tang, H. I. Elim, W. X. Sun, Z. H. Zhang, W. S. Chin, "Excitonic nonlinear absorption in CdS nanocrystals studied using Z-scan technique," *Journal of Applied Physics*, 95, 6381 (**2004**).
13. H. Du, G. Q. Xu, W. S. Chin, L. Huang, W. Ji, " Synthesis, characterization, and nonlinear optical properties of hybridized CdS-polystyrene nanocomposites," *Chem. Mater*., 14, 4473 (2002)
14. Alex Adronov, Jean M. J. Frechet, Guang S. He, Kyoung-Soo Kim, Sung-Jae Chung, Jacek Swiatkiewicz, Paras N. Prasad, " Novel two-photon absorbing dendritic structures," *Chem. Mater*., 12, 2838 (2000)
15. Y. Gaoa, N. Q. Huong, J.L. Birman, M. J. Potasek, "Highly effective thin film optical filter constructed of semiconductor quantum dot 3D arrays in an organic host," *Nanofabrication: Technologies, Devices, and Applications*, W. Y. Lai and S. Pau, eds, Proc. SPIE, vol. 5592, in press.
16. C. L. Tang, *Fundamentals of Quantum mechanics*, (2005)
17. Hari Singh Nalwa, *Nanostructured Materials and Nanotechnology*, Academic Press (2002). Charles Kittel, *Introduction to Solid States Physics*, John Wiley & Sons (2005)

18. Abramowitz and Stegun, *Handbook of Mathematical Functions*, (1965)

19. Buhleier, E. W.; Wehner, W.; Vo¨gtle, F. *Synthesis* **1978**, 155- 158.

20. Denkewalter, R. G.; Kolc, J.; Lukasavage, W. J. U.S. Pat. 4,- 289,872, Sept. 15, 1981.

21. (4) Denkewalter, R. G.; Kolc, J.; Lukasavage, W. J. U.S. Pat. 4,- 410,688, Oct. 18, 1983

22. A.W. Bosman, H. M. Janssen, and E. W. Meijer, "About dendrimers: Structure, Physical Properties, and applications," *Chem. Rev*., 99, 1665 (1999)

23. Hong Ma and Alex K.-Y. Jen, "Functional dendrimers for nonlinear optics," *Adv. Mater.,* 13, 1201 (2001)

24. Bai Jaeil, Ducharme Stephen, Leonov Alexei G., Lu Liu, Takacs James M., *Proc. SPIE* Vol. 3799, 22 (1999)

25. Shiyoshi Yokoyama, Tatsuo Nakahama, Akira Otomo, and Shinro Mashiko, *J. Am. Chem. Soc*., 122, 3174 (2000)

26. T. Goodson III, O. Varnavski and Y . Wang, "Optical properties and applications of dendrimer-metal nanocomposites," *Int. Reviews in Physical Chemistry*, 23, 109 (2004)

27. V. I. Yudson, P. Reineker, and V. M. Agranovich, *Phys. Rev. B* **52**, R5543 ~1995

28. T. Takagahara, Solid State Commun. **78**, 279 ~1991; Surf. Sci. **267**, 310 ~1992; T. Takagahara and E. Hanamura, *Phys. Rev. Lett.* **56**, 2533 ~1986.

29. A. Engelmann, V. I. Yudson, and P. Reineker, *Phys. Rev. B* **57**, 1784 ~1998

30. V. M. Agranovich, D. M. Basko, G. C. La Rocca, and F. Bassani, *J. Phys.: Condens. Matter.* **10**, 9369 (1998)

31. V M Agranovich, G C La Rocca and F Bassani, *Pure Appl. Opt.* **7** (1998) 119–127

32. 11) L. V. Asryan and R. A. Suris, *IEEE J. Quantum Electron*. **34**, 841 ~1998

33. Y. Gao, N. Q. Huong, J.L. Birman, M. J. Potasek, *Proc. SPIE*, **5592**, 272, (2005).

34. Information obtained from Dendritic Nanotechnologies

35. L.E. Brus, *J. of Chem Phys.* **80**, 4423 (1984)

36. Hong Ma and Alex K.-Y. Jen, *Adv. Mater*., **13**, 1201 (2001)

37. M. Sheik-bahae, A.A. Said, E. W. Van Stryland, *Opt. Letters*, **14**, 955 (1989)

38. Ardie Walser, Stavros G. Demos, Michael Etienne, Roger Dorsinville, *Optics Communications*, **240**, 417 (2004)

39. Lina Yang, R. Dorsinville, R. R. Alfano, W. K. Zou, N. L. Yang, *Optics Letters*, **16**, 758 (1991)

40. R. H. Stolen and C. Lin, *Phys. Rev. A* **17**, 1448 (1978)

41. D. Cotter, M.G. Burt, and J. Manning, *Phys. Rev. Let.*, **68**, 8 (1992)

42. Lina Yang, R. Dorsinville, Q. Z. Yang, P.X. Ye, R. R. Alfano, R. Zamboni, C. Taliani. Optics Letters, 17, 323 (1992).

43. Ursula Keller, K. J. Weingarten, Franz X. Kartner, D. Kopf, B. Braun, I. D. Jung, R. Fluck, H. Honninger, N. Matuschek, J. Aus der Au. IEEE J. of Selected Topics in QE, 2, 435 (1996)

Chapter 6

1. W. H. Brattain, J. Bardeen Phys. Rev. 74, 230 (1948)
2. S. Iijima, Nature 354, **56** (1991)
3. S. Iijima and T. Ichihashi, "*Single-shell carbon nanotubes of 1-nm diameter"*, Nature **363**, 603-605 (1993)
4. R. Saito, *Physical Properties of Carbon nanotubes*, Imperial College Press (1998)
5. M. Brandbyge. "*Atomic and Electronic Structure of Carbon Nanotubes*", (1999)
6. J. W. Mintmire, D. H. Robertson, and C. T. White, *Journal of the Physics and*

Chemistry of Solids **54**, 1835 (1993).

7. Z. Yao, H.W.Ch. Postma, L. Balents, and C. Dekker, *Nature* **402**, 273 (1999).

8. H.W.Ch. Postma, T.F. Teepen, Z. Yao, M. Grifoni, and C. Dekker, *Science* **293**, 76 (2001).

9. J. N. Coleman, D. F. O'Brien, A. B. Dalton, B. McCarthy, B.Lahr, A. Drury, R. C. Barklie, and W. J. Blau, ''*Measurement of nanotube content in pyrotically generated carbon soot*,'' *Chem. Commun*. **20**, 2001–2002 (2000).

10. R. Murphy, J. N. Coleman, M. Cadek, B. McCarthy, M. Bent, A. Drury, R. C. Barklie, and W. J. Blau, *J. Phys. Chem. B* **106**, 3087–3091 (2002).

11. Paul's Thesis at NJIT (2006)

12. R. L. Libo®, *Introductory Quantum Mechanics* (Addison-Wesley Publishing Company, Inc., ISBN, 0-201-54715-5, 1993), 2nd edn.

13. C. Harmans, *Mesoscopic Physics an introduction* (TUDelft, 1997)

14. N. Hamada et al, *Phys. Rev. Lett*. **68** (1992) 1579. Ref2: R. Saito et al., *Appl. Phys. Lett*. **60** (1992) 2204.

15. H. Han, S, Vijayalakshmi, A. Lan, Z. Iqbak, H. Grebel, E. Lalanne and A. M. Johnson, *Appl. Phys. Letts*, **82**, 1458-1460 (2003)

16. S. Vijayalakshmi, H. Grebel, G. Yaglioglu, R. Dorsinville and C. W. White, *Appl. Phys. Letts*, **78**, 1754 (2001). S. Vijayalakshmi, H. Grebel, G. Yaglioglu, R. Pino, R. Dorsinville, and C. W. White, *Jour. Appl. Phys*. **88**, No 11 pp 6418-6422 (2000)

17. H. Grebel and W. Zhong, *Opt. Lett.* **18**, 1123 (1993)

18. L. Vivien, D. Riehl, J.F. Delouis, J. A. Delaire, and F. Hache, *Jour. Opti. Soci. of Amer.* **19**, No 2 (2002)

19. H. S. Woo, R. Czerw, S. Webster, D. L. Carroll, J. Ballato, A. E. Strevens, D. O'Brien, W. J. Blau, *Appl. Phys. Lett*. **77** 1393 (2000).

20. H. S. Woo, R. Czerw, S. Webster, D. L. Carroll, J. W. Park, J. H. Lee, *Synth. Met*. **116,** 369 (2001).

21. T. Liu, T. V. Sreekumar, S. Kumar, R. H. Hauge, R. E. Smalley, *Carbon* **41** 2427 (2003).

22. G. B. Blanchet, C.R. Fincher, F. Gao, *Appl. Phys. Lett.* **82** 1290 (2003).

23. E. Kymakis, G. A. J. Amaratunga, *Appl. Phys. Lett.* **80** 112 (2002) .

24. E. Kymakis, I. Alexandrou, G. A. J. Amaratunga, *J. Appl. Phys*. **93** 1764 (2003).

25. Y. Diamant, J. Chen, H. Han, B. Kamenev, L. Tsybeskov and H. Grebel, "Electrochemical polymerization and characterizations, of polycarbazole on Single Wall Carbon Nanotubes", submitted to *Chem. Phys. Lett.*, August 2004.

26. G. G. Malliaras, V. V. Krasnikov, H. J. Bolink, and G. Hadziioannou, *Appl. Phys. Lett*. **67** 455 (1995).

27. S. Vijayalakshmi, H. Grebel, G. Yaglioglu, R. Dorsinville and C. W. White, *Appl. Phys. Lett*, **78**, 1754 (2001).

28. G. V. Prakash, M. Cazzanelli, Z. Gaburro, L. Pavesi, F. Iacona, G. Franzo, amd F. Priolo, Jour. Of. Appl. Phys. 91, 4607 (2002).